Title

Modulating the Secondary Coordination Sphere around Metal Complexes with Hybrid Tripodal Ligands

Author

Jones, Jason Robert

Publication Date

2017

UNIVERSITY OF CALIFORNIA,
IRVINE

Modulating the Secondary Coordination Sphere around Metal Complexes with Hybrid Tripodal Ligands

DISSERTATION

submitted in partial satisfaction of the requirements
for the degree of

DOCTOR OF PHILOSOPHY

in Chemistry

by

Jason R. Jones

Dissertation Committee:
Professor Andrew S. Borovik, Chair
Professor William J. Evans
Professor Alan F. Heyduk

2017

DEDICATION

To

My wife –
For her unwavering love and support

TABLE OF CONTENTS

LIST OF FIGURES

Page

LIST OF SCHEMES

Page

LIST OF TABLES

LIST OF EQUATIONS

Page

ACKNOWLEDGMENTS

Firstly, I would like to thank Andy for the continuous support over the last five years, both personally and professionally. You have been immensely influential in the way I think about scientific problems. I am thankful for the freedom that you have given me to pursue new ideas. This freedom is what kept me motivated and interested in my projects. I am grateful for the amount of time you spend with the lab; you have always made yourself easily assessable to members of the lab, which really makes it a great place to work. Thank you for taking the time to teach me. I am grateful for the opportunity to have worked with such a great scientist and mentor.

I would also like to thank my committee members, Professor Bill Evans and Professor Alan Heyduk, for all the useful discussions we have had over the years. The discussions we had were the inspiration for new projects and have greatly influenced me and pushed my thinking during my time at UCI.

Thank you to Dr. Joseph Ziller for the teaching me X-ray Crystallography. The X-ray lab was a great place to spend each morning, and I am thankful for all the time you spent teaching me how to solve and refine data and operate the X-ray instrumentation. I think back to these mornings very fondly because I had the opportunity to talk with you and researchers from many groups at UCI and learn about their research.

The Borovik Lab has been a great place work, and this is because of the great people that have made up the lab over the years. The first thing that I noticed when I came to UCI was how welcoming everyone in the Borovik Lab was. Everyone in the lab has been extremely helpful, and I have been tremendously fortunate to be part of the Borovik Lab. Samuel Mann and Nathan Lau have been with me since day one, though all the major milestones at UCI. From doing homework during our first year, working on reports, preparing our dissertations, movie nights, and softball games, you guys have been there for all of it, and have made these times a lot of fun. Thank you for your friendship and support over the last five years; it has made a huge impact on me. Kyle, Jen and Ryan have also been there since day one, and I'll never forget spending these five years with you guys. Thank you also to Noam Levi for being such a great friend. Walmart and Costco trips are never the same without you, but I'm confident that our international visits will continue.

When I started in the lab, I was lucky to learn from very talented chemists, including Taketo, Yohei, Nate, Dave, Jon, Sarah, and Ethan. I am really grateful for the time they spent teaching me how to do experiments in the lab, but also for the great times we had. I can't forget the newer members, Victoria, Kelsey, Justin B, Lisa, Suman, Deborah, Maisha, Sunny, Delores, and Justin L. It's been great working with you all. You have all made the lab a truly memorable place, and I will really miss the great times we had. A big shout out to Victoria, in particular. Thank you so much for all the delicious baked goods and bringing Dwayne Johnson into the lab. It really made the lab a better place.

The facilities at UCI have always been nothing short of excellent. John and Beniam, were always extremely helpful with mass spectrometry and were always willing to help me with a new experiment or help me interpret my data. Phil has always kept the NMR lab up and running and was always willing to answer questions. Joe has kept the X-Ray lab in excellent condition and has always been around to help students. The X-Ray lab is heavily used by the chemistry department, but very rarely suffers downtime because of the pride Joe takes in the lab.

Outside of lab, I made some great friends through the UCI Cycling and Triathlon teams. Thank you to Antonio, Chris, and Jacob for all the time we spent riding and racing bikes together, and of course, riding around all the donut shops in Orange County. Softball games with Bad Life Choices were a great way to spend the end of a work day, thank you to Sam and Sarah for putting together the team every season. Go Bad Life Choices!

I am thankful that throughout my life, my parents have constantly been supportive. I am so grateful to have been geographically close to my Mom and Dad during my time at UCI. To my Dad, it was great to be close enough to have lunch with you on Fridays, and Mom, thank you for all the love and support, and for always knowing that chocolate and peanut butter are the best combo. I couldn't have been where I am today without your love and support.

To my wife and best friend, Masha, I am so lucky that you are so loving and supportive and always there for me. I really couldn't have made it this far without your encouragement and love. You always see things in a positive light, which is refreshing after a tough day. And, of course, I couldn't forget my best bud and companion, Jimmie, who is always ready to play fetch three times before falling asleep.

CURRICULUM VITAE

for
Jason R. Jones

Education

University of California Irvine Irvine, CA
Ph.D. in Chemistry (2017)

San Diego State University San Diego, CA
B.S. in Physics (2011)

Publications

Jones, J. R., Ziller, J. W & Borovik, A. S. Modulating the Primary and Secondary Coordination Spheres within a Series of Co^{II}—OH Complexes. *Inorganic Chemistry.* **2017**, *56*, 1112-1120.

Wilson, R. J., Jones, J. R. & Bennett, M. V. Unprecedented gallium-nitrogen anions: synthesis and characterization of $[(Cl_3Ga)_3N]^{3-}$ and $[(Cl_3Ga)_2NSnMe_3]^{2-}$. *Chemical Communications.* **2013**, *49*, 5049–5051.

Presentations

"Modular approach to tuning the equatorial ligand field strength around a series of Co^{II}—OH complexes with hydrogen bonding cavities in trigonal symmetry," American Chemical Society 251st National Meeting, San Diego, California, March 17, 2016.

"Toward high-nuclearity gallium nitride molecules: Solid state synthesis and DFT calculations," American Chemical Society 241st National Meeting, Anaheim, California, March 27, 2011.

"Toward high-nuclearity gallium nitride molecules: Solid state synthesis and DFT calculations," Student Research Symposium, San Diego State University, California, March 4, 2011.

"Towards New Syntheses and Morphologies of Manganese-doped Group-III Nitride Ferromagnetic Semiconductors," Student Research Symposium. San Diego State University. February 27, 2009.

Awards	**UC Irvine X-Ray Crystallography Fellowship** 2015 - 2016
	ACS Summer Fellowship in Nuclear and Radiochemistry 2011
	Edmond A. Duke Scholarship 2011

ABSTRACT OF THE DISSERTATION

Modulating the Secondary Coordination Sphere Around Metal Complexes with Hybrid Tripodal Ligands

By

Jason R. Jones

Doctor of Philosophy in Chemistry

University of California Irvine, 2017

Professor Andrew S. Borovik, Chair

In biological systems, metalloproteins have evolved to carry out difficult chemical transformations with high activity and selectivity through control of the primary and secondary coordination spheres. Inorganic chemists have developed organic ligand scaffolds to prepare small-molecule model complexes with similar coordination environments to active sites of metalloproteins. However, the resulting complexes are often unable to carry out the same reactivity as their metalloprotein counterparts because they lack the precise control of the secondary coordination sphere.

The most common secondary coordination sphere interaction in metalloproteins is hydrogen bonds (H-bonds). Our group has shown that intramolecular H-bonds can be incorporated into rigid ligand scaffolds to facilitate the activation of small molecules. This has been demonstrated through the use of tetradentate, anionic, and C_3 symmetric ligand scaffolds, which when bound to a metal ion have one open coordination site available for binding of small molecules. Intramolecular H-bonds have been incorporated through the introduction of sulfonamido, urea and amido groups, which can serve as H-bond donors or

acceptors. This dissertation focuses on ligand design that systematically changes the H-bonding network in the secondary coordination sphere around M–O and M–OH units.

The first study investigates the effect of having intramolecular H-bond donors and acceptors in the same ligand by developing new ligands based upon the symmetrical sulfonamido tripodal ligand $[MST]^{3-}$ and the symmetrical urea tripodal ligand $[H_3buea]^{3-}$. Two new hybrid ligand systems ($[H\mathbf{1}^{tol}]^{3-}$ and $[H_2\mathbf{2}^{tol}]^{3-}$) having varying numbers of urea and sulfonamido groups were synthesized. These four ligands were used to synthesize a series of $Co^{II/III}$–OH complexes with varying numbers of intramolecular H-bonds. These complexes allowed for the study of the structural and physical properties arising from modification of the H-bonding network about a Co–OH unit.

The remainder of the dissertation focuses on the development of new hybrid urea tripodal ligands ($[H_3\mathbf{3}^{R}]^{3-}$) based upon $[H_3buea]^{3-}$. These ligands were developed to maintain a constant primary coordination sphere, while modifying the properties of only one H-bond donor. This is accomplished through attaching a substituted phenyl ring with electron-withdrawing groups on *only one* of the urea units, which modulates the acidity of this urea NH. These ligands were used to synthesize a series of M–O(H) (M = $Mn^{III/IV/V}$ and Fe^{III}) complexes, which showed that their properties are highly dependent on changes to *only one* H-bond.

CHAPTER 1

Introduction

Purpose of Dissertation Research

Proteins with metal cofactors (denoted metalloproteins) often carry out difficult chemical transformations with high activity and selectivity.[1–3] The environments surrounding the cofactors within the active sites are precisely tuned to facilitate specific types of chemical reactions. From the perspective of the metal cofactors, the environment is dictated by the primary and secondary coordination spheres around the metal ion(s). The primary coordination sphere is governed by the ligands that are covalently bonded to the metal ion(s). Coordination chemists have studied the effect of the primary coordination spheres on the properties of metal ions for over a century.[4,5] Non-covalent interactions, such as hydrogen bonds (H-bonds), steric effects, and electrostatic effects are the dominant interactions that regulate the secondary coordination sphere. The most common type of secondary coordination sphere interaction in metalloproteins is H-bonds, which have bond strengths typically ranging from 1 to 15 kcal mol^{-1}.[6]

H-bond networks serve a variety of functions, including stabilizing reactive ligands, tuning redox potentials, facilitating proton transfer, and positioning substrates for reactivity.[7,8] The importance of H-bonds in metalloproteins is illustrated in hemoglobin, which is a Fe-containing protein that is responsible for transporting O_2 from the respiratory organs to other tissues in the body. When O_2 is bound to the Fe center in hemoglobin, a bifurcated H-bond is formed between histidine-206 and the superoxido ligand (Figure 1.1). This histidine has been shown to play a crucial structural role in regulating the affinity and rate of dioxygen binding to hemoglobin.[7,9–13]

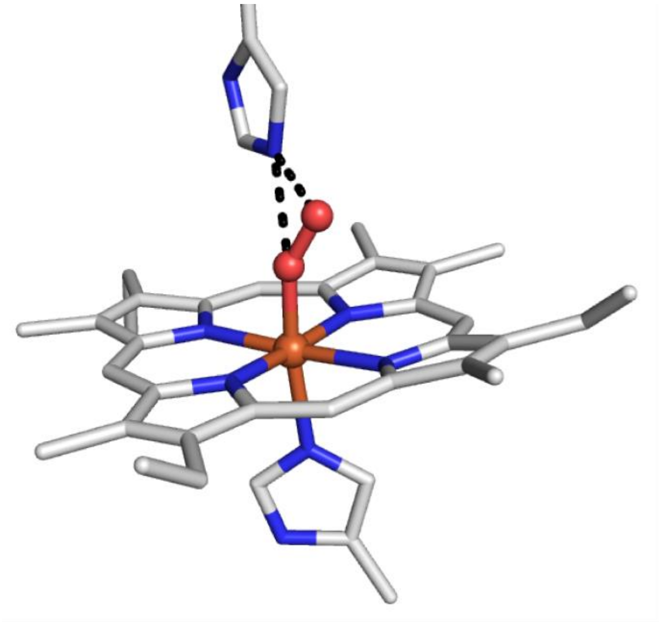

Figure 1.1. Active site of hemoglobin with oxygen bound to the Fe-center (Fe = brown, N = blue, O = red). PDB#: 1GZX[8]

The reversible binding of dioxygen in hemoglobin is attributed to the secondary coordination sphere around the Fe center and the extended protein environment. This is evidenced by the extensive small molecule porphyrin research, which shows that when there are no H-bonding interactions or steric restraints, Fe-porphyrin complexes rapidly and irreversibly bind dioxygen and form μ-oxo bridged dimers.[14–16] There have been many examples of synthetic Fe-porphyrin complexes that bind dioxygen; however, they require low temperatures to prevent the formation of μ–oxo bridged dimers.[17–21] This unproductive μ–oxo bridged dimer formation was overcome by the Collman group using substituted "picket fence" porphyrins (Figure 1.2). In this work, the Collman group prepared an $\mathrm{Fe^{II}}$ complex using a substituted "picket fence" porphyrin that contains four H-bond donors from amide groups. Although these amide NH groups were too far away from the $\mathrm{Fe^{III}}$–superoxido unit to participate in H-bonding, they did provide steric protection to prevent dimerization.

This stabilization allowed the Collman group to work at ambient temperatures and use X-ray diffraction (XRD) to determine the molecular structure of the Fe^{III}–O_2 complex. In this complex, the binding of dioxygen is reversible and dioxygen evolution can be achieved by dissolving the complex in a coordinating solvent, such as pyridine.[22–26] Despite having H-bond donors that are unable to participate in H-bonding with a bound ligand, this Fe^{III}–O_2 complex was one of the first examples of a synthetic system that demonstrated how functional groups with H-bond donors could be incorporated into a rigid ligand.

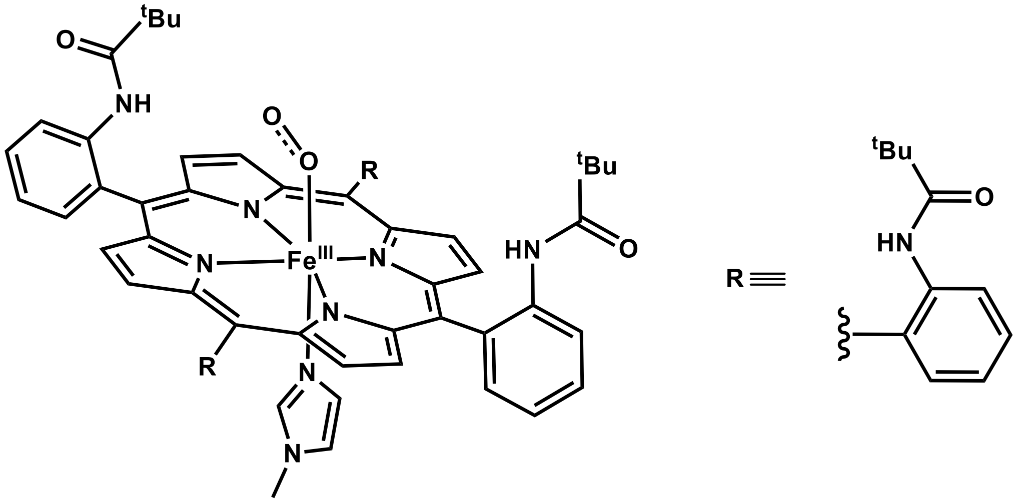

Figure 1.2. Structure of the Fe^{III}—O_2 complex prepared by the Collman group using a substituted "picket fence" porphyrin.[22]

Synthetic chemists have been interested in rationally incorporating H-bonding groups in the secondary coordination sphere around metal ions, in a way that mimics metalloprotein environments. However, this task is difficult because small molecule systems often have flexible structures, unlike the rigid environments within protein active sites.[27] These flexible structures lead to unwanted H-bonds with solvent molecules or counterions. New ligands have been designed containing rigid multidentate frameworks incorporate H-bond donor and acceptor groups within close proximity to the metal ion, which leads to reproducible intramolecular H-bonds. It is with these rigid frameworks that many groups have been able to modulate the secondary coordination sphere around metal ions.[28–40]

The Masuda group developed a series of ligands capable of forming intramolecular H-bonds to probe the effect of H-bonds on the stability of metal complexes. Masada and coworkers designed dinuclear Cu^{II} peroxide complexes with tripyridine tripodal ligands that vary the number of H-bond donating amino groups appended to the pyridine donor atoms (Figure 1.3). Resonance Raman spectra of these complexes showed an increase in the ν(O–O) stretching frequency with increasing number of H-bond donors. The increase in stretching frequency suggests that the H-bond interaction to the peroxide ligand reduces electron density in the π* orbitals, thereby, increasing the O–O bond strength. This research highlighted the stabilizing effect of H-bonds on metal complexes.[41]

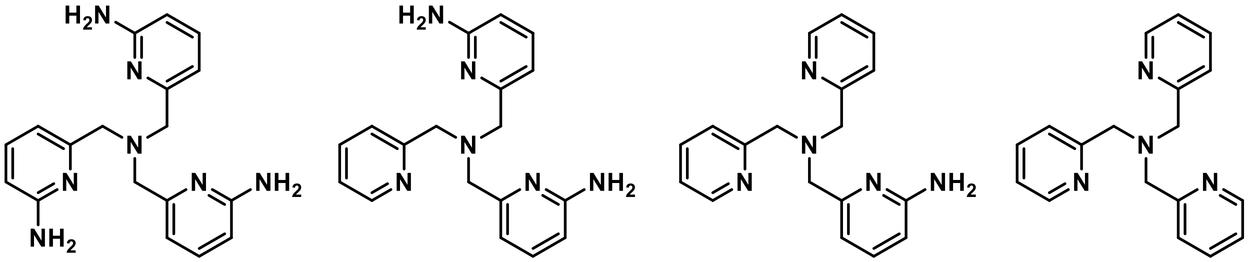

Figure 1.3. A series of ligands used by Masuda to probe the stability of Cu^{II}—(μ—O$_2$)—Cu^{II} complexes.[41]

In a more recent example, the Yang lab has synthesized new Co^{II} complexes with tetradentate Schiff base ligands with appended crown-ether cavities that allows for the incorporation of alkali and alkaline earth Lewis acidic cations (Na$^+$, K$^+$, Ca^{2+}, Sr^{2+}, and Ba^{2+}) (Figure 1.4).[42] Cyclic voltammetry of these complexes showed that in comparison to the Co^{II} complex without a proximal cation, the Co$^{II/I}$ redox couple is shifted 130 mV positive for Na$^+$ and K$^+$, and 230-300 mV positive for Ba^{2+}, Sr^{2+}, and Ca^{2+}. Interestingly, the different Lewis acids resulted in a small change in the electronic absorption spectra for the d–d transition of

Co^{II} ($\Delta\lambda_{max} \sim 15$ nm) for these complexes, suggesting the primary coordination sphere remains similar. The vibrational frequency of the imine C=N bond for the series shifts slightly with the Lewis acid strength of the redox-inactive metal ion ($\Delta\nu_{C=N} \sim 22$ cm^{-1}). This small shift suggests that the redox-inactive metal ions have little effect on the electron density of the Co^{II} center. These two observations suggest that this effect is not a result of changes in the primary coordination sphere. Rather, this effect likely arises from the incorporation of a cationic charge in the secondary coordination sphere of the Co^{II} center, illustrating how redox properties of metal ions are influenced by electrostatic interactions in the secondary coordination sphere. There are other examples of complexes with redox-inactive metal ions appended to the ligand;[40,42–50] however, this ligand designed by the Yang group allows for structural changes introduced by the redox-inactive metal ions to be minimized, while allowing for a large variety of metal ions to be studied.

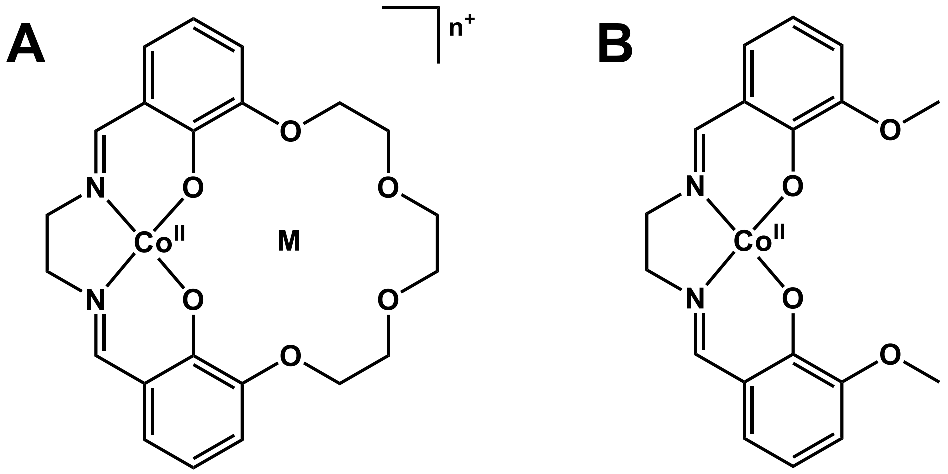

Figure 1.4. (A) New Co^{II} complexes with redox-inactive metal ions synthesized by the Yang group: n = 1 for Na^+ and K^+; n = 2 for Ca^{2+}, Sr^{2+}, and Ba^{2+}; and (B) the Co^{II} complex lacking redox-inactive metal ions used for comparison in this study.[42]

Previous Work by the Borovik Group

The Borovik group is interested in studying the effects of the secondary coordination sphere on the properties of metal ions. We have successfully demonstrated that intramolecular H-bonds can be incorporated into rigid ligands to facilitate the activation of small molecules.[51] This is achieved primarily by using tetradentate, anionic, nitrogen atom-based tripodal ligands, which when bound to a metal ion have one open coordination site available for binding of small molecules. Using tripodal ligands enforces local C_3 symmetry around the metal ion, which enables access to a high-spin electronic configuration for the metal ion that are difficult to access in other local symmetries. The use of tripodal ligands with H-bond donors has allowed for the stabilization of rare M–oxido species in high-spin electronic configurations.[51–57]

The Borovik group reported the synthesis and characterization of Co^{II} complexes with varying numbers of urea and amide ligands to create a hybrid ligand platform that allowed for systematic modulation of the number of H-bond donors in the secondary coordination sphere (Figure 1.5). The number of H-bond donors varied from zero (all amide containing arms) to three (all urea containing arms). The ligand frameworks containing at least one H-bond were found to react with dioxygen to generate Co^{III}–OH complexes. In contrast, the complex with no H-bond donors did not react with dioxygen under any conditions. The ability to detect the Co^{III}–OH species can be attributed to the added stability the H-bonds provides to the exogenous hydroxido unit. The importance of H-bonds in these complexes is further supported by the fact that stability of the series of Co^{III}–OH complexes increased with increasing number H-bond donors. The increased stability of the complexes was attributed to the intramolecular H-bonds causing a decrease in the nucleophilicity of the Co^{III}–OH unit. The observed reactivity of the Co^{II} species and stability of the Co^{III} species show the dynamic ability of H-bonds to introduce reactivity, but also stability under different circumstances.[38]

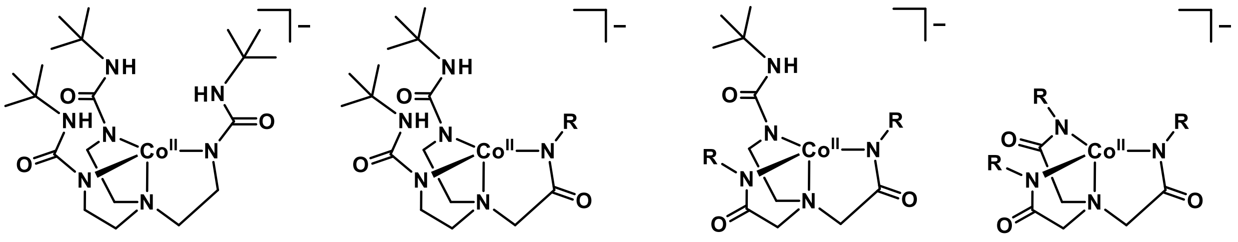

Figure 1.5. Series of four-coordinate trigonal monopyramidal Co^{II} complexes synthesized by the Borovik group to study the effect of H-bonding on O_2 activation.[38]

The Borovik group also has developed systems in which the ligand provides H-bond acceptors within the secondary coordination sphere. To investigate the chemistry of H-bond accepting moieties, the tripodal ligand platform $[MST]^{3-}$ was designed (Figure 1.6A). While $[MST]^{3-}$ has a similar primary coordination sphere to $[H_3buea]^{3-}$ (Figure 1.6B), it now has H-bond accepting sulfonamido groups rather than H-bond donating urea moieties seen in $[H_3buea]^{3-}$. The $[MST]^{3-}$ ligand cavity has been shown to support M–OH_2, M–OH, and M–NH_3 complexes, where H-bonding is present between the oxygen atoms of the sulfonamido groups and the hydrogen atom(s) of the corresponding exogenous ligand.[50,58–61] In addition to participating in H-bond, the sulfonamido groups are well suited to serve as a binding site for a secondary metal ion. Taking advantage of the auxiliary binding site has allowed for preparation of heterobimetallic hydroxido-bridged complexes with a variety of both redox-inactive and redox-active metal ions (Figure 1.7).[40,49,58,62]

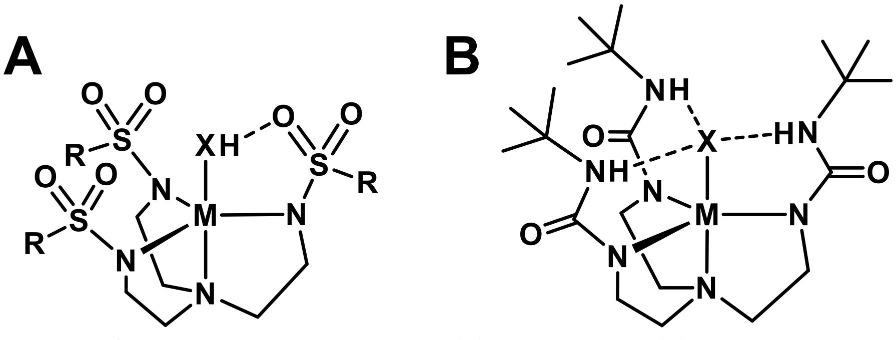

Figure 1.6. Structure of metal complexes with the (A) $[MST]^{3-}$ and (B) $[H_3buea]^{3-}$ ligands. H-bonding is shown with dashed lines. R = 1,3,5-trimethylbenzene.

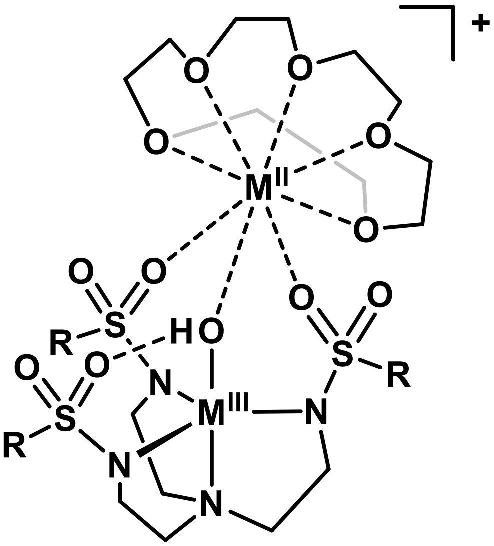

Figure 1.7. Example of hydroxido bridged heterobimetallic complexes with the $[MST]^{3-}$ ligand. M^{III} = Fe, Mn, Ga; M^{II} = Ca, Sr, and Ba.[58]

Overview of Chapters

The research in this dissertation focuses on ligand design that systematically changes the H-bonding network in the secondary coordination sphere around M–OH and M–O units. The ligands $[MST]^{3-}$ and $[H_3buea]^{3-}$ were the design inspiration for the new hybrid ligands presented in this thesis, due to the fact that both ligands provide rigid tripodal framework that allows for the formation of intramolecular H-bonds to a fifth ligand coordinated to the metal ion. Since the Borovik group has studied both $[MST]^{3-}$ and $[H_3buea]^{3-}$ extensively with a multitude of transition metal ions, comparisons between analogous complexes prepared with new hybrid ligand systems with these functional groups would provide additional information on how the secondary coordination sphere influences function.

Research in Chapter 2. Two new hybrid ligands $[H_2\mathbf{2}^{tol}]^{3-}$ and $[H\mathbf{1}^{tol}]^{3-}$ were synthesized, which includes a combination of H-bond donor and acceptor groups from urea or sulfonamido moieties (Figure 1.8). The ligand $[H_2\mathbf{2}^{tol}]^{3-}$ contains two H-bond donors from two urea moieties and one H-bond acceptor from a lone sulfonamido group; the ligand $[H\mathbf{1}^{tol}]^{3-}$ was prepared to support intramolecular H-bond networks containing two H-bond acceptors from two sulfonamido groups and one H-bond donor from a lone urea. The corresponding Co^{II}–OH and Co^{III}–OH complexes with $[H_2\mathbf{2}^{tol}]^{3-}$ and $[H\mathbf{1}^{tol}]^{3-}$ ligands were synthesized and characterized. In conjunction with the two symmetrical systems, these hybrid ligands allowed for study of the structural and physical effects arising from the modification of the H-bonding network about a Co–OH unit. The quantitative electronic effect of urea and sulfonamido ligands are evaluated through a ligand field analysis from the electronic absorption spectra of the four complexes. The H-bond networks in the series of complexes are probed by X-Ray diffraction methods, where the number of intramolecular H-bonds in the complexes varies from one to three. The stability of the corresponding Co^{III}–OH complexes increases with increasing number of H-bond donors in the ligand, similar to the series of Co^{III}–OH complexes discussed above.[38]

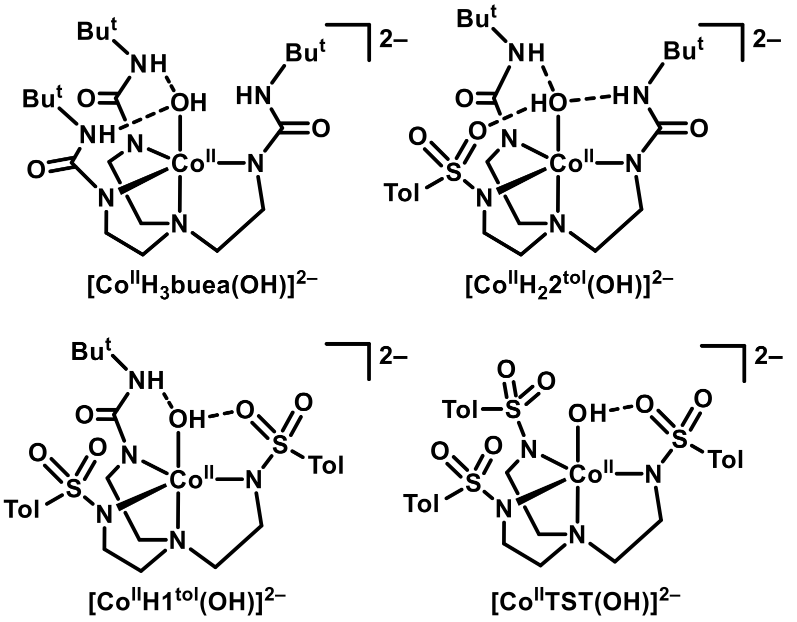

$[Co^{II}H_3buea(OH)]^{2-}$ $[Co^{II}H_2\mathbf{2}^{tol}(OH)]^{2-}$

$[Co^{II}H\mathbf{1}^{tol}(OH)]^{2-}$ $[Co^{II}TST(OH)]^{2-}$

Figure 1.8. Metal complexes synthesized with symmetrical and hybrid ligands in Chapter 2.

Research in Chapter 3. The results presented in Chapter 2 suggest that the structural and reactivity properties of the series of Co^{II}–OH complexes are affected by both the primary and secondary coordination sphere. This makes it difficult to isolate how the secondary coordination sphere affects the structure and functional properties of these complexes. A new series of hybrid urea based tripodal ligands, based upon $[H_3buea]^{3-}$ were developed to maintain a nearly constant primary coordination sphere, while modifying the properties of *only one* of the intramolecular H-bond donors. This is accomplished by attaching a para-substituted phenyl ring on *only* one of the urea groups, which modulates the acidity of this urea NH. These ligands were used to synthesize a series of Mn^{III}–O(H) complexes and their physical properties and reactivity with substrates were evaluated (Figure 1.9). The second order rate constants observed for the reaction of the Mn^{III} compounds with 9,10-dihydroanthracene (DHA) are highly dependent on changes to *only one H-bond donor*. In addition, changing *only one H-bond donor* causes a significant change in the pK_a of the Mn^{III}–O(H) complexes.

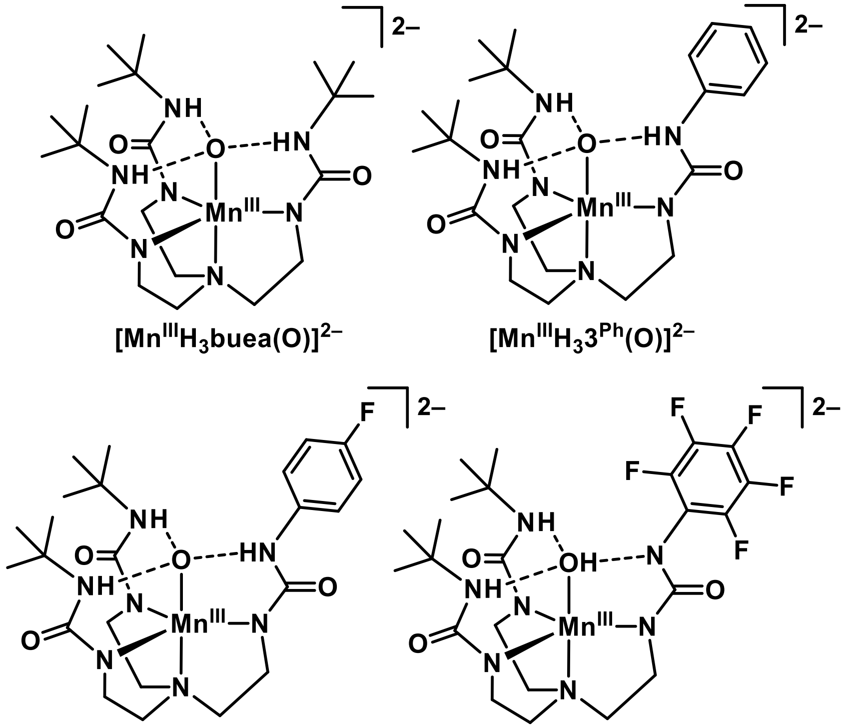

$[Mn^{III}H_3buea(O)]^{2-}$ $[Mn^{III}H_33^{Ph}(O)]^{2-}$

$[Mn^{III}H_33^{F}(O)]^{2-}$ $[Mn^{III}H_23^{5F}(OH)]^{2-}$

Figure 1.9. A series of Mn^{III}–O(H) complexes synthesized and characterized in Chapter 3.

Research in Chapter 4. The oxidation chemistry of the Mn^{III}–O(H) complexes presented in Chapter 3 are studied using electronic absorbance spectroscopy and electron paramagnetic resonance (EPR) spectroscopy. New Mn^{IV} and Mn^{V} species are generated and have different stability than the analogous complexes using the symmetrical urea ligand $[H_3buea]^{3-}$. The Mn^{IV} complexes were reacted with various acids to generate protonated species. Preliminary results suggest that intramolecular proton transfer between H-bonded groups upon oxidation of $[Mn^{III}H_2\mathbf{3}^{5F}(OH)]^{2-}$ could be occurring (Scheme 1.1).

Scheme 1.1. Oxidation of $[Mn^{III}H_2\mathbf{3}^{5F}(OH)]^{2-}$ Showing Possible Intramolecular Proton Transfer

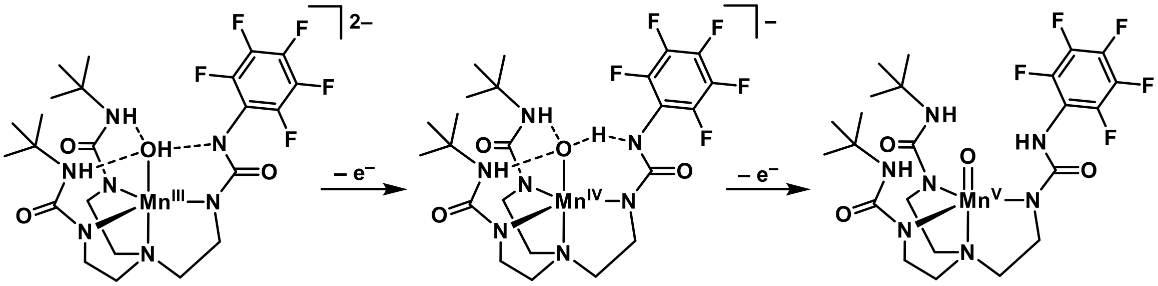

Research in Chapter 5. With the development of the new hybrid urea based tripodal ligands developed in Chapter 3, new Fe^{III}–O(H) complexes were synthesized and EPR properties were evaluated. The EPR spectra provides information on the protonation state of these Fe^{III} complexes. The oxidation chemistry of the Fe^{III} complexes was reported and different species were generated depending on which electron withdrawing substituent was attached to the modified urea arm. However, upon oxidation, further reactivity occurred to produce complexes with identical EPR parameters that are similar to $[Fe^{III}H_3buea(OH)]^{-}$.

References

(1) Holm, R. H.; Kennepohl, P.; Solomon, E. I. Structural and Functional Aspects of Metal Sites in Biology. *Chem. Rev.* **1996**, *96* (7), 2239–2314.
(2) Poulos, T. L. Heme Enzyme Structure and Function. *Chem. Rev.* **2014**, *114* (7), 3919–3962.
(3) Stone, K. L.; Borovik, A. Lessons from Nature: Unraveling Biological CH Bond Activation. *Curr. Opin. Chem. Biol.* **2009**, *13* (1), 114–118.
(4) Werner, A. Über Die Raumisomeren Kobaltverbindunge. *Ann. Chem.* **1912**, *386*, 1–272.

(5) Werner, A. Zur Kenntnis Des Asymmetrischen Kobaltatoms. III. *Berichte der Dtsch. Chem. Gesellschaft* **1911**, *44* (3), 3272–3278.

(6) Etter, M. C. Encoding and Decoding Hydrogen-Bond Patterns of Organic Compounds. *Acc. Chem. Res.* **1990**, *23* (4), 120–126.

(7) Igarashi, J.; Kobayashi, K.; Matsuoka, A. A Hydrogen-Bonding Network Formed by the B10-E7-E11 Residues of a Truncated Hemoglobin from Tetrahymena Pyriformis Is Critical for Stability of Bound Oxygen and Nitric Oxide Detoxification. *J. Biol. Inorg. Chem.* **2011**, *16* (4), 599–609.

(8) Paoli, M.; Liddington, R.; Tame, J.; Wilkinson, A.; Dodson, G. Crystal Structure of T State Haemoglobin with Oxygen Bound At All Four Haems. *J. Mol. Biol.* **1996**, *256* (4), 775–792.

(9) Perutz, M. F. Stereochemistry of Cooperative Effects in Haemoglobin: Haem–Haem Interaction and the Problem of Allostery. *Nature* **1970**, *228* (5273), 726–734.

(10) Huynh, B. H.; Case, D. A.; Karplus, M. Nature of the Iron-Oxygen Bond in Oxyhemoglobin. *J. Am. Chem. Soc.* **1977**, *99* (18), 6103–6105.

(11) Birukou, I.; Schweers, R. L.; Olson, J. S. Distal Histidine Stabilizes Bound O2 and Acts as a Gate for Ligand Entry in Both Subunits of Adult Human Hemoglobin. *J. Biol. Chem.* **2010**, *285* (12), 8840–8854.

(12) Yuan, Y.; Tam, M. F.; Simplaceanu, V.; Ho, C. New Look at Hemoglobin Allostery. *Chem. Rev.* **2015**, *115* (4), 1702–1724.

(13) Lukin, J. A.; Ho, C. The Structure–Function Relationship of Hemoglobin in Solution at Atomic Resolution. *Chem. Rev.* **2004**, *104* (3), 1219–1230.

(14) Cohen, I. A.; Caughey, W. S. Substituted Deuteroporphyrins. IV. Kinetics and Mechanism of Reactions of Iron(II) Porphyrins with Oxygen. *Biochemistry* **1968**, *7* (2), 636–641.

(15) Hoffman, a B.; Collins, D. M.; Day, V. W.; Fleischer, E. B.; Srivastava, T. S.; Hoard, J. L. The Crystal Structure and Molecular Stereochemistry of μ-Oxo-Bis(α,β,γ,δ-Tetraphenylporphinatoiron (III)). *J. Am. Chem. Soc.* **1972**, *94* (10), 3620–3626.

(16) Shikama, K. Stability Properties of Dioxygen-Iron(II) Porphyrins: An Overview from Simple Complexes to Myoglobin. *Coord. Chem. Rev.* **1988**, *83* (C), 73–91.

(17) Basolo, F.; Hoffman, B. M.; Ibers, J. A. Synthetic Oxygen Carriers of Biological Interest. *Acc. Chem. Res.* **1975**, *8* (11), 384–392.

(18) Baldwin, J. E.; Huff, J.; Balwin, J. S.; Huff, J. Binding of Dioxygen to Iron(II). Reversible Behavior in Solution. *J. Am. Chem. Soc.* **1973**, *95* (17), 5757–5759.

(19) Anderson, D. L.; Weschler, C. J.; Basolo, F. Reversible Reaction of Simple Ferrous Porphyrins with Molecular Oxygen at Low Temperatures. *J. Am. Chem. Soc.* **1974**, *96* (17), 5599–5600.

(20) Wagner, G. C.; Kassner, R. J. Spectroscopic Properties of Protoheme Complexes Undergoing Reversible Oxygenation. *J. Am. Chem. Soc.* **1974**, *96* (17), 5593–5595.

(21) Collman, J. P.; Gagne, R. R.; Reed, C. A.; Robinson, W. T.; Rodley, G. A. Structure of an Iron(II) Dioxygen Complex; a Model for Oxygen Carrying Hemeproteins. *Proc. Natl. Acad. Sci.* **1974**, *71* (4), 1326–1329.

(22) Collman J. P.; Gagne, R. R.; Halbert, T. R.; Marchon, J. C.; Reed, C. A.; Collman, J. P.; Gagne, R. R.; Halbert, T. R.; Marchon, J. C.; Reed, C. A. Reversible Oxygen Adduct Formation in Ferrous Complexes Derived from a Picket Fence Porphyrin. Model for Oxymyoglobin. *J. Am. Chem. Soc.* **1973**, *95* (23), 7868–7870.

(23) Collman J. P.; Reed, C. A.; Collman, J. P.; Reed, C. A.; Coliman, J. P.; Reed, C. A. Syntheses of Ferrous-Porphyrin Complexes. Hypothetical Model for Deoxymyoglobin. *J. Am. Chem. Soc.* **1973**, *95* (6), 2048–2049.

(24) Collman, J. P.; Gagne, R. T.; Reed, C. A.; Collman James, P.; Gagne, R. T.; Reed, C. A. Paramagnetic Dioxygen Complex of Iron(II) Derived from a Picket Fence Porphyrin. Further Models for Hemoproteins. *J. Am. Chem. Soc.* **1974**, *96* (8), 2629–2631.

(25) Collman, J. P.; Gagne, R. R.; Reed, C.; Halbert, T. R.; Lang, G.; Robinson, W. T.; Collman James, P.; Gagne, R. R.; Reed, C.; Halbert, T. R.; et al. Picket Fence Porphyrins. Synthetic Models for Oxygen

Binding Hemoproteins. *J. Am. Chem. Soc.* **1975**, *97* (6), 1427–1439.

(26) Collman James, P.; Boulatov, R.; Sunderland, C. J.; Fu, L. Functional Analogues of Cytochrome c Oxidase, Myoglobin, and Hemoglobin. *Chem. Rev.* **2004**, *104* (2), 561–588.

(27) Borovik, A. S. Bioinspired Hydrogen Bond Motifs in Ligand Design: The Role of Noncovalent Interactions in Metal Ion Mediated Activation of Dioxygen. *Acc. Chem. Res.* **2005**, *38* (1), 54–61.

(28) Natale, D.; Mareque-Rivas, J. C. The Combination of Transition Metal Ions and Hydrogen-Bonding Interactions. *Chem. Commun.* **2008**, No. 4, 425–437.

(29) Blacquiere, J. M.; Pegis, M. L.; Raugei, S.; Kaminsky, W.; Forget, A.; Cook, S. A.; Taguchi, T.; Mayer, J. M. Synthesis and Reactivity of Tripodal Complexes Containing Pendant Bases. *Inorg. Chem.* **2014**, *53* (17), 9242–9253.

(30) Metteau, L.; Parsons, S.; Mareque-Rivas, J. C. Hydrogen Bonding Cavities Regulating Redox Behavior and Binding of Metal-Bound Ligands. *Inorg. Chem.* **2006**, *45* (17), 6601–6603.

(31) Mukherjee, J.; Lucas, R. L.; Zart, M. K.; Powell, D. R.; Day, V. W.; Borovik, A. S. Synthesis, Structure, and Physical Properties for a Series of Monomeric Iron(III) Hydroxo Complexes with Varying Hydrogen-Bond Networks. *Inorg. Chem.* **2008**, *47* (13), 5780–5786.

(32) Moore, C. M.; Quist, D. A.; Kampf, J. W.; Szymczak, N. K. A 3-Fold-Symmetric Ligand Based on 2-Hydroxypyridine: Regulation of Ligand Binding by Hydrogen Bonding. *Inorg. Chem.* **2014**, *53* (7), 3278–3280.

(33) Sickerman, N. S.; Park, Y. J.; Ng, G. K.-Y.; Bates, J. E.; Hilkert, M.; Ziller, J. W.; Furche, F.; Borovik, A. S. Synthesis, Structure, and Physical Properties for a Series of Trigonal Bipyramidal M(II)–Cl Complexes with Intramolecular Hydrogen Bonds. *Dalt. Trans.* **2012**, *41* (15), 4358.

(34) Yeh, C.-Y. Y.; Chang, C. J.; Nocera, D. G. "Hangman" Porphyrins for the Assembly of a Model Heme Water Channel. *J. Am. Chem. Soc.* **2001**, *123* (7), 1513–1514.

(35) Berreau, L. M.; Makowska-Grzyska, M. M.; Arif, A. M.; Arif Atta, M. Modeling the Active Site Chemistry of Liver Alcohol Dehydrogenase: Mononuclear Zinc Methanol and N,N-Dimethylformamide Complexes of a Nitrogen/Sulfur Ligand Possessing an Internal Hydrogen Bond Donor. *Inorg. Chem.* **2001**, *40* (10), 2212–2213.

(36) Hammes, B. S.; Young, Jr., V. G.; Borovik, A. S. Hydrogen-Bonding Cavities about Metal Ions: A Redox Pair of Coordinatively Unsaturated Paramagnetic Co-OH Complexes. *Angew. Chemie Int. Ed.* **1999**, *38* (5), 666–669.

(37) Shook, R. L.; Gunderson, W. A.; Greaves, J.; Ziller, J. W.; Hendrich, M. P.; Borovik, A. S. A Monomeric Mn(III)–Peroxo Complex Derived Directly from Dioxygen. *J. Am. Chem. Soc.* **2008**, *130* (28), 8888–8889.

(38) Lucas, R. L.; Zart, M. K.; Murkerjee, J.; Sorrell, T. N.; Powell, D. R.; Borovik, A. S. A Modular Approach toward Regulating the Secondary Coordination Sphere of Metal Ions: Differential Dioxygen Activation Assisted by Intramolecular Hydrogen Bonds. *J. Am. Chem. Soc.* **2006**, *128* (48), 15476–15489.

(39) Park, Y. J.; Sickerman, N. S.; Ziller, J. W.; Borovik, A. S. Utilizing Tautomerization of 2-Amino-Oxazoline in Hydrogen Bonding Tripodal Ligands. *Chem. Commun.* **2010**, *46* (15), 2584–2586.

(40) Park, Y. J.; Ziller, J. W.; Borovik, A. S. The Effects of Redox-Inactive Metal Ions on the Activation of Dioxygen: Isolation and Characterization of a Heterobimetallic Complex Containing a Mn(III)–(μ-OH)–Ca(II) Core. *J. Am. Chem. Soc.* **2011**, *133* (24), 9258–9261.

(41) Wada, A.; Honda, Y.; Yamaguchi, S.; Nagatomo, S.; Kitagawa, T.; Jitsukawa, K.; Masuda, H. Steric and Hydrogen-Bonding Effects on the Stability of Copper Complexes with Small Molecules. *Inorg. Chem.* **2004**, *43* (18), 5725–5735.

(42) Reath, A. H.; Ziller, J. W.; Tsay, C.; Ryan, A. J.; Yang, J. Y. Redox Potential and Electronic Structure Effects of Proximal Nonredox Active Cations in Cobalt Schiff Base Complexes. *Inorg. Chem.* **2017**, *56* (6), 3713–3718.

(43) Lee, Y. M.; Bang, S.; Yoon, H.; Bae, S. H.; Hong, S.; Cho, K. Bin; Sarangi, R.; Fukuzumi, S.; Nam, W.

Tuning the Redox Properties of a Nonheme Iron(III)-Peroxo Complex Binding Redox-Inactive Zinc Ions by Water Molecules. *Chem. Eur. J.* **2015**, *21* (30), 10676–10680.

(44) Bang, S.; Lee, Y.-M.; Hong, S.; Cho, K.-B.; Nishida, Y.; Seo, M. S.; Sarangi, R.; Fukuzumi, S.; Nam, W. Redox-Inactive Metal Ions Modulate the Reactivity and Oxygen Release of Mononuclear Non-Haem Iron(III)–peroxo Complexes. *Nat. Chem.* **2014**, *6* (10), 934–940.

(45) Bae, S. H.; Lee, Y. M.; Fukuzumi, S.; Nam, W. Fine Control of the Redox Reactivity of a Nonheme Iron(III)–Peroxo Complex by Binding Redox-Inactive Metal Ions. *Angew. Chemie - Int. Ed.* **2017**, *56* (3), 801–805.

(46) Tsui, E. Y.; Tran, R.; Yano, J.; Agapie, T. Redox-Inactive Metals Modulate the Reduction Potential in Heterometallic Manganese–oxido Clusters. *Nat. Chem.* **2013**, *5* (4), 293–299.

(47) Herbert, D. E.; Lionetti, D.; Rittle, J.; Agapie, T. Heterometallic Triiron-Oxo/hydroxo Clusters: Effect of Redox-Inactive Metals. *J. Am. Chem. Soc.* **2013**, *135* (51), 19075–19078.

(48) Delgado, M.; Ziegler, J. M.; Seda, T.; Zakharov, L. N.; Gilbertson, J. D. Pyridinediimine Iron Complexes with Pendant Redox-Inactive Metals Located in the Secondary Coordination Sphere. *Inorg. Chem.* **2016**, *55* (2), 555–557.

(49) Lacy, D. C.; Park, Y. J.; Ziller, J. W.; Yano, J.; Borovik, a S. Assembly and Properties of Heterobimetallic Co(II)/(III)/Ca(II) Complexes with Aquo and Hydroxo Ligands. *J. Am. Chem. Soc.* **2012**, *134* (42), 17526–17535.

(50) Cook, S. A.; Borovik, A. S. Molecular Designs for Controlling the Local Environments around Metal Ions. *Acc. Chem. Res.* **2015**, *48* (8), 2407–2414.

(51) MacBeth, C. E.; Golombek, A. P.; Young Jr., V. G.; Yang, C.; Kuczera, K.; Hendrich, M. P.; Borovik, A. S. O2 Activation by Nonheme Iron Complexes: A Monomeric Fe(III)-Oxo Complex Derived from O2. *Science.* **2000**, *289* (5481), 938–941.

(52) Gupta, R.; MacBeth, C. E.; Young, V. G.; Borovik, A. S. Isolation of Monomeric Mn(III)/(II)−OH and Mn(III)−O Complexes from Water: Evaluation of O−H Bond Dissociation Energies. *J. Am. Chem. Soc.* **2002**, *124* (7), 1136–1137.

(53) Parsell, T. H.; Behan, R. K.; Green, M. T.; Hendrich, M. P.; Borovik, A. S. Preparation and Properties of a Monomeric Mn(IV)-Oxo Complex. *J. Am. Chem. Soc.* **2006**, *128* (27), 8728–8729.

(54) Taguchi, T.; Gupta, R.; Lassalle-Kaiser, B.; Boyce, D. W.; Yachandra, V. K.; Tolman, W. B.; Yano, J.; Hendrich, M. P.; Borovik, A. S. Preparation and Properties of a Monomeric High-Spin Mn(V)-Oxo Complex. *J. Am. Chem. Soc.* **2012**, *134* (4), 1996–1999.

(55) Lacy, D. C.; Gupta, R.; Stone, K. L.; Greaves, J.; Ziller, J. W.; Hendrich, M. P.; Borovik, A. S. Formation, Structure, and EPR Detection of a High Spin Fe(IV)-Oxo Species Derived from Either an Fe(III)-Oxo or Fe(III)-OH Complex. *J. Am. Chem. Soc.* **2010**, *132* (35), 12188–12190.

(56) Shook, R. L.; Borovik, A. S. The Effects of Hydrogen Bonds on Metal-Mediated O2 Activation and Related Processes. *Chem. Commun.* **2008**, No. 46, 6095.

(57) Shirin, Z.; Hammes, B. S.; Young, V. G.; Borovik, A. S. Hydrogen Bonding in Metal Oxo Complexes: Synthesis and Structure of a Monomeric Manganese(III)−Oxo Complex and Its Hydroxo Analogue. *J. Am. Chem. Soc.* **2000**, *122* (8), 1836–1837.

(58) Park, Y. J.; Cook, S. A.; Sickerman, N. S.; Sano, Y.; Ziller, J. W.; Borovik, A. S. Heterobimetallic Complexes with M(III)-(μ-OH)-M(II) Cores (M(III) = Fe, Mn, Ga; M(II) = Ca, Sr, and Ba): Structural, Kinetic, and Redox Properties. *Chem. Sci.* **2013**, *4* (2), 717–726.

(59) Lau, N.; Ziller, J. W.; Borovik, A. S. Sulfonamido Tripods: Tuning Redox Potentials via Ligand Modifications. *Polyhedron* **2015**, *85*, 777–782.

(60) Sickerman, N. S.; Peterson, S. M.; Ziller, J. W.; Borovik, A. S. Synthesis, Structure and Reactivity of Fe(II/III)–NH3 Complexes Bearing a Tripodal Sulfonamido Ligand. *Chem. Commun.* **2014**, *50* (19), 2515.

(61) Cook, S. A.; Ziller, J. W.; Borovik, A. S. Iron(II) Complexes Supported by Sulfonamido Tripodal Ligands: Endogenous versus Exogenous Substrate Oxidation. *Inorg. Chem.* **2014**, *53* (20), 11029–11035.

(62) Sano, Y.; Weitz, A. C.; Ziller, J. W.; Hendrich, M. P.; Borovik, A. S. Unsymmetrical Bimetallic Complexes with M(II)–(μ-OH)–M(III) Cores (M(II)M(III) = Fe(II)Fe(III), Mn(II)Fe(III), Mn(II)Mn(III)): Structural, Magnetic, and Redox Properties. *Inorg. Chem.* **2013**, *52* (18), 10229–10231.

CHAPTER 2

Modulating the Primary and Secondary Coordination Spheres within a Series of Co^{II}–OH Complexes

Introduction

The properties and functions of metal complexes are achieved through control of the primary and secondary coordination sphere around the metal ions.[1–7] As discussed in Chapter 1, there is extensive research on controlling properties and function of metal ions using primary coordination sphere effects. However, much less is known about how the secondary coordination sphere influences reactivity and properties of metal ions. One type of important secondary coordination sphere interaction is the hydrogen bond (H-bond), which is an attractive interaction between a hydrogen atom bound to an electronegative element and another electronegative group. Many different ligand systems have been prepared containing H-bond donor and acceptors in order to probe the effect of H-bonds on metal ion properties.[1–6,8–15] For example, Fout has reported a tripodal pyrrole based ligand system that has a flexible secondary coordination sphere featuring three H-bond accepting imine moieties when it is bound in its anionic form to the metal ion (Scheme 2.1). However, when the ligand is bound in its neutral form, the ligand tautomerizes, resulting in a secondary coordination sphere defined by H-bond donors.[8,16,17] Anionic and neutral binding modes result in formation of stable Fe^{II} complexes with axial aquo, hydroxido, or triflate ligands.

Scheme 2.1. Tripodal Ligand Platform Developed by Fout[8]

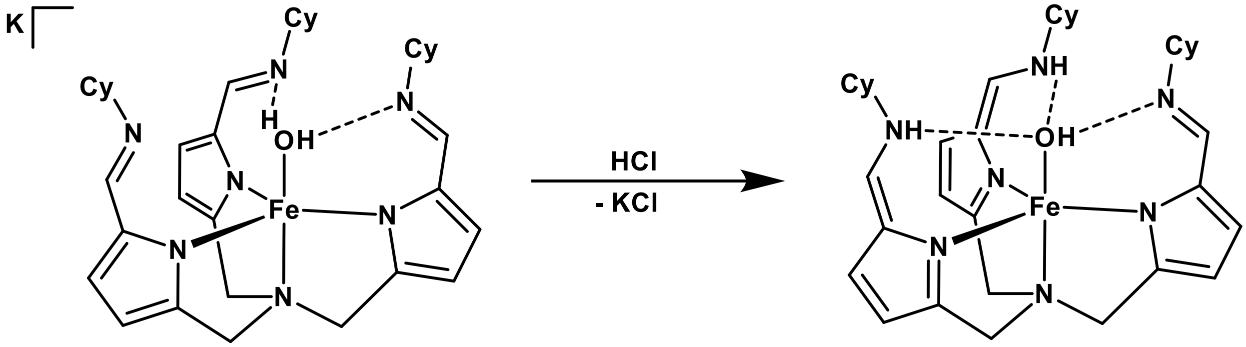

Our group has developed a family of tripodal ligands with differing numbers of H-bond donors to probe how systematic changes in H-bonding networks affect metal complex function.[1–5,7] By varying the number of urea and amide moieties in a series of tripodal ligands, Co^{II} complexes containing similar primary coordination spheres, but with a range of zero to three intramoleular H-bonds could be prepared. Co^{III}–OH complexes with increased number of H-bond donors showed increased stability and a 0.25 V cathodic shift in their one-electron reduction potentials.[7] Additionally, two tripodal ligands containing either H-bond donating groups or accepting groups have been synthesized. The tripodal sulfonamide-based ligand (*N,N′,N″*-(nitrilotris(ethane-2,1-diyl))tris(2,4,6-trimethylbenzene-sulfonamido)) $[MST]^{3-}$ (Figure 2.1A) utilizes sulfonamide oxygen atoms as H-bond acceptors. This ligand system has been shown to stabilize metal-aqua complexes with Mn^{II}, Fe^{II}, and Co^{II} ions.[18] In the tripodal urea-based ligand $[H_3buea]^{3-}$ (tris[(*N'*-*tert*-butylureaylato)-*N*-ethylene]aminato) (Figure 2.1B), the urea NH groups can be H-bond donors. These H-bond donating groups stabilize metal-oxo complexes of $Mn^{III}/Mn^{IV}/Mn^{V}$ and Fe^{III}/Fe^{IV} ions and hydroxido complexes of $Mn^{II}/Mn^{III}/Mn^{IV}$, $Fe^{II}/Fe^{III}/Fe^{IV}$, and Co^{II}/Co^{III} ions.[19–22] The anionic urea nitrogen atoms in the $[H_3buea]^{3-}$ ligand are more electron-donating because they are stronger bases than the anionic sulfonamide nitrogen atoms in the $[MST]^{3-}$ ligand, making M^{II} complexes with the $[H_3buea]^{3-}$ ligand more potent reducing agents.[23] This can be seen by a comparison of one-electron reduction potentials of M^{II} complexes with the $[MST]^{3-}$ and $[H_3buea]^{3-}$ ligands.[24,25]

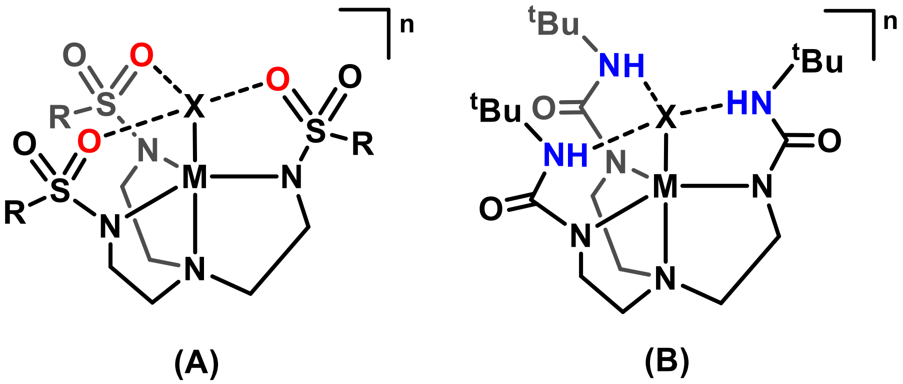

Figure 2.1. Structure of metal complexes made with (A) $[MST]^{3-}$ and (B) $[H_3buea]^{3-}$ with H-bond donating (blue) and hydrogen bond accepting (red) moieties highlighted. R = -Mesityl.

In this chapter, a new series of hybrid tripodal ligands that contain both urea and sulfonamide groups was prepared to further examine the effect of intramolecular H-bonding groups on the properties of a series of Co^{II}–OH complexes. The two new hybrid ligands N-(2–(bis(2–(3–(*tert*-butyl)ureido)ethyl)amino)ethyl)-4-methylbenzene-sulfonamido ($[H_2\mathbf{2}^{tol}]^{3-}$) and N,N′-((2–(3–(*tert*-butyl)ureido)ethyl)azanediyl)bis(ethane-2,1-diyl))bis(4-methylbenzenesulfonamido) ($[H\mathbf{1}^{tol}]^{3-}$) include aspects of $[H_3buea]^{3-}$ and $[MST]^{3-}$ described above. The ligand $[H_2\mathbf{2}^{tol}]^{3-}$ includes two H-bond donors from urea groups and a single H-bond acceptor from a sulfonamido group. The ligand $[H\mathbf{1}^{tol}]^{3-}$ contains two sulfonamido moieties and one urea unit (Figure 2.2). This series of ligands allowed us to probe the structural and physical effects of having H-bond donors and acceptors within the same ligand. As mentioned before, a sulfonamido is a weaker donor than a urea, and using the series of four ligands the donor strength of sulfonamido and urea nitrogens can be quantitatively assessed through electronic absorbance spectroscopy.

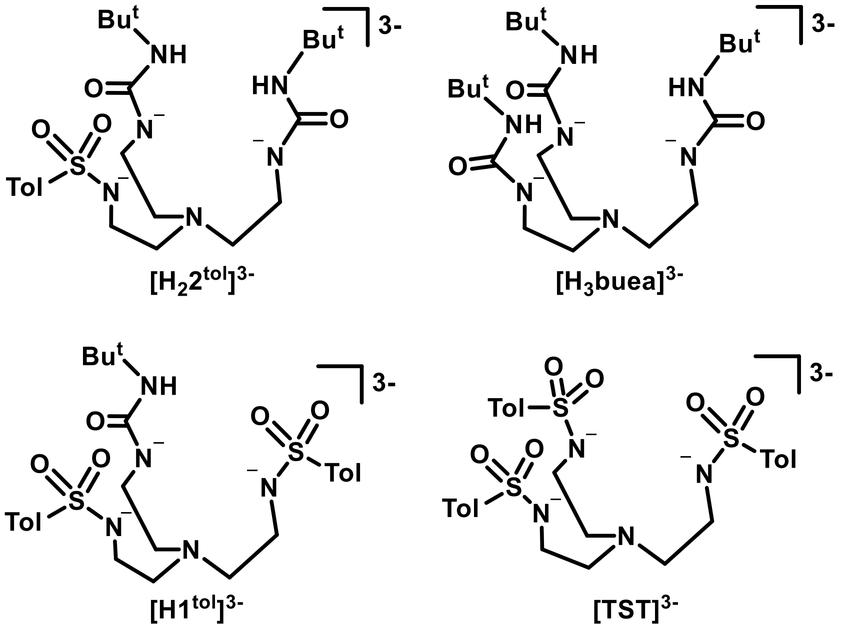

$[H_2\mathbf{2}^{tol}]^{3-}$ $[H_3buea]^{3-}$ $[H\mathbf{1}^{tol}]^{3-}$ $[TST]^{3-}$

Figure 2.2. The tripodal ligands used in this study, including the previously reported $[TST]^{3-}$ and $[H_3buea]^{3-}$.[26,27]

Results and Discussion

Ligand Design and Synthesis. Our group has previously utilized symmetrical tripodal ligands based on amides,[7,28–30] ureas,[4,27] and sulfonamides[4,31] to study the effect of the secondary coordination sphere on the properties of metal ions. In addition, hybrid ligand systems containing urea and other functionalities such as amido or pyridylcarboxyamido units have been synthesized and studied.[7,32] In this study, the new hybrid ligands $[H\mathbf{1}^{tol}]^{3-}$ and $[H_2\mathbf{2}^{tol}]^{3-}$, which contain both urea and sulfonamide groups, were prepared as well as their corresponding Co^{II}–OH complexes. Combining urea and sulfonamide moieties allows for systematic modulation of the secondary coordination sphere through variation of the intramolecular H-bonding network that surrounds the Co^{II}–OH units.

The preparation of $H_4\mathbf{1}^{tol}$ followed a four-step route (Scheme 2.2) that began with treating tris(2–aminoethyl)amine (tren) with di-*tert*-butyl dicarbonate to afford the monoboc protected species **4** (76% yield), which is converted to disulfonamide **5** (84%

yield) after addition of 2 equiv of 4-toluenesulfonyl chloride. Compound **5** was deprotected (95% yield) with trifluoroacetic acid (TFA) and then treated with *tert*-butyl isocyanate to afford H_4**1**^{tol} (82% yield) after purification. The preparation of H_5**2**^{tol} was achieved from the diurea compound **7** and 1 equiv of 4-toluenesulfonyl chloride to give H_5**2**^{tol} (70% yield) after purification (Scheme 2.2).

Scheme 2.2. Preparative route to H_41^{tol} and H_52^{tol}

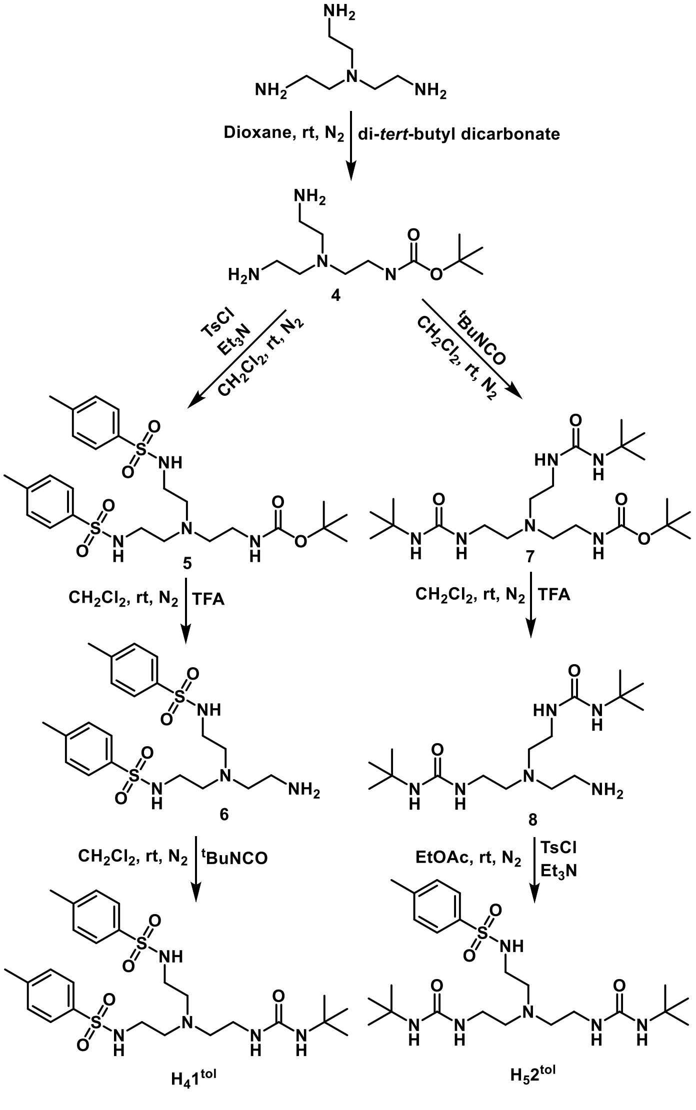

The syntheses of the Co^{II} complexes is outlined in Scheme 2.3. The Co^{II}–OH complex of $[TST]^{3-}$ was synthesized under an argon atmosphere by first deprotonating the ligand precursor with 3 equiv of KH and then adding solid $Co(OAc)_2$ to produce a dark blue solution and a white solid (KOAc, 2 equiv). After filtration to remove KOAc, the solution was treated with 1 equiv of H_2O, which induced a color change to pink. An additional equiv of KH was added to the mixture and stirred until gas evolution ceased to give a purple solution. $K_2[Co^{II}TST(OH)]$ was purified by recrystallization using vapor diffusion of Et_2O in a dimethylacetamide (DMA) solution of the salt.

Scheme 2.3. Preparative Routes to Co^{II}–OH Complexes[a]

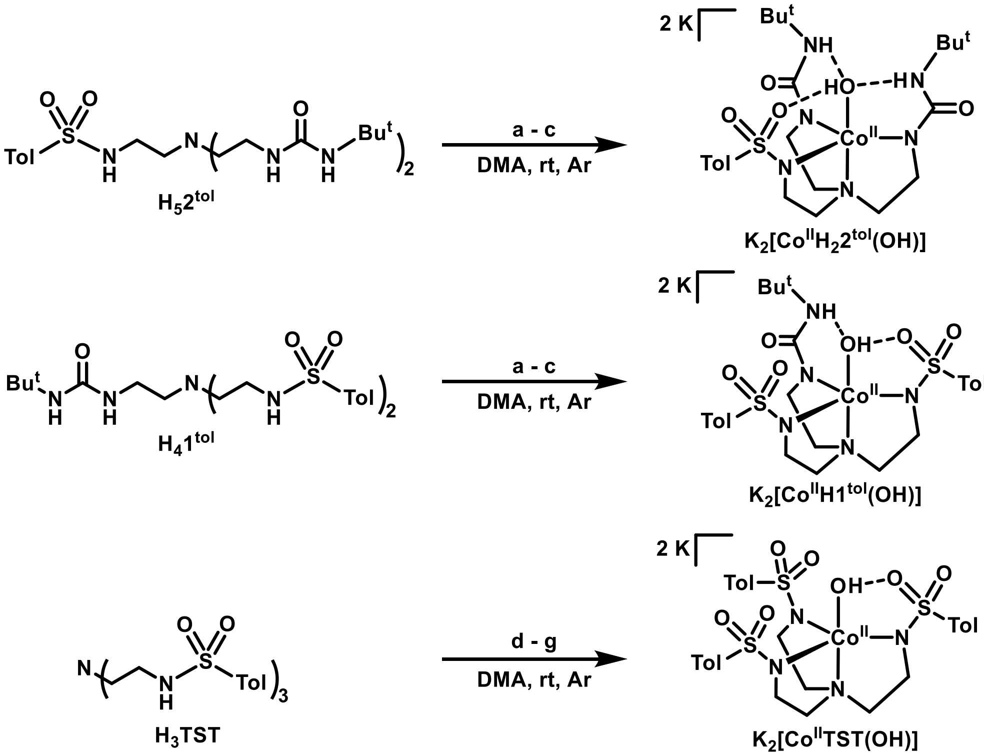

[a]Reagents: (a) 4 KH; (b) $Co(OAc)_2$; (c) H_2O; (d) 3 KH; (e) $Co(OAc)_2$; (f) H_2O; (g) KH. The synthesis of $[Co^{II}H_3buea(OH)]^{2-}$ has already been reported.[27]

The remaining Co^{II}–OH complexes were prepared by deprotonating the ligand precursor with 4 equiv of KH, followed by addition of solid $Co(OAc)_2$ to produce a blue solution and solid KOAc (2 equiv). After filtration, $K_2[Co^{II}H\mathbf{1}^{tol}(OH)]$, $K_2[Co^{II}H_2\mathbf{2}^{tol}(OH)]$, and $K_2[Co^{II}H_3buea(OH)]$ were formed after addition of 1 equiv of H_2O and recrystallized using the method described for $K_2[Co^{II}TST(OH)]$. All the Co^{II}–OH complexes are high-spin S = 3/2, as determined by their room temperature magnetic moments, which range from 4.10 to 4.49 μ_B, and their perpendicular mode electron paramagnetic resonance (EPR) spectra measured at 77 K, which contain a prominent feature at g = 3.9.

Structural Properties. The molecular structures of the Co^{II}–OH complexes were examined using X-Ray diffraction methods. Single crystals of $K_2[Co^{II}H\mathbf{1}^{tol}(OH)]$ could not be obtained and the structure of $K_2[Co^{II}H_3buea(OH)]$ was reported previously.[27] The molecular structures of $[Co^{II}TST(OH)]^{2-}$, $[Co^{II}H_2\mathbf{2}^{tol}(OH)]^{2-}$, and $[Co^{II}H_3buea(OH)]^{2-}$ reveal that the coordination environment around the Co^{II} ion adopts a trigonal bipyramidal geometry (Figure 2.3), with the trigonal plane formed by three anionic nitrogen donors. Analysis of the Co1–N_{trig} distances in the trigonal plane reveal that there are statistically significant differences in Co1–N_{trig} bond lengths for urea and sulfonamido donors. Those involving a deprotonated urea are shorter than those involving a deprotonated sulfonamide. The average Co1–N_{trig} distance is 2.057(2) Å in $[Co^{II}H_3buea(OH)]^{2-}$ and 2.118(6) Å in $[Co^{II}TST(OH)]^{2-}$.

The Co1–O1 distance is related to the amount of H-bonding to the hydroxido ligand. As the number of H-bonds donated to the hydroxido ligand increase, the Co1–O1 distance should also increase because the anionic charge of the hydroxido decreases with the number of H-bond donors. Conversely, if an H-bond from the hydroxido ligand is accepted by an oxygen atom of a sulfonamido arm, the Co1–O1 distance should decrease. Specifically, for $[Co^{II}H_3buea(OH)]^{2-}$, the two H-bonds donated by the urea NH donors result in the longest Co1–O1 distance of the series at 2.051(3) Å. However, the Co1–O1 bond length contracts to 2.015(2) Å in $[Co^{II}H_2\mathbf{2}^{tol}(OH)]^{2-}$, which contains two intramolecular H-bond donors and one acceptor, due to the presence of a sulfonamido group that serves as a H-bond acceptor. Finally, the complex $[\mathrm{Co^{II}TST(OH)}]^{2-}$ has the shortest Co1–O1 bond length at 1.953(4) Å, since no H-bonds are donated to the hydroxido ligand and one intramolecular H-bond is accepted from the hydroxido ligand to a sulfonamido oxygen atom (O2). This single H-bond has an O1⋯O2 distance of 2.808(6) Å that is significantly shorter than the distance of 2.950(2) Å that is observed in $[\mathrm{Co^{II}H_2}\mathbf{2}^{\mathrm{tol}}\mathrm{(OH)}]^{2-}$.

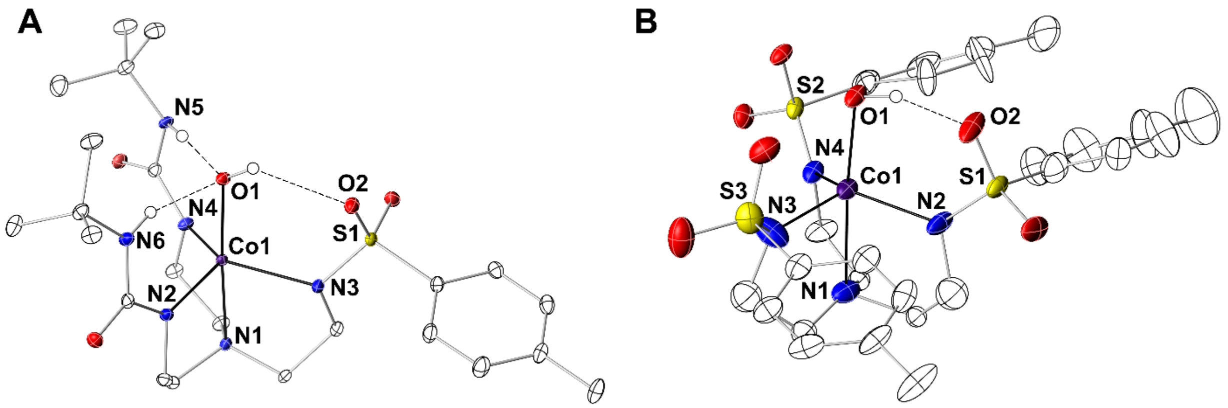

Figure 2.3. Thermal ellipsoid plots of $[\mathrm{Co^{II}H_2}\mathbf{2}^{\mathrm{tol}}\mathrm{(OH)}]^{2-}$ (A) and $[\mathrm{Co^{II}TST(OH)}]^{2-}$ (B). Thermal ellipsoids are drawn at the 50% probability level, and only urea and hydroxido hydrogen atoms are shown for clarity.

A trend in the displacement of cobalt ion towards the trigonal plane formed by the three anionic nitrogen atoms was observed. $[\mathrm{Co^{II}TST(OH)}]^{2-}$ has the greatest displacement of 0.440 Å towards O1, whereas in the other structures the out of plane distance shortens with an increasing number of NH⋯O1 H-bonds: 0.351 Å in $[\mathrm{Co^{II}H_2}\mathbf{2}^{\mathrm{tol}}\mathrm{(OH)}]^{2-}$ and 0.346 Å in $[\mathrm{Co^{II}H_3buea(OH)}]^{2-}$. The greatest out of plane distance in $[\mathrm{Co^{II}TST(OH)}]^{2-}$ could arise from the contraction in Co1–O1 distance and the hydroxido ligand being locked in place due to an intramolecular H-bond allowing only the $\mathrm{Co^{II}}$ ion to move out of the plane.

Table 2.1. Selected Bond Distances and Angles for the Three $\mathrm{Co^{II}}$–OH Complexes

Distances (Å) or angles (deg)	$[\mathrm{Co^{II}TST(OH)}]^{2-}$	$[\mathrm{Co^{II}H_2}\mathbf{2}^{\mathrm{tol}}\mathrm{(OH)}]^{2-}$	$[\mathrm{Co^{II}H_3buea(OH)}]^{2-\,a}$
Co1–N1	2.224(5)	2.213(2)	2.216(5)
Co1–N2	2.081(5)	2.039(2)	2.079(4)
Co1–N3	2.147(4)	2.175(2)	2.075(4)
Co1–N4	2.128(6)	2.049(2)	2.046(4)
Co1–O1	1.953(4)	2.015(2)	2.051(4)
d(O1···O2)	2.808(6)	2.950(2)	–
d(O1···N5)	–	2.741(2)	2.829(5)
d(O1···N6)	–	2.851(3)	2.781(5)
d(O1···N7)	–	–	2.802(5)
N1–Co1–N2	78.7(2)	80.74(6)	80.2(1)
N1–Co1–N3	78.43(18)	79.12(6)	80.7(1)
N1–Co1–N4	78.5(2)	81.04(6)	80.2(2)
N2–Co1–N3	126.7(2)	108.69(6)	108.1(1)
N2–Co1–N4	110.6(3)	117.79(7)	125.0(2)
N3–Co1–N4	111.6(2)	125.09(6)	108.1(1)
O1–Co1–N1	172.1(2)	176.40(6)	179.3(1)

[a] ref. [33]

Our group[3] and others in the literature[34] have found correlations between M–OH_n bond lengths and the number of intramolecular H-bonds. A progressive lengthening of the M–O(H) bond is observed as the number of intramolecular H-bonds to the hydroxido ligand increases because the H-bonds removes electron density from the hydroxido ligand, which makes the ligand a weaker donor to the metal ion. This weaker donation to the metal ion results in a lengthening of the M–O(H) bond. The hydroxido ligand can also function as a H-bond donor, which changes the properties of the hydroxido ligand. When the hydroxido ligand serves as a H-bond donor, the hydroxido ligand becomes more basic because the H-bond reduces the positive charge around the oxygen from proton that is involved in the H-bond interaction. This interaction causes the hydroxido ligand to become more anionic and thereby results in a contraction of the Co1–O1 distance. This contraction in the Co1–O1 distance is observed from $[\mathrm{Co^{II}H_3buea(OH)}]^{2-}$ to $[\mathrm{Co^{II}H_2}\mathbf{2}^{\mathrm{tol}}\mathrm{(OH)}]^{2-}$ and is attributed to the hydroxido ligand serving as a H-bond donor in $[\mathrm{Co^{II}H_2}\mathbf{2}\mathrm{(OH)}]^{2-}$. However, this effect is minimized by the presence of two intramolecular H-bonds that are formed from urea NH groups to the hydroxido ligand in $[Co^{II}H_2\mathbf{2}^{tol}(OH)]^{2-}$. Without any urea groups in $[Co^{II}TST(OH)]^{2-}$, the Co1–O1 distance is significantly shorter and the strongest H-bond from the hydroxido ligand is formed. The different intramolecular H-bond networks also affect the N1–Co1–O1 angles, which are the smallest in $[Co^{II}TST(OH)]^{2-}$ and progressively increase with the number of urea groups. These structural trends suggest that the types of intramolecular H-bonds formed with hydroxido ligand affect the properties of the hydroxido ligand, thereby resulting in changes in structural properties.

Vibrational Properties. Fourier transform infrared spectroscopy (FTIR) was used to further probe the vibrations of the O–H bond (ν(OH)) in the solid state (Table 2.2). The energy of the vibration is directly related to the strength of the O–H bond, while the broadness of the vibrational band as measured by the full-width-at-half max (FWHM) correlates with the strength of the H-bond formed by the hydroxido ligand. The lowest energy ν(O–H) of 3574 cm^{-1} is observed with $[Co^{II}TST(OH)]^{2-}$, which also has the broadest peak with a full-width-at-half max value of 24 cm^{-1}. In $[Co^{II}H\mathbf{1}^{tol}(OH)]^{2-}$, a split band is observed at a higher energy of 3581 and 3602 cm^{-1}, and for $[Co^{II}H_2\mathbf{2}^{tol}(OH)]^{2-}$, a single band is observed at 3625 cm^{-1} with a full-width-at-half max value of 9 cm^{-1}, suggesting that the H-bond formed from the hydroxido ligand is weaker than the one formed in $[Co^{II}TST(OH)]^{2-}$. This is supported by the structural data that shows a shorter O1⋯O2 distance in $[Co^{II}TST(OH)]^{2-}$. The ν(OH) in $[Co^{II}H_3buea(OH)]^{2-}$ was not observed.[27]

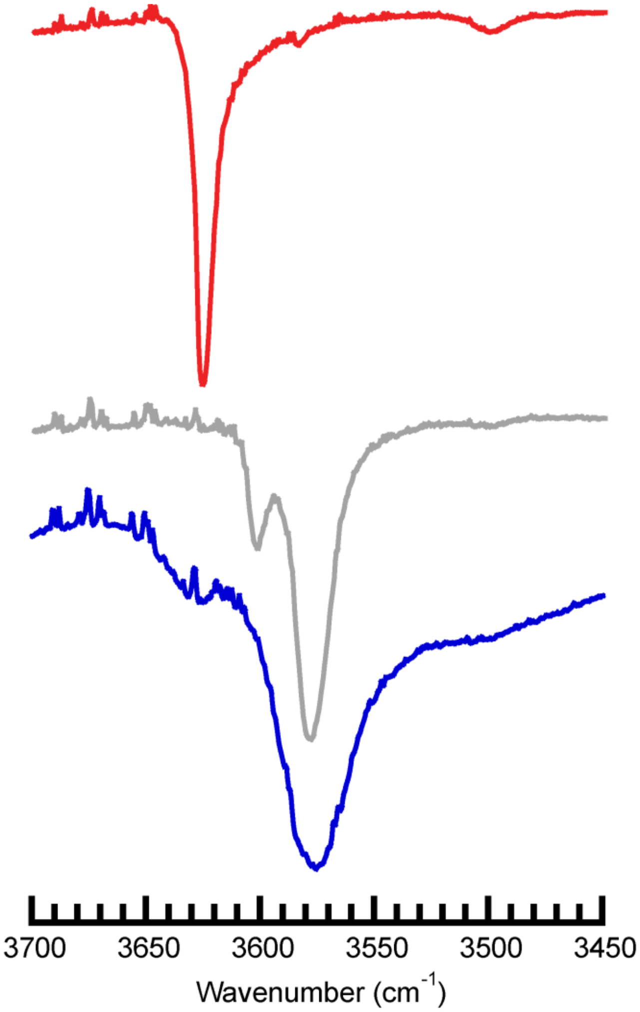

Figure 2.4. Solid state FTIR spectra of $K_2[Co^{II}H_22^{tol}(OH)]^{2-}$ (red line), $K_2[Co^{II}H1^{tol}(OH)]$ (grey line), and $K_2[Co^{II}TST(OH)]$ (blue line) showing the ν(O–H) stretch.

Lower energy ν(O–H) bands are correlated with shorter Co–O(H) bond distances in this series. In contrast to the previous studies, which have hydroxido ligands that only accepts H-bonds from a urea NH donor, all the complexes described herein except $[Co^{II}H_3buea(OH)]^{2-}$ have ligands that accept a H-bond from the hydroxido ligand. Regardless, similar trends in the ν(OH) bands are observed. This vibrational analysis shows that $[Co^{II}TST(OH)]^{2-}$ has the lowest energy ν(O–H) band and shortest Co1–O1 bond length, consistent with a strong intramolecular H-bond from the hydroxido ligand to a sulfonamido oxygen atom. In addition, the ν(O–H) bands broaden as the H-bond strengthens, which has also been shown in organic systems (e.g., NH···O=CR$_2$).[3] This broadening effect has been attributed to an increase in the strength of H-bonds.

Table 2.2. Vibrational Properties of the Co^{II}–OH Complexes

	ν(O–H) (FWHM, cm^{-1})
$[\mathrm{Co^{II}TST(OH)}]^{2-}$	3574 (24)
$[\mathrm{Co^{II}H}\mathbf{1}^{\mathrm{tol}}\mathrm{(OH)}]^{2-}$	3602, 3581 (16)
$[\mathrm{Co^{II}H_2}\mathbf{2}^{\mathrm{tol}}\mathrm{(OH)}]^{2-}$	3625 (9)
$[\mathrm{Co^{II}H_3buea(OH)}]^{2-}$	N/A

Electronic Absorbance Properties. The electronic absorbance spectra for the Co^{II}–OH complexes measured in DMA are characterized by d–d bands at $\lambda_{max} \sim$ 470, 550, and 600 nm, with extinction coefficients of less than 200 M^{-1} cm^{-1} (Figure 2.5 and Table 2.3). In addition, each complex contains a very weak d–d band between $\lambda_{max} \sim$ 700-900 nm with extinction coefficients less than 100 M^{-1} cm^{-1} that is also present in previously reported Co^{II}–OH complexes with trigonal bipyramidal geometry.[27]

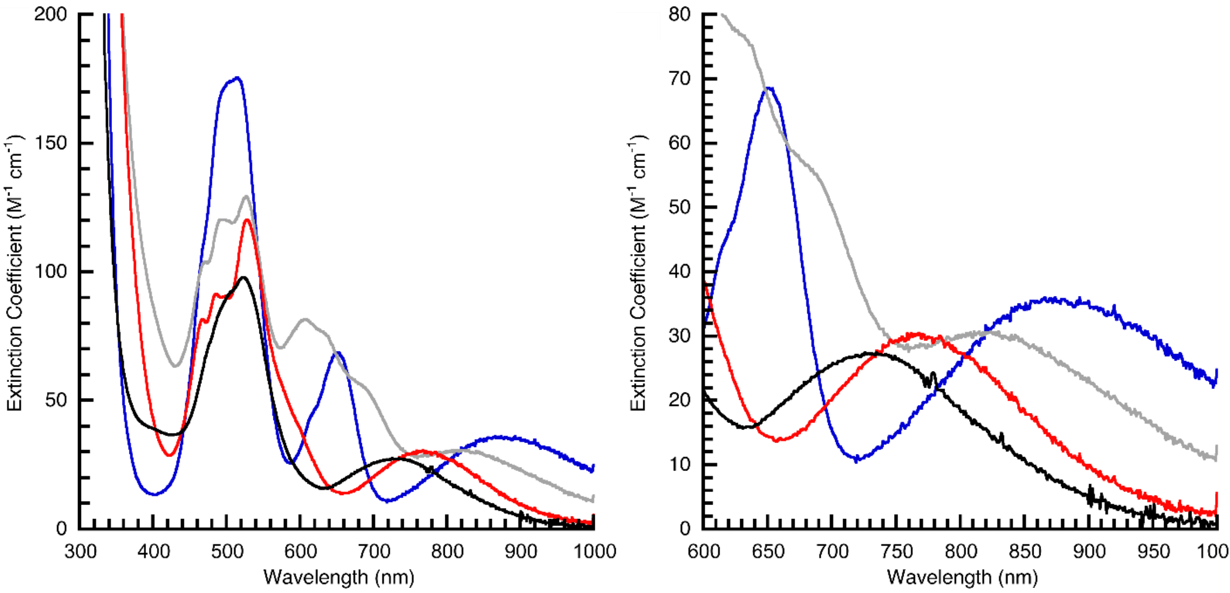

Figure 2.5. Electronic absorbance spectra for $[\mathrm{Co^{II}H_3buea(OH)}]^{2-}$ (black line), $[\mathrm{Co^{II}H_22^{tol}(OH)}]^{2-}$ (red line), $[\mathrm{Co^{II}H1^{tol}(OH)}]^{2-}$ (grey line), and $[\mathrm{Co^{II}TST(OH)}]^{2-}$ (blue line) recorded in DMA.

The low-energy band can be used to evaluate the effect of the deprotonated urea and sulfonamido donors to the ligand field. For a high-spin Co^{II} ion in C_{3v} symmetry, ligand field theory predicts that this band should arise from the $^4A_1 \longrightarrow {}^4E$ transition (Figure 2.6 and Table 2.3). The energy of this transition is sensitive to the types of donors in the trigonal plane made up of the three anionic nitrogen donors. In the qualitative analysis that follows, only the σ-interactions were considered with π-interactions associated with the axial ligands assumed to remain constant. This analysis suggests that deprotonated urea donors are stronger field ligands than deprotonated sulfonamide donors, as the low-energy band shifts to higher energy upon substitution with more deprotonated urea donors. This blue-shift is indicative of a larger energy gap in the d-orbital manifold, which suggests improved electron-donating properties of the ligand. The low-energy electronic absorbance band for the symmetric urea-based system $[\mathrm{Co^{II}H_3buea(OH)}]^{2-}$ is observed at 14,100 $\mathrm{cm^{-1}}$ (710 nm) and shifts to 11,200 $\mathrm{cm^{-1}}$ (890 nm) in the symmetric sulfonamido-based system $[\mathrm{Co^{II}TST(OH)}]^{2-}$. The two complexes that contain hybrid ligands have absorbance bands that are observed at energies in between those of the symmetric systems. $[\mathrm{Co^{II}H_2}\mathbf{2}^{\mathrm{tol}}\mathrm{(OH)}]^{2-}$ and $[\mathrm{Co^{II}H}\mathbf{1}^{\mathrm{tol}}\mathrm{(OH)}]^{2-}$ have transitions at 13,000 $\mathrm{cm^{-1}}$ (767 nm) and 12,200 $\mathrm{cm^{-1}}$ (820 nm), respectively. This incremental increase of approximately 1000 $\mathrm{cm^{-1}}$ observed for the band correlates with the number of deprotonated urea donors in the $\mathrm{Co^{II}}$–OH complexes. This effect reflects the increased basicity of a deprotonated urea compared to a deprotonated sulfonamide, resulting in a stronger field ligand.[23]

Table 2.3. Electronic Absorbance Properties of $\mathrm{Co^{II}}$–OH Complexes

	λ_{max} (nm), (E, $\mathrm{cm^{-1}}$)
$[\mathrm{Co^{II}TST(OH)}]^{2-}$	890, (11,200)
$[\mathrm{Co^{II}H}\mathbf{1}^{\mathrm{tol}}\mathrm{(OH)}]^{2-}$	820, (12,200)
$[\mathrm{Co^{II}H_2}\mathbf{2}^{\mathrm{tol}}\mathrm{(OH)}]^{2-}$	767, (13,000)
$[\mathrm{Co^{II}H_3buea(OH)}]^{2-}$	710, (14,100)

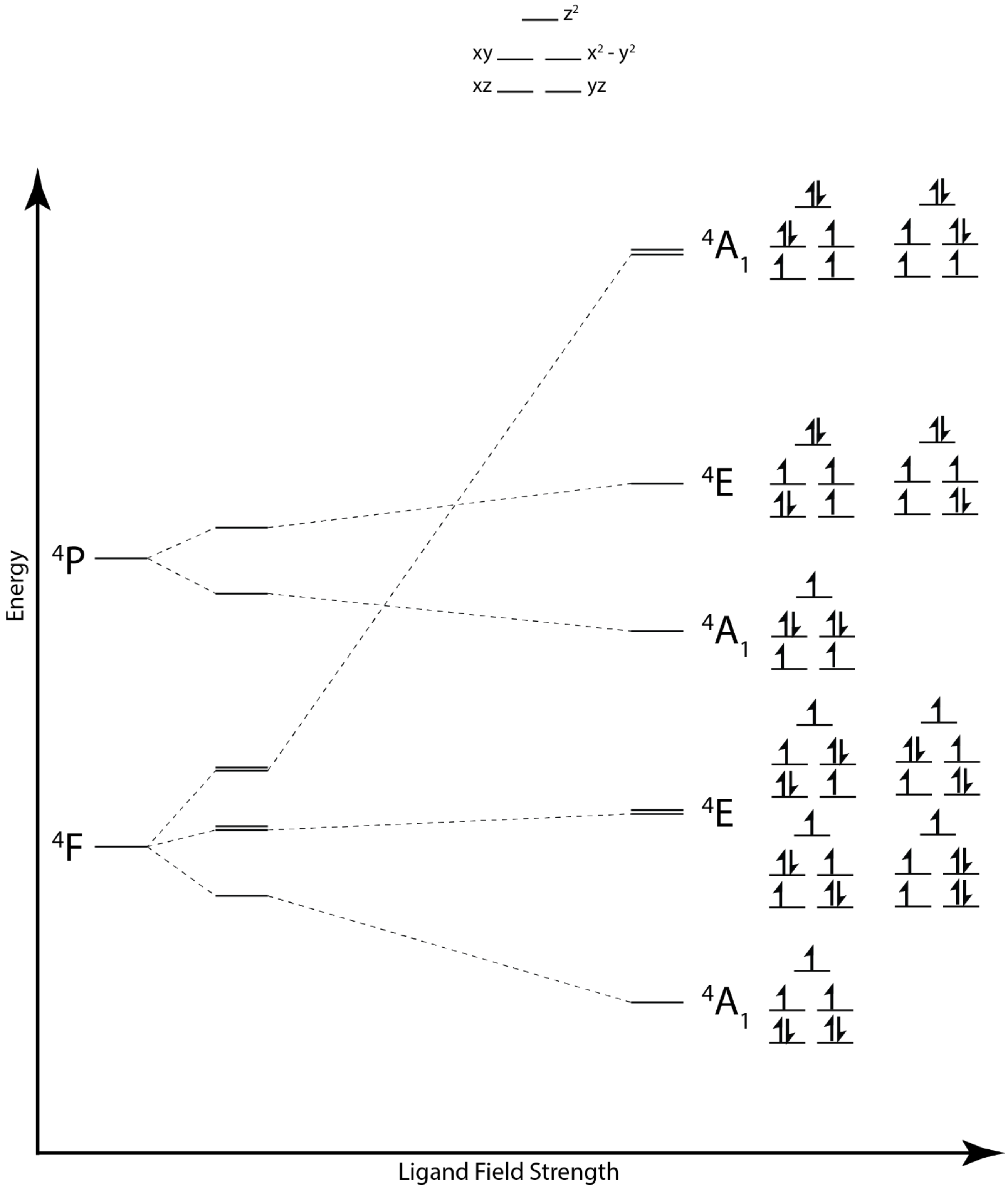

Figure 2.6. Qualitative energy diagram showing the predicted energy manifold for a Co^{II} ion in C_{3v} symmetry.

Electrochemical Properties: Cyclic voltammetry (CV) was used to evaluate the electrochemical properties of the Co^{II}–OH complexes. CV experiments were conducted in DMA at room temperature and showed a one-electron event that was assigned to the Co^{III}/Co^{II} redox couple (Figure 2.7 and Table 2.4). For all the complexes, the oxidative event was quasi-reversible, except $[Co^{II}TST(OH)]^{2-}$, which was irreversible. Thus, a comparison of the potential of peak anodic current (E_a) is most appropriate since it allows for comparison of all the Co^{II}–OH complexes. In this series, the E_a values range from −0.52 to −1.17 V vs $FeCp_2^+/FeCp_2$, illustrating the ability of this series of tripodal ligands to modulate the redox properties of the Co center. Consistent with the findings that the deprotonated urea groups are the strongest field ligands, $[Co^{II}H_3buea(OH)]^{2-}$ and $[Co^{II}H_2\mathbf{2}^{tol}(OH)]^{2-}$ are the best at stabilizing the Co^{III} oxidation state and have the most negative E_a values of −1.17 and −0.71 V vs $[FeCp_2]^{+/0}$. A single sulfonamido group causes a large shift in the E_a value by 0.46 V. The effect of adding more sulfoamido groups is diminished when comparing the E_a value of $[Co^{II}H_2\mathbf{2}^{tol}(OH)]^{2-}$ and $[Co^{II}(H\mathbf{1}^{tol})]^{2-}$ where a difference of only 0.13 V is observed. A difference of only 0.06 V is observed when comparing the E_a value of $[Co^{II}H\mathbf{1}^{tol}(OH)]^{2-}$ and $[Co^{II}TST(OH)]^{2-}$. The smaller changes in E_a values could be due to the hydroxido ligand donating more electron density to the Co center as the number of H-bonds from the urea to the hydroxido decreases. In addition, the H-bonding from the hydroxido to a sulfonamido oxygen atom also increases the amount of donation to the Co center.

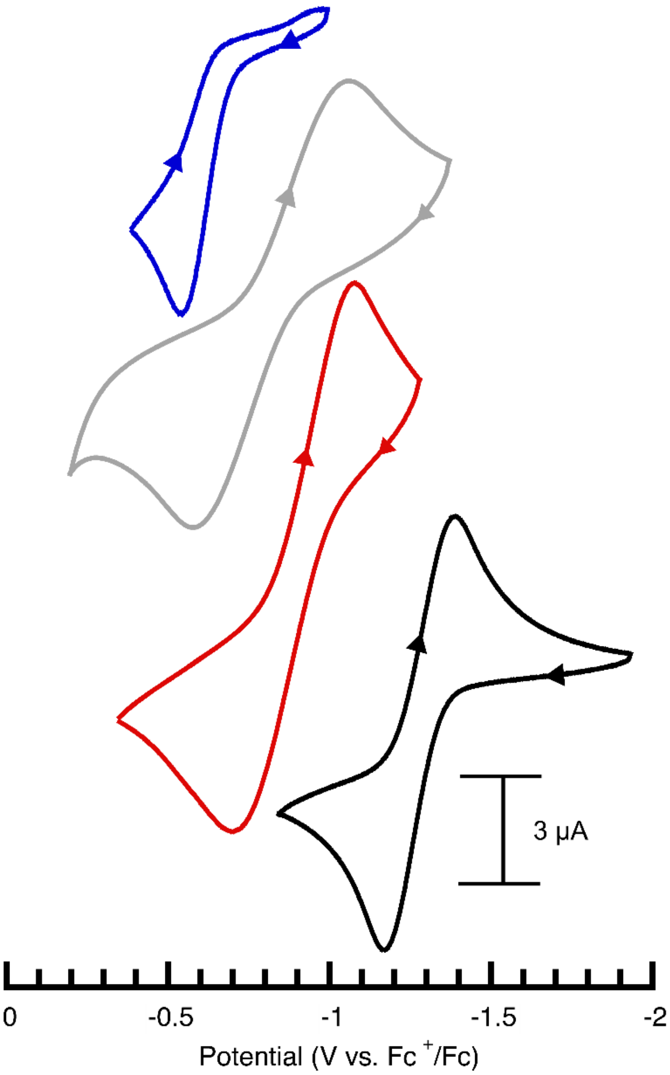

Figure 2.7. Cyclic voltammograms of $[Co^{II}H_3buea(OH)]^{2-}$ (black line), $[Co^{II}H_2\mathbf{2}^{tol}(OH)]2-$ (red line), $[Co^{II}H\mathbf{1}^{tol}(OH)]^{2-}$ (gray line), and $[Co^{II}TST(OH)]^{2-}$ (blue line) recorded in DMA. Measurements were done at room temperature under Ar, with a scan rate of 100 mV·s^{-1}.

Table 2.4. Electrochemical Properties of the Co^{II}–OH Complexes

	$E_{1/2}$ (E_a) (V vs $[FeCp_2]^{+/0}$)	ΔE (V), i_a/i_c
$[Co^{II}TST(OH)]^{2-}$	N/A (- 0.52)	–
$[Co^{II}H\mathbf{1}^{tol}(OH)]^{2-}$	- 0.905 (- 0.58)	0.485, 1.04
$[Co^{II}H_2\mathbf{2}^{tol}(OH)]^{2-}$	- 0.828 (- 0.71)	0.380, 1.12
$[Co^{II}H_3buea(OH)]^{2-}$	−1.28 (- 1.17)	0.215, 1.07

Oxidized Species. The results from the electrochemical experiments suggested that related Co^{III}–OH complexes could be accessed at reasonably negative potentials. However, the stabilities of the oxidized products differ throughout the series, which can be seen from the CV in Figure 2.7. For example, the CV of $[Co^{II}TST(OH)]^{2-}$ shows a completely irreversible redox event, which suggests that stability of the analogous Co^{III}–OH species is limited.

The CV data also suggested that $[FeCp_2]^+$ could be used as an oxidant for all four compounds, and the subsequent oxidation reactions were monitored spectrophotometrically. We have previously shown that $[Co^{III}H_3buea(OH)]^-$ is sufficiently stable enough at room temperature to obtain single crystals and determine the molecular structure.[7,27] A similar reaction at room temperature with $[Co^{II}H_2\mathbf{2}^{tol}(OH)]^{2-}$ produced a species with characteristic absorbance bands matching previously characterized Co^{III}–OH complexes with a trigonal bipyramidal coordination geometry (Figure 2.8).[7,27] This species slowly decayed in solution at room temperature with $t_{1/2} \sim 5$ d, and the isolation as single crystals was not possible (Figure 2.9A and Figure 2.10A). The oxidized form of $[Co^{II}H\mathbf{1}^{tol}(OH)]^{2-}$ had limited stability with a $t_{1/2} = 16$ min at 25 °C (Figure 2.9B and Figure 2.10B). The complexes $[Co^{III}H\mathbf{1}^{tol}(OH)]^-$ and $[Co^{III}TST(OH)]^-$ were only stable below – 50 °C. A direct comparison in the half-life of $[Co^{III}TST(OH)]^-$ to the others could not be made because the species decayed too quickly at room temperature to obtain a half-life. A $t_{1/2} = 13$ min was measured at – 20 °C for $[Co^{III}TST(OH)]^-$ (Figure 2.9B and Figure 2.10B).

The stability observed for the Co^{III}–OH complexes is similar to a previous study conducted by our group with Co^{III}–OH complexes with varying number of H-bond donors to the hydroxido ligand.[7] The study used urea/amidate tripodal ligands, where the number of intramolecular H-bond donors varied from zero to three. The stability of the complexes increases with the number of urea groups. The stability was attributed to the increasing number of intramolecular H-bond donors to the hydroxido ligand.

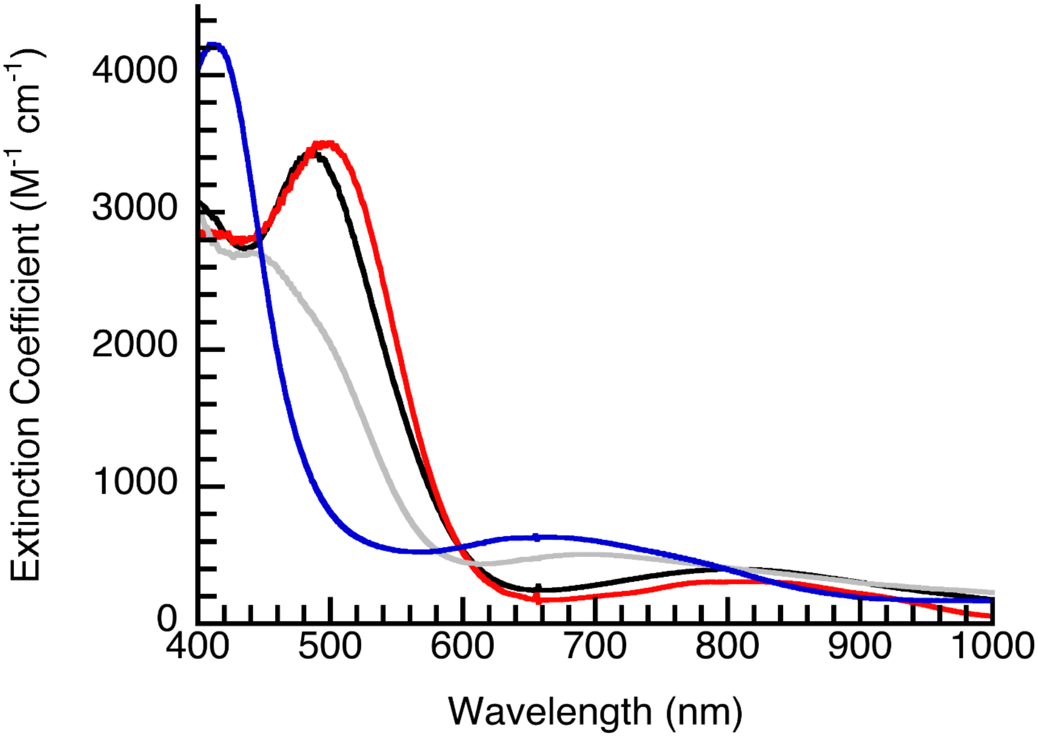

Figure 2.8. Electronic absorbance spectra for $[Co^{III}H_3buea(OH)]^-$ (black line), $[Co^{III}H_2\mathbf{2}^{tol}(OH)]^-$ (red line), $[Co^{III}H\mathbf{1}^{tol}(OH)]^-$ (grey line), $[Co^{III}TST(OH)]^-$ (blue line) recorded in a DMF:THF mixture at – 80 °C. Products were generated by oxidation of Co^{II}–OH compounds with $FeCp_2BF_4$.

With the series of Co^{III}–OH complexes presented in this chapter, the differing stabilities are less straightforward. The complexes $[Co^{III}H_3buea(OH)]^-$ and $[Co^{III}H_2\mathbf{2}^{tol}(OH)]^-$ contain the same number of intramolecular H-bonds, but they have very different stabilities. The types of intramolecular H-bond formed in the two complexes are different; $[Co^{III}H_3buea(OH)]^-$ has all H-bond donors to the hydroxido ligand, whereas $[Co^{III}H_2\mathbf{2}^{tol}(OH)]^-$ has two H-bond donors from ureas and one acceptor from a sulfonamido oxygen. In addition, there are large differences in the redox properties of the four complexes in the series that correlate with their stabilities. Therefore, the observed stabilities of the four Co^{III}–OH complexes likely result from a combination of influences from the primary and secondary coordination spheres.

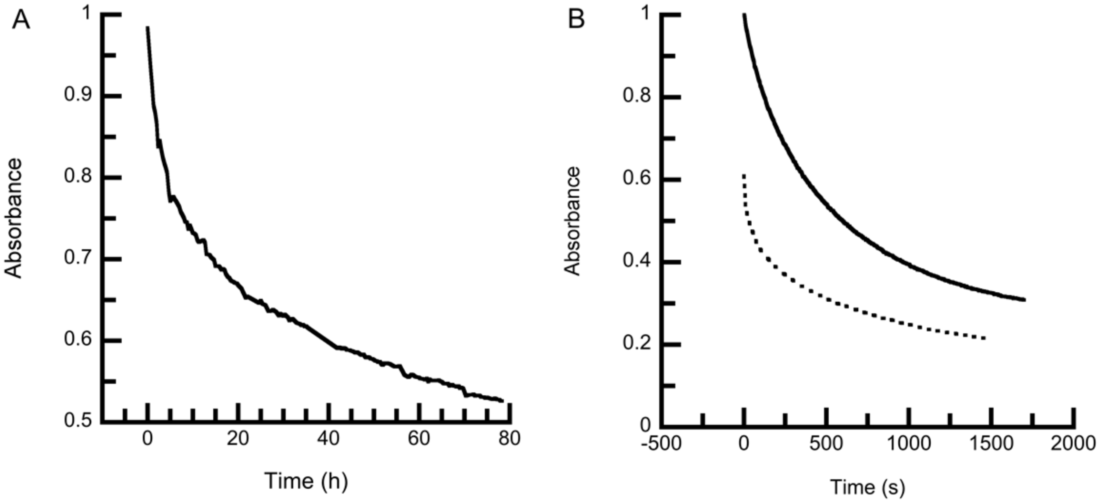

Figure 2.9. Data used to determine the rate constants for decay of (A) [Co^{III}H$_2$**2**^{tol}(OH)]$^-$ (25 °C), and (B) (–) [Co^{III}H**1**^{tol}(OH)]$^-$ (25 °C), (•) [Co^{III}TST(OH)]$^-$ (– 20 °C).

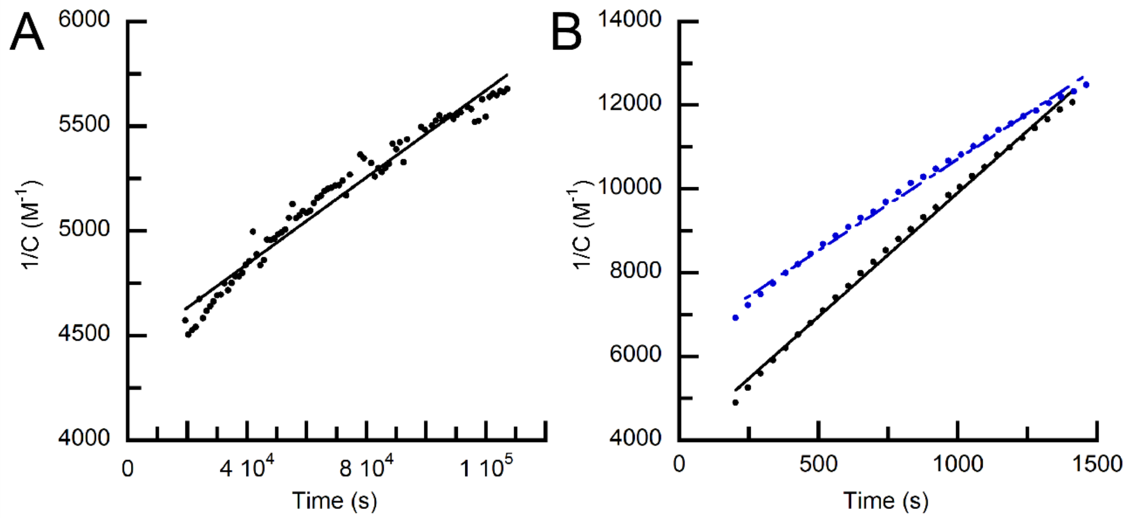

Figure 2.10. Linear fits used to determine the second order rate constants for decay of (A) [Co^{III}H$_2$**2**^{tol}(OH)]$^-$ (25 °C), and (B) (blue line) [Co^{III}H**1**^{tol}(OH)]$^-$ (25 °C), (black line) [Co^{III}TST(OH)]$^-$ (– 20 °C).

Table 2.5. Half-lives and λ_{max} and Extinction Coefficients for the Four Co^{III}–OH Complexes

	$t_{1/2}$ (m), (T, °C)	λ_{max} (nm) (M^{-1} cm^{-1})
[Co^{III}TST(OH)]$^-$	13, (– 20)	412 (4200), 663 (631)
[Co^{III}H**1**^{tol}(OH)]$^-$	16, (25)	448 (2700) ,693 (506)
[Co^{III}H$_2$**2**^{tol}(OH)]$^-$	7200, (25)	498 (3500), 788 (305)
[Co^{III}H$_3$buea(OH)]$^-$	N/A	485 (3400), 805 (398)

Summary and Conclusions

A preparative route to two new tripodal hybrid ligands [H**1**$^{\mathrm{tol}}$]$^{3-}$ and [H$_2$**2**$^{\mathrm{tol}}$]$^{3-}$ containing varying numbers of urea and sulfonamide groups was presented. Together with the symmetrical ligands [H$_3$buea]$^{3-}$ and [TST]$^{3-}$, they form a series of ligands that were used to probe the effects of H-bond donors and acceptors on the properties of Co$^{\mathrm{II}}$–OH complexes. The molecular structures of three of the four complexes were presented and showed that all the Co$^{\mathrm{II}}$–OH complexes have a trigonal bipyramidal primary coordination sphere, which is typical for complexes with these types of tripodal ligands. The structural data presented here suggest that the structural properties of the Co$^{\mathrm{II}}$–OH compounds are influenced by both the primary and secondary coordination spheres. For example, the combination of adding H-bond accepting moieties and decreasing H-bond donating groups in the secondary coordination sphere results in the shortening of the Co–O1 bond length. This effect was supported by the vibrational studies that showed commensurate changes in the energies and peak broadness associated with the ν(OH) that is bound to the Co$^{\mathrm{II}}$ center.

To assess the effect of changing the primary coordination sphere for the Co$^{\mathrm{II}}$–OH complexes, a qualitative ligand field approach was used to examine the changes in the $^4A_1 \longrightarrow {}^4E$ transition. This transition is studied because it is sensitive to the nature of the ligands in the trigonal plane. Based on this analysis, the deprotonated urea groups are stronger field ligands than the deprotonated sulfonamide groups. Each deprotonated urea within the trigonal plane increases the $^4A_1 \longrightarrow {}^4E$ transition by ~1000 cm^{-1}. Large shifts in the potentials of peak anodic current were observed, which can be explained by changes to both the primary and secondary coordination spheres. The Co$^{\mathrm{III}}$–OH analogs had varying stabilities that correlate with the number of urea groups in the ligands. In [Co$^{\mathrm{III}}$H$_3$buea(OH)]$^-$ the three urea groups stabilize the Co^{III} center enough to allow for isolation of crystalline solid at room temperature. However, adding more sulfonamide groups to the ligand drastically changes the Co^{III} complexes stability, which highlights the instability of trigonal bipyramidal Co^{III}–OH complexes. However, identification of a clear cause for the stability of the Co^{III}–OH complexes could not be obtained. These results illustrate the difficulty in assigning changes in properties and reactivity to a single source. The primary and secondary coordination spheres influence in these complexes are intertwined.

Experimental Section

Materials.

N,N'-(((2–aminoethyl)azanediyl)bis(ethane-2,1-diyl))bis(4-methylbenzene-sulfonamide) and the ligand precursors 1,1',1''-(nitrilotris(ethane-2,1-diyl))tris(3–(*tert*-butyl)urea) (H_6buea), *N,N',N''*-(nitrilotris(ethane-2,1-diyl)tris(4-methylbenzenesulfonamide) (H_3TST), and the metal complex $K_2[Co^{II}H_3buea(OH)]$ were synthesized using literature procedures.[26,27,36] For $K_2[Co^{II}H_3buea(OH)]$ a DMA/Et_2O diffusion was used to crystallize the salt instead of DMA-MeCN/Et_2O diffusion. The metal precursor $Co^{II}(OAc)_2$ was purchased from Sigma Aldrich in ≥ 99% purity and used as received. Potassium hydride (KH) as a 30% dispersion in mineral oil was filtered with a glass frit, washed with pentane and Et_2O, dried by vacuum and stored under an argon atmosphere. The syntheses of the metal complexes were conducted in an argon atmosphere.

Physical Methods.

Co^{II} electronic absorbance spectra were collected on a Cary 50 spectrometer and low temperature Co^{III} electronic absorbance spectra were collected on an 8453 Agilent UV-vis spectrophotometer equipped with an Unisoku Unispeks cryostat with a 1.00 cm quartz cuvette. Electronic paramagnetic resonance (EPR) spectra were recorded using a Bruker EMX spectrometer equipped with an ER041XG microwave bridge, an Oxford Instrument liquid-helium quartz cryostat, and a dual mode cavity (ER4116DM). Fourier-transform infrared (FTIR) spectra were collected on a Varian 800 Scimitar series FTIR spectrometer in Nujol. ^{1}H and ^{13}C nuclear magnetic resonance (NMR) spectroscopies were conducted using a Bruker DRX500 spectrometer. Solution magnetic moments were determined by the Evan's method using a Bruker DRX500 spectrometer.[37] Cyclic voltammetric experiments were conducted using a CHI600C electrochemical analyzer. A 2.0 mm glassy carbon electrode was used as the working electrode at scan velocities of 100 mV s^{-1}. A cobaltocenium/cobaltocene couple ($CoCp_2^+/CoCp_2$) (ΔE_p = 0.136 V) was used to monitor the Ag wire reference electrode and all potentials are reference to the Fc^+/Fc couple.

Preparative Methods.

N,N'-(((2–(3–(tert-butyl)ureido)ethyl)azanediyl)bis(ethane-2,1-diyl))bis(4-methylbenzenesulfonamide) (H_41^{tol}). *N,N'*-(((2–aminoethyl)azanediyl)bis(ethane-2,1-diyl))bis(4-methylbenzenesulfonamide) (2.507 g, 4.510 mmol) was dissolved in 120 mL of dichloromethane (CH_2Cl_2), and *tert*-butyl isocyanate (0.507 g, 5.11 mmol) dissolved in 60 mL of CH_2Cl_2 was added dropwise and stirred overnight. Volatiles were removed under reduced pressure to give a light yellow powder that was further dried under vacuum. The product was dissolved in ethyl acetate (EtOAc) and eluted through a silica plug with EtOAc to give 2.50 g (82%) of the desired product as a white solid. FTIR (KBr disc, cm^{-1}): 3406, 3289, 2965, 2925, 2870, 1648, 1598, 1550, 1496, 1452, 1324, 1214, 1158, 1093, 950, 815, 707, 660, 551. ^{1}H NMR (500 MHz, $CDCl_3$, ppm): 1.32 (s, 9H), 2.42 (s, 6H), 2.14 (s, 6H), 2.46 (t, 2H), 2.51 (t, 4H), 2.96 (m, 4H), 3.15 (q, 2H), 4.96 (s, 1H), 5.22 (t, 1H), 5.89 (br s, 2H), 7.31 (d, 4H), 7.79 (d, 4H). ^{13}C NMR (500 MHz, $CDCl_3$, ppm): 158.41, 143.53, 136.86, 129.87, 127.15, 53.39, 50.28, 41.12, 37.59, 29.53, 21.60. HRMS (ES+) Exact mass calcd for $C_{25}H_{39}N_5O_5S_2Na$ [$H_4$1^{tol} + Na]+, 576.2290. Found 576.2270.

tert-butyl (2–(bis(2–(3–(tert-butyl)ureido)ethyl)amino)ethyl)carbamate (6). *tert*-butyl (2–(bis(2–aminoethyl)amino)ethyl)carbamate (1.292 g, 5.234 mmol) was dissolved in 60 mL of CH_2Cl_2 and a 60 mL solution of *tert*-butyl isocyanate (1.036 g, 10.45 mmol) was added dropwise over 30 min. The reaction was allowed to stir overnight under N_2, after which the solvent was removed under vacuum to afford a white powder. This solid was dissolved in 5:100 solution of methanol: CH_2Cl_2 and was eluted through a silica plug with a 5:100 solution of methanol: CH_2Cl_2 to give 1.254 g (54%) of white solid. ^{1}H NMR (500 MHz, $CDCl_3$, ppm): 1.34 (s, 18H), 1.44 (s, 9H), 2.48 (m, 6H), 3.12 (m, 6H), 5.02 (m, 3H), 5.65 (s, 2H). ^{13}C NMR (500 MHz, $CDCl_3$, ppm): 158.71, 156.78, 79.44, 56.16, 55.43, 50.08, 39.10, 38.09, 29.67, 28.49. HRMS (ES+) [$C_{21}H_{44}N_6O_4$ + H]+, 445.3502. Found 445.3511.

1,1'-(((2–aminoethyl)azanediyl)bis(ethane-2,1-diyl))bis(3–(tert-butyl)urea) (7). *tert*-butyl (2–(bis(2–(3–(*tert*-butyl)ureido)ethyl)amino)ethyl)carbamate (6.415 g, 14.43 mmol) was dissolved in 40 mL of CH_2Cl_2, cooled to 0 ºC and 40 mL of trifluoroacetic acid was added dropwise under N_2. The solution was allowed to stir for an additional 2 h and the volatiles were removed under reduced pressure to yield a colorless oil. This oil was stirred with 4 M NaOH until a pH of 11 was achieved. This solution was then extracted with 10x20 mL of CH_2Cl_2 and dried over Na_2SO_4. The solvent was removed by vacuum to afford 3.73 g (75%) of the desired product as a white solid. ^{1}H NMR (500 MHz, $CDCl_3$, ppm): 1.31 (s, 18H), 2.47

(m, 6H), 2.59 (t, 2H), 3.19 (q, 4H), 5.08 (s, 2H), 5.62 (m, 2H). ^{13}C NMR (500 MHz, CDCl3, ppm): 158.70, 56.02, 50.07, 39.63, 38.10, 29.65. HRMS (ES+) [$C_{16}H_{36}N_6O_2$ + Na], 367.2798. Found 367.2808.

N-(2–(bis(2–(3–(tert-butyl)ureido)ethyl)amino)ethyl)-4-methylbenzenesulfonamide ($H_5$2^{tol}). 1,1'-(((2–aminoethyl)azanediyl)bis(ethane-2,1-diyl))bis(3–(*tert*-butyl)urea) (1.210 g, 3.517 mmol) and Et_3N (0.613 g, 6.06 mmol) were dissolved in EtOAc (60 mL) and treated dropwise with 4-toluenesulfonyl chloride(0.674 g, 3.54 mmol) in EtOAc (60 mL) over 1 h. The mixture was allowed to stir overnight under N_2, after which the resultant solution was washed with 2x20 mL of H_2O and 15 mL of brine followed by drying over Na_2SO_4. The colorless solution was filtered and dried under reduced pressure to yield a white solid that was washed with diethyl ether (Et_2O) and vacuumed dried overnight to yield 1.236 g (70.5%) of the desired white solid. ^{1}H NMR (500 MHz, $CDCl_3$, ppm): 1.32 (s, 18H), 2.40 (s, 3H), 2.47 (s, 6H), 2.99 (s, 2H), 3.14 (s, 4H), 5.22 (s, 2H), 5.60 (s, 2H), 6.22 (s, 1H), 7.31 (d, 2H), 7.76 (d, 2H). ^{13}C NMR (500 MHz, $CDCl_3$, ppm): 158.85, 143.31, 137.37, 129.80, 126.93, 55.53, 50.05, 46.30, 41.52, 37.87, 29.60, 21.55. HRMS (ES+) [$C_{23}H_{42}SN_6O_4$ + Na]+, 521.2886. Found 521.2872.

$K_2[Co^{II}(OH)(H1^{tol})]$. Solid KH (0.0289 g, 0.723 mmol) was treated with a 4 mL DMA solution of H_4**1**^{tol} (0.1003 g, 0.1811 mmol) and stirred until bubbling ceased. $Co(OAc)_2$ (0.0322 g, 0.182 mmol) was then added as one portion and the resultant solution stirred for 20 min to produce a dark purple heterogeneous mixture. Water (3.5 μL, 0.19 mmol) was added via syringe that produced an immediate color change to pink. The mixture was stirred for 1.5 h followed by filtration through a medium porous-glass filter and the filtrate was concentrated to 1 mL under vacuum. To the pink solution 25 mL of Et_2O was added that caused the precipitation of a pink solid which was collected on a medium porous-glass filter, washed with copious amounts of Et_2O, and dried under vacuum. The pink solid was dissolved in 2 mL of DMA and 10 mL of Et_2O was allowed to diffuse resulting in pink precipitate that was collected and dried on a glass fritted filter. 0.0586 g (45%) of the desired pink solid was obtained. FTIR (Nujol, cm^{-1}): 3602, 3581, 3214, 3143, 1651, 1600, 1516, 1463, 1376, 1356, 1323, 1220, 1136, 1079, 1045, 1020, 976, 832, 809, 662. 604. UV/vis (DMA, nm (M^{-1} cm^{-1})): λ_{max} (ε) = 470 (103), 493 (120), 528 (129), 610 (81), 637 (75), 690 (54), 820 (30). μ_{eff} (DMSO, 298K): 4.10 μ_B. Anal. Calcd (found) for $C_{25}H_{37}CoK_2N_5O_6S_2$: C, 42.60 (42.58); H, 5.29 (5.47); N, 9.94 (9.95). EPR (X-band, Perpendicular, DMA, 77K): g = 3.9

$K_2[Co^{II}(OH)(H_2\mathbf{2}^{tol})]$. This salt was prepared using a similar procedure described above for $K_2[Co^{II}(OH)(H\mathbf{1}^{tol})]$ with $H_5\mathbf{2}^{tol}$ (0.1974 g, 0.3958 mmol), KH (0.0649 g, 1.62 mmol), $Co(OAc)_2$ (0.0710 g, 0.401 mmol), and H_2O (7 µL, 0.4 mmol). The salt was isolated as a fine pink/purple powder after diffusion of Et_2O into the DMA solution. The pink/purple solid was collected on a medium porous-glass filter, and washed with 20 mL MeCN, 20 mL of THF, and 20 mL of Et_2O and dried by vacuum to give 0.1422 g (55 %) of the desired product. FTIR (Nujol mull, cm^{-1}) 3625, 3218, 3142, 1646, 1593, 1514, 1464, 1400, 1378, 1357, 1330, 1268, 1228, 1221, 1132, 1125, 1105, 1074, 1048, 1019, 977, 891, 839, 817, 795, 720, 660. UV/Vis (DMA, nm (M^{-1} cm^{-1})): λ_{max} (ε) = 472 (80), 488 (90), 528 (120), 767 (30). μ_{eff} (DMSO, 298 K, Evan's Method): 4.26 μ_B. Anal. Calcd (found) for $C_{23}H_{40}CoK_2N_6O_5S$.DMA: C, 44.01 (44.28); H, 6.70 (6.74); N, 13.31 (13.17). EPR (X-band, DMA, 77K): g = 3.8.

$K_2[Co^{II}(OH)TST]$. H_3TST (0.3254 g, 0.5345 mmol) was dissolved in 8 mL of DMA and added to 3 equiv of neat KH (0.0653 g, 1.63 mmol) and stirred until bubbling ceased. $Co(OAc)_2$ (0.0951 g, 0.537 mmol) was added and stirred for 1 h to produce a dark blue mixture. The blue mixture was filtered through a glass fritted filter and H_2O (12 µL, 0.67 mmol) was added to the filtrate to give a pink solution that was stirred for 15 min. KH (0.0222 g, 0.555 mmol) was added to the solution and it was stirred until bubbling ceased. The solution was filtered through a medium porous-glass filter and the filtrate was split into two vials and 10 mL of Et_2O was allowed to diffuse which resulted in dark purple crystals that were washed with 20 mL of CH_2Cl_2 and 30 mL of Et_2O and dried by vacuum to give 0.2407 g (59%) of the desired purple solid. FTIR (Nujol mull, cm^{-1}) 3569, 1645, 1597, 1493, 1464, 1376, 1246, 1142, 1112, 1081, 1044, 1017, 974, 932, 872, 815, 735, 710, 663, 599, 556. UV/Vis (DMA, nm (M^{-1} cm^{-1})): λ_{max} (ε) = 522 (170), 660 (65), 890 (35). μ_{eff} (DMSO, 298K, Evan's Method): 4.11 μ_B. Anal. Calcd (found) for $C_{27}H_{36}CoK_2N_4O_7S_3.0.5CH_2Cl_2$: C, 41.06 (41.16); H, 4.41 (4.52); N, 6.97 (6.79). EPR (X-band, 77K, perpendicular): g = 3.7.

Oxidation of Co^{II}–OH Complexes. A stock solution of the Co^{II}–OH complex was prepared in DMA (20 mL) at room temperature. A 3 mL aliquot of the solution of Co^{II}–OH was transferred to a 1 cm quartz cuvette and was sealed with a rubber septum before being transferred to a precooled 8453 Agilent UV-vis spectrophotometer equipped with an Unisoku Unispeks cryostat and allowed to equilibrate to the desired temperature for at least 15 min. A stock solution of $[FeCp_2]BF_4$ was prepared in DMA. To the Co^{II}–OH solution, 1 equiv of $[FeCp_2]BF_4$ was added via gas-tight syringe. The high energy band corresponding to the Co^{III} species between 400 – 500 nm was monitored to determine the half-lives of the Co^{III}–OH compounds (Figure 2.9) and treated as 2nd order reaction: half-lives were determined from $1/k[Co^{III}$ complex].

X-Ray Crystallographic Methods.

A Bruker SMART APEX II diffractometer was used for molecular structure determination. The APEX2[38] program package was used to determine the unit-cell parameters and for data collection. The raw data was processed using SAINT[39] and SADABS[40] to yield the reflection data file. Subsequent calculations were carried out using the SHELXTL[41] program. The structures were solved by direct methods and refined to convergence. Crystallographic data of the structure determination are given in Table 2.6. Selected bond lengths and angles are given in Table 2.1 and the molecular structure of each anion is shown in Figure 2.3. The structure of $K_2[Co^{II}TST(OH)]$ contained three anions within the asymmetric unit that were chemically identical. Two of the anions have disorder within the $[TST]^{3-}$ ligand: the anion containing Co2 has two tolyl groups that are disordered and the anion containing Co3 has one disordered tolyl group. For the anion containing Co2 the disorder was modeled using multiple components using partial site-occupancy factors (50:50 for both rings); for the anion with Co3 the disorder was modeled with 50:50 site occupancy. The anion containing Co3 also had partial disorder within the tren backbone that was modeled as 50:50 disorder. The anion of $[Co^{II}TST(OH)]^{2-}$ that was not disordered is shown in Figure 2.3 and its metrical parameters were used in Table 2.1.

Table 2.6. Crystallographic Data for $K_2[Co^{II}TST(OH)]$ and $K_2[Co^{II}H_2\mathbf{2}^{tol}(OH)]$•2DMA

Salt	$(K_2[Co^{II}TST(OH)])_3$	$K_2[Co^{II}H_2\mathbf{2}^{tol}(OH)]$•2DMA
Empirical Formula	$C_{81}H_{102}Co_3K_6N_{12}O_{21}S_9$	$C_{31}H_{58}CoK_2N_8O_7S$
fw	2277.65	824.04
T (K)	88(2)	88(2)
space group	$P2_1/c$	$P1$
a (Å)	19.4569(14)	11.9841(7)
b (Å)	32.796(2)	12.9122(7)
c (Å)	18.3848(13)	14.8689(8)
α (deg)	90	68.6652(7)
β (deg)	111.2036(9)	87.4545(8)
γ (deg)	90	69.8767(7)
Z	4	2
V (Å^3)	10943.1(13)	2003.73(19)
δ_{calcd} (Mg/m^3)	1.384	1.366
R1	0.0804	0.0378
wR2	0.2098	0.0942
GOF	1.058	1.025

wR2 = $[\Sigma[w(F_o^2 - F_c^2)^2] / \Sigma[w(F_o^2)^2]]^{1/2}$; R1 = $\Sigma||F_o| - |F_c|| / \Sigma|F_o|$; Goof = S = $[\Sigma[w(F_o^2 - F_c^2)^2] / (n-p)]^{1/2}$ where n is the number of reflections and p is the total number of parameters refined.

References

(1) Shook, R. L.; Borovik, A. S. Role of the Secondary Coordination Sphere in Metal-Mediated Dioxygen Activation. *Inorg. Chem.* **2010**, *49* (8), 3646–3660.

(2) Shook, R. L.; Borovik, A. S. The Effects of Hydrogen Bonds on Metal-Mediated O2 Activation and Related Processes. *Chem. Commun.* **2008**, No. 46, 6095.

(3) Borovik, A. S. Bioinspired Hydrogen Bond Motifs in Ligand Design: The Role of Noncovalent Interactions in Metal Ion Mediated Activation of Dioxygen. *Acc. Chem. Res.* **2005**, *38* (1), 54–61.

(4) Cook, S. A.; Borovik, A. S. Molecular Designs for Controlling the Local Environments around Metal Ions. *Acc. Chem. Res.* **2015**, *48* (8), 2407–2414.

(5) Cook, S. A.; Hill, E. A.; Borovik, A. S. Lessons from Nature: A Bio-Inspired Approach to Molecular Design. *Biochemistry* **2015**, *54* (27), 4167–4180.

(6) Natale, D.; Mareque-Rivas, J. C. The Combination of Transition Metal Ions and Hydrogen-Bonding Interactions. *Chem. Commun.* **2008**, No. 4, 425–437.

(7) Lucas, R. L.; Zart, M. K.; Murkerjee, J.; Sorrell, T. N.; Powell, D. R.; Borovik, A. S. A Modular Approach toward Regulating the Secondary Coordination Sphere of Metal Ions: Differential Dioxygen Activation Assisted by Intramolecular Hydrogen Bonds. *J. Am. Chem. Soc.* **2006**, *128* (48), 15476–15489.

(8) Matson, E. M.; Bertke, J. A.; Fout, A. R. Isolation of Iron(II) Aqua and Hydroxyl Complexes Featuring a Tripodal H-Bond Donor and Acceptor Ligand. *Inorg. Chem.* **2014**, *53* (9), 4450–4458.

(9) Park, Y. J.; Matson, E. M.; Nilges, M. J.; Fout, A. R. Exploring Mn–O Bonding in the Context of an Electronically Flexible Secondary Coordination Sphere: Synthesis of a Mn(III)–oxo. *Chem. Commun.* **2015**, *51* (25), 5310–5313.

(10) Wada, A.; Harata, M.; Hasegawa, K.; Jitsukawa, K.; Masuda, H.; Mukai, M.; Kitagawa, T.; Einaga, H. Structural and Spectroscopic Characterization of a Mononuclear Hydroperoxo-Copper(II) Complex with Tripodal Pyridylamine Ligands. *Angew.*

Chemie Int. Ed. **1998**, *37* (6), 798–799.

(11) Mareque-Rivas, J. C.; Salvagni, E.; Parsons, S. Investigating the Effect of Hydrogen Bonding Environments in Amide Cleavage Reactions at zinc(II) Complexes with Intramolecular Amide Oxygen Co-Ordination. *Dalt. Trans.* **2004**, No. 24, 4185–4192.

(12) Berreau, L. M.; Makowska-Grzyska, M. M.; Arif, A. M.; Arif Atta, M. Modeling the Active Site Chemistry of Liver Alcohol Dehydrogenase: Mononuclear Zinc Methanol and N,N -Dimethylformamide Complexes of a Nitrogen/Sulfur Ligand Possessing an Internal Hydrogen Bond Donor. *Inorg. Chem.* **2001**, *40* (10), 2212–2213.

(13) Kendall, A. J.; Zakharov, L. N.; Gilbertson, J. D. Synthesis and Stabilization of a Monomeric Iron(II) Hydroxo Complex via Intramolecular Hydrogen Bonding in the Secondary Coordination Sphere. *Inorg. Chem.* **2010**, *49* (19), 8656–8658.

(14) Moore, C. M.; Quist, D. A.; Kampf, J. W.; Szymczak, N. K. A 3-Fold-Symmetric Ligand Based on 2-Hydroxypyridine: Regulation of Ligand Binding by Hydrogen Bonding. *Inorg. Chem.* **2014**, *53* (7), 3278–3280.

(15) Blacquiere, J. M.; Pegis, M. L.; Raugei, S.; Kaminsky, W.; Forget, A.; Cook, S. A.; Taguchi, T.; Mayer, J. M. Synthesis and Reactivity of Tripodal Complexes Containing Pendant Bases. *Inorg. Chem.* **2014**, *53* (17), 9242–9253.

(16) Matson, E. M.; Park, Y. J.; Fout, A. R. Facile Nitrite Reduction in a Non-Heme Iron System: Formation of an Iron(III)-Oxo. *J. Am. Chem. Soc.* **2014**, *136* (50), 17398–17401.

(17) Park, Y. J.; Matson, E. M.; Nilges, M. J.; Fout, A. R. Exploring Mn-O Bonding in the Context of an Electronically Flexible Secondary Coordination Sphere: Synthesis of a Mn(III)-Oxo. *Chem. Commun. (Camb).* **2015**, *51* (25), 5310–5313.

(18) Lacy, D. C.; Park, Y. J.; Ziller, J. W.; Yano, J.; Borovik, A. S. Assembly and Properties of Heterobimetallic Co(II/III)/Ca(II) Complexes with Aquo and Hydroxo Ligands. *J. Am. Chem. Soc.* **2012**, *134* (42), 17526–17535.

(19) Taguchi, T.; Gupta, R.; Lassalle-Kaiser, B.; Boyce, D. W.; Yachandra, V. K.; Tolman, W. B.; Yano, J.; Hendrich, M. P.; Borovik, A. S. Preparation and Properties of a Monomeric High-Spin Mn(V)-Oxo Complex. *J. Am. Chem. Soc.* **2012**, *134* (4), 1996–1999.

(20) Gupta, R.; MacBeth, C. E.; Young, V. G.; Borovik, A. S. Isolation of Monomeric Mn(III/II) −OH and Mn(III)−O Complexes from Water: Evaluation of O−H Bond Dissociation Energies. *J. Am. Chem. Soc.* **2002**, *124* (7), 1136–1137.

(21) MacBeth, C. E.; Gupta, R.; Mitchell-Koch, K. R.; Young, V. G.; Lushington, G. H.; Thompson, W. H.; Hendrich, M. P.; Borovik, A. S. Utilization of Hydrogen Bonds To Stabilize M−O(H) Units: Synthesis and Properties of Monomeric Iron and Manganese Complexes with Terminal Oxo and Hydroxo Ligands. *J. Am. Chem. Soc.* **2004**, *126* (8), 2556–2567.

(22) Hill, E. A.; Weitz, A. C.; Onderko, E.; Romero-Rivera, A.; Guo, Y.; Swart, M.; Bominaar, E. L.; Green, M. T.; Hendrich, M. P.; Lacy, D. C.; et al. Reactivity of an Fe(IV)-Oxo Complex with Protons and Oxidants. *J. Am. Chem. Soc.* **2016**, *138* (40), 13143–13146.

(23) Bordwell, F. G. Equilibrium Acidities in Dimethyl Sulfoxide Solution. *Acc. Chem. Res.* **1988**, *21* (12), 456–463.

(24) Lau, N.; Ziller, J. W.; Borovik, A. S. Sulfonamido Tripods: Tuning Redox Potentials via Ligand Modifications. *Polyhedron* **2015**, *85*, 777–782.

(25) Gupta, R.; MacBeth, C. E.; Young, V. G. J.; Borovik, A. S. Isolation of Monomeric Mn(III/II)-OH and Mn(III)-O Complexes from Water: Evaluation of O-H Bond Dissociation Energies. *J. Am. Chem. Soc.* **2002**, *124* (7), 1136–1137.

(26) Chen, D.; Motekaitis, R. J.; Murase, I.; Martell, A. E. The Synthesis of Binucleating Polyaza Macrocyclic and Macrobicyclic Ligands and the Dioxygen Affinities of Their Cobalt Complexes. *Tetrahedron* **1995**, *51* (1), 77–88.

(27) Hammes, B. S.; Young, Jr., V. G.; Borovik, A. S. Hydrogen-Bonding Cavities about Metal Ions: A Redox Pair of Coordinatively Unsaturated Paramagnetic Co-OH Complexes. *Angew. Chemie Int. Ed.* **1999**, *38* (5), 666–669.

(28) Shirin, Z.; S. Borovik, A.; G. Young Jr., V. Synthesis and Structure of a Mn(III)-OH Complex Generated from Dioxygen. *Chem. Commun.* **1997**, No. 20, 1967.

(29) Ray, M.; Golombek, A. P.; Hendrich, M. P.; Young, V. G.; Borovik, A. S. Synthesis and Structure of a Trigonal Monopyramidal Fe(II) Complex and Its Paramagnetic Carbon Monoxide Derivative. *J. Am. Chem. Soc.* **1996**, *118* (25), 6084–6085.

(30) Ray, M.; Hammes, B. S.; Yap, G. P. A.; Rheingold, A. L.; Borovik, A. S. Structure and Physical Properties of Trigonal Monopyramidal Iron(II), Cobalt(II), Nickel(II), and Zinc(II) Complexes. *Inorg. Chem.* **1998**, *37* (7), 1527–1532.

(31) Park, Y. J.; Ziller, J. W.; Borovik, A. S. The Effects of Redox-Inactive Metal Ions on the Activation of Dioxygen: Isolation and Characterization of a Heterobimetallic Complex Containing a Mn(III)–(μ-OH)–CaII Core. *J. Am. Chem. Soc.* **2011**, *133* (24), 9258–9261.

(32) Shook, R. L.; Gunderson, W. A.; Greaves, J.; Ziller, J. W.; Hendrich, M. P.; Borovik, A. S. A Monomeric Mn(III)−Peroxo Complex Derived Directly from Dioxygen. *J. Am. Chem. Soc.* **2008**, *130* (28), 8888–8889.

(33) MacBeth, C. E.; Hammes, B. S.; Young, V. G.; Borovik, A. S. Hydrogen-Bonding Cavities about Metal Ions: Synthesis, Structure, and Physical Properties for a Series of Monomeric M-OH Complexes Derived from Water. *Inorg. Chem.* **2001**, *40* (18), 4733–4741.

(34) Mukherjee, J.; Lucas, R. L.; Zart, M. K.; Powell, D. R.; Day, V. W.; Borovik, A. S. Synthesis, Structure, and Physical Properties for a Series of Monomeric Iron(III) Hydroxo Complexes with Varying Hydrogen-Bond Networks. *Inorg. Chem.* **2008**, *47* (13), 5780–5786.

(35) Gellman, S. H.; Dado, G. P.; Liang, C.; Adam, B. R. Conformation-Directing Effects of a Single Intramolecular Amide-Amide Hydrogen Bond : Variable-Temperature NMR and IR Studies on a Homologous Diamide Series. *J. Am. Chem. Soc.* **1991**, *113* (4), 1164–1173.

(36) DiVittorio, K. M.; Hofmann, F. T.; Johnson, J. R.; Abu-Esba, L.; Smith, B. D. Facilitated Phospholipid Translocation in Vesicles and Nucleated Cells Using Synthetic Small Molecule Scramblases. *Bioorg. Med. Chem.* **2009**, *17* (1), 141–148.

(37) Evans, D. F. The Determination of the Paramagnetic Susceptibility of Substances in Solution by Nuclear Magnetic Resonance. *J. Chem. Soc.* **1959**, 2003–2005.

(38) Bruker AXS, I. APEX2 Version 2014.11-0. Madison, WI 2014.

(39) Bruker AXS, I. SAINT Version 8.34a. Madison, WI 2013.

(40) Sheldrick, G. M. SADABS. Bruker AXS, Inc: Madison 2014.

(41) Sheldrick, G. M. SHELXTL. Bruker AXS, Inc: Madison 2014.

CHAPTER 3

Mn^{III}–Oxido and Mn^{III}–Hydroxido Complexes with Urea-based Hybrid Ligands

Introduction

The previous chapter reported the synthesis of new hybrid sulfonamido and urea based ligands and their properties with Co^{II} ions. The secondary coordination sphere was systematically varied by changing the number of H-bond donor and acceptor groups. However, this study showed that changing from a sulfonamido to a urea causes a measurable change in the primary coordination sphere. This makes it difficult to distinguish whether changes in properties of metal complexes arise from changes in the H-bonding network or the primary coordination sphere. Therefore, studying changes in the secondary coordination sphere require new ligands, which keep the primary coordination sphere constant, while allowing for systematic changes in the secondary coordination sphere.

It is not well understood how varying the strength of H-bonds in the secondary coordination sphere effects the function and properties of metal ions. To this end, a new series of hybrid ligands were developed to modulate only the secondary coordination sphere. This series of hybrid ligands was developed based on a tripodal urea ligand $[H_3buea]^{3-}$ previously synthesized by our group.[1] Previous members of our group have reported the synthesis and characterization of Mn^{III}–O and Mn^{III}–OH complexes using the $[H_3buea]^{3-}$ ligand (Figure 3.1).[2] This ligand is capable of providing up to three intramolecular H-bonds to an axial ligand. These H-bonds have been shown to stabilize a reactive oxido ligand in $[Mn^{III}H_3buea(O)]^{2-}$.[3] Previous studies with this complex have shown that it is capable of doing C–H bond activation with 9,10-dihydroanthracene (DHA) to produce anthracene.[4] Understanding how to activate C–H bonds is of interest to the chemical community because it provides the opportunity to synthesize complex organic molecules in a more efficient manner. To this end, new Mn^{III}–O complexes with hybrid ligands based upon $[H_3buea]^{3-}$, were targeted to develop an understanding of the relationship between H-bonds to a Mn^{III}–O and C–H bond reactivity.

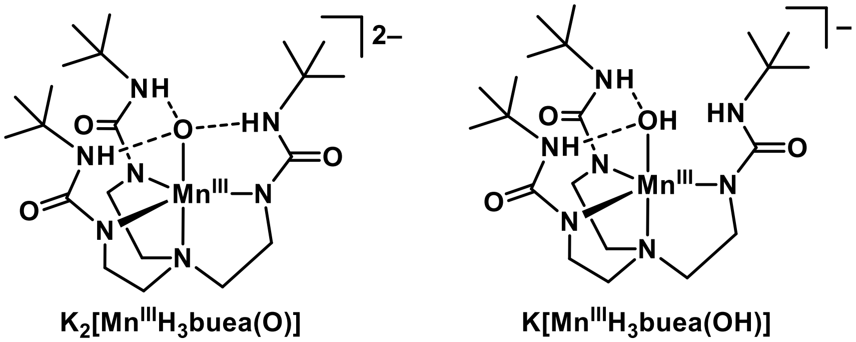

Figure 3.1. Mn^{III}–oxido and Mn^{III}–hydroxido complexes previously reported by the Borovik group with the $[H_3buea]^{3-}$ ligand.[3]

This chapter will describe the synthesis and characterization of a new series of hybrid tripodal urea ligands where two arms contain *tert*-butyl groups analogous to $[H_3buea]^{3-}$ and the third arm contains a substituted phenyl group in which a variety of substituents were placed primarily in the *para*-position. In *para*-substituted phenols it has been shown that the pK_a can be systematically modulated by attaching electron withdrawing or electron donating groups.[5] Systematically modulating the pK_a of the urea NH groups was targeted because pK_a is related to the strength of the H-bond that can form between the urea NH and a H-bond acceptor.[6,7] The strongest H-bond arises when the pK_a of the two groups involved in the H-bond are closely matched, such that ΔpK_a approaches 0. The goal of this project was to modulate the pK_a value for a *single urea NH* within the H-bonding cavity to determined its effect on the function of a Mn^{III}–oxido complex toward C–H bond cleavage. The synthesis and characterization of Mn^{III}–oxido and Mn^{III}–hydroxido complexes with these new hybrid ligands will be presented, along with preliminary reactivity studies with external substrates.

Results and Discussion

Ligand Design and Synthesis. Scheme 3.1 outlines the synthesis of the hybrid ligand precursors H_6**3**^{R} (R = H, F, F_5). The synthesis of the hybrid ligands began with ethylene diamine being treated with di-*tert*-butyl dicarbonate to afford the monoboc protected species N-*tert*-butoxycarbonyl–1,2–diaminoethane.[8] *Tert*-butyl isocyanate was added to

Scheme 3.1. Preparative Route to H_6**3**^{R} (R = H = R_1 is H_6**3**^{Ph}; R = F, R_1 = H is H_6**3**^{F}; R = F = R_1 is H_6**3**^{5F})

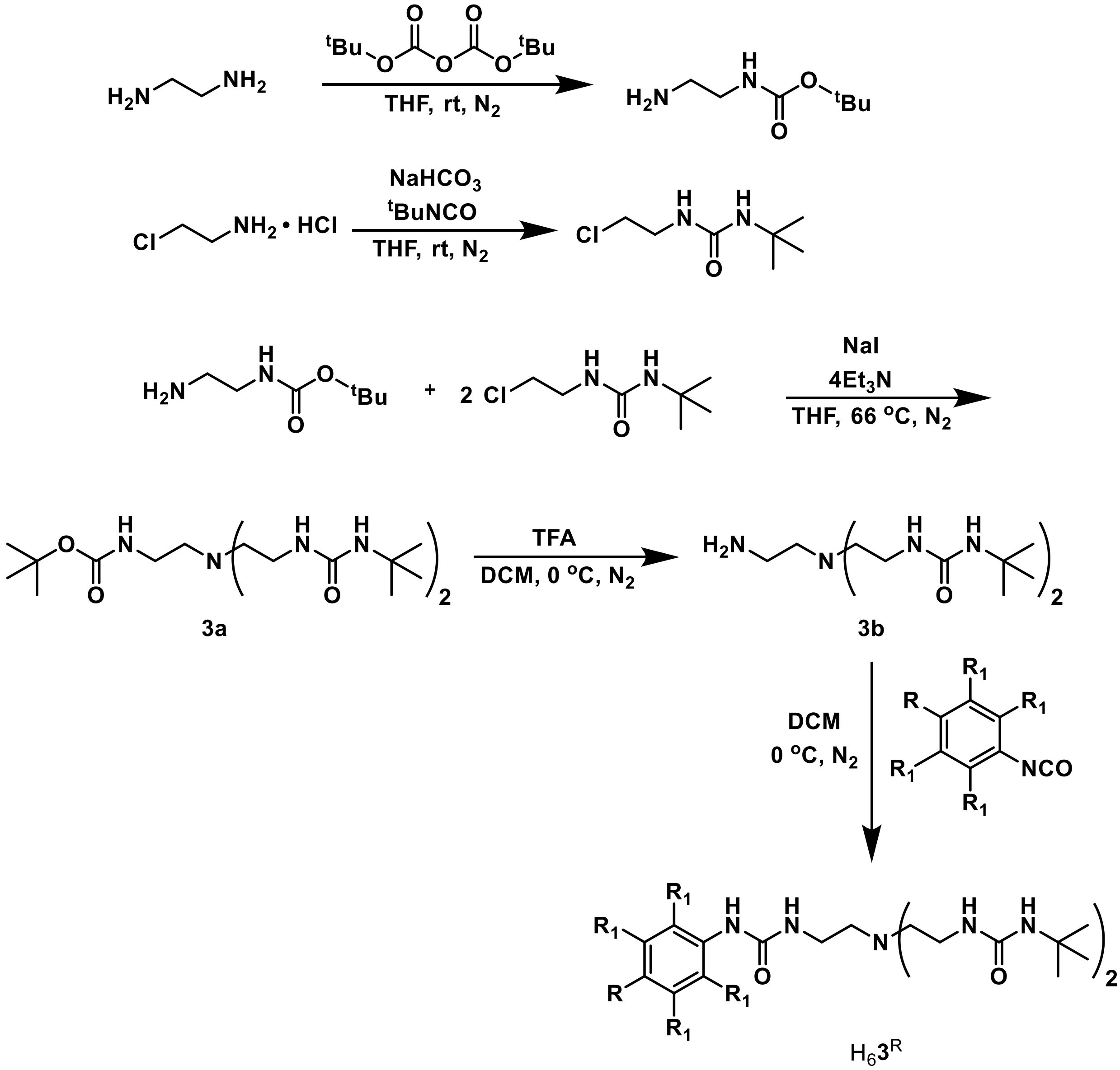

2–chloroethylamine afford 1-*tert*-butyl-3–(2–chloroethyl)urea,[9] which was treated with N-*tert*-butoxycarbonyl–1,2–diaminoethane to afford the monoboc protected diurea tripod (*N*'-*tert*-butyoxycarbonyl)-*N*-ethyl]-bis[(*N*'-*tert*-butylureayl)-*N*-ethyl]amine (**3a**).[10] The monoboc protected diurea tripod **3a** was reacted with trifluoroacetic acid (TFA) to give the primary amine (**3b**)[11] and then the desired isocyanate was added to afford the ligand precursor $H_6\mathbf{3}^R$.

Metal Complex Synthesis. Three Mn^{III} complexes were synthesized by deprotonating the appropriate ligand with 4 equivalents (equiv) of KH in dimethylacetamide (DMA), under an argon atmosphere and then adding solid $Mn^{II}(OAc)_2$ to produce a colorless heterogeneous mixture. The mixture was treated with 0.5 equiv of dry O_2, resulting in an immediate color change to dark purple (for complexes with $[H_3\mathbf{3}^{Ph}]^{3-}$, $[H_3\mathbf{3}^F]^{3-}$, $[H_3buea]^{3-}$) or dark green ($[H_2\mathbf{3}^{5F}]^{4-}$, Scheme 3.2). The mixture was filtered to remove KOAc and was purified by vapor diffusion of Et_2O into the DMA solution of the salt. Since the spectroscopic characterization of $[Mn^{III}H_3buea(O)]^{2-}$ and $[Mn^{III}H_3buea(OH)]^{-}$ have been previously reported, the new Mn metal complexes with different hybrid ligands were compared to those reference complexes.[12]

Scheme 3.2. Preparative Routes to Mn^{III}–O and Mn^{III}–OH Complexes

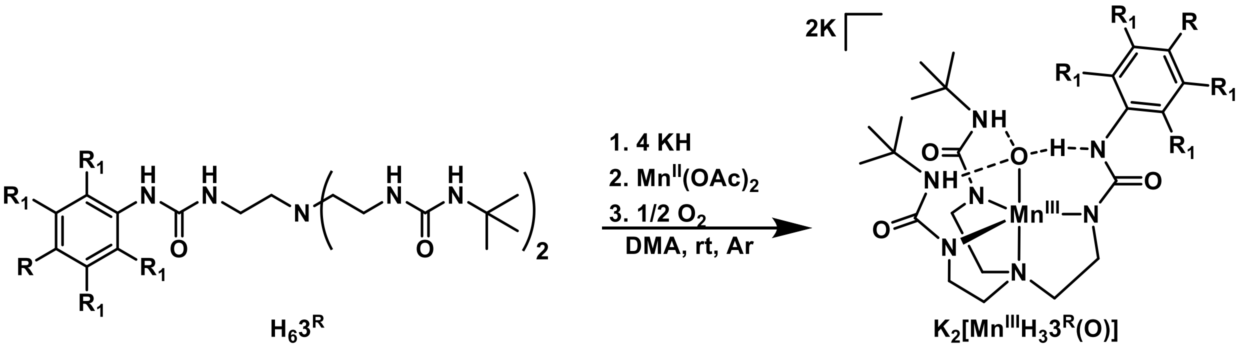

The ligands $[H_2\mathbf{3}^{Ph}]^{4-}$ and $[H_2\mathbf{3}^{F}]^{4-}$ react with Mn^{II} and O_2 to produce complexes with similar spectroscopic properties to $[Mn^{III}H_3buea(O)]^{2-}$, suggesting that they are Mn^{III}–O complexes. In contrast, the more electron withdrawing ligand $[H_2\mathbf{3}^{5F}]^{4-}$ reacts with Mn^{II} and O_2 to produce a complex with different spectroscopic features to $[Mn^{III}H_3buea(O)]^{2-}$ and $[Mn^{III}H_3buea(OH)]^{-}$. However, the Mn^{III} complex with $[H_2\mathbf{3}^{5F}]^{4-}$ has similar structural and spectroscopic properties to Mn^{III} complex our group previously characterized with a tripodal ligand with two urea groups and one carboxyamidopyridyl unit ($[H_2bupa]^{3-}$).[13,14] In the complex $[Mn^{III}H_2bupa(O)(H)]^{-}$, observations suggested that this complex was a hybrid species between an Mn–oxido and Mn–hydroxido (Figure 3.2).[13] However, structural data for the Mn^{III} complex with $[H_2\mathbf{3}^{5F}]^{4-}$ revealed that the hydrogen atom is located on the oxygen, suggesting the complex is a Mn^{III}–OH complex with a deprotonated urea. The following sections will describe the characterization of the Mn^{III} complexes with the $[H_2\mathbf{3}^{Ph}]^{4-}$, $[H_2\mathbf{3}^{F}]^{4-}$, and $[H_2\mathbf{3}^{5F}]^{4-}$ ligands, and make comparisons to previously reported complexes.

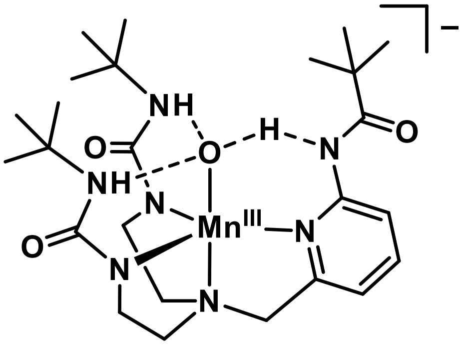

Figure 3.2. Possible structure of the complex $[Mn^{III}H_2bupa(O)(H)]^{-}$.[13]

Electronic Absorbance Properties. The Mn^{III}–O, Mn^{III}–OH, Mn^{IV}=O, Mn^{IV}–OH, and Mn^{V}=O complexes with $[H_3buea]^{3-}$ have unique electronic absorbance spectra that can be used as a powerful tool in determining the protonation state of the oxido ligand.[15–18] In particular, $[Mn^{III}H_3buea(O)]^{2-}$ and $[Mn^{III}H_3buea(OH)]^{-}$ have diagnostic spectra (Figure 3.3).[15] We reasoned that the Mn^{III}–O(H) complexes in this complex would have similar spectra to these reference complexes and could be used to assess the protonation states in the complexes with the new hybrid ligands.

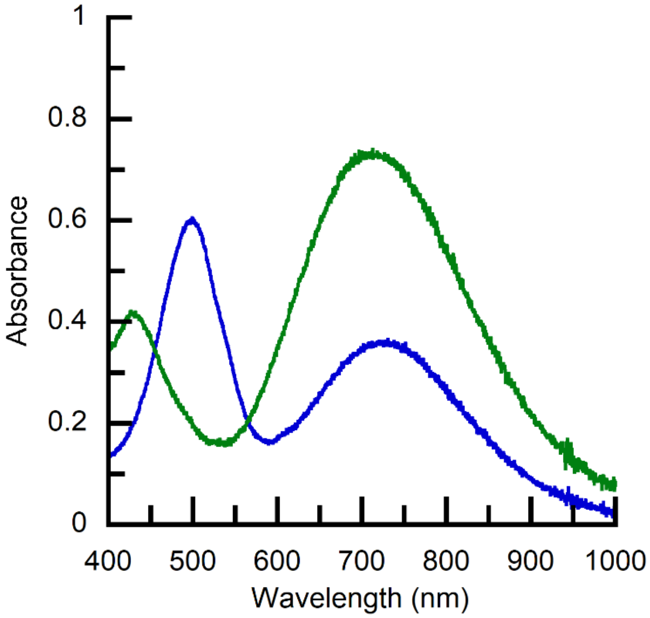

Figure 3.3. Electronic absorbance spectra of $[Mn^{III}H_3buea(O)]^{2-}$ (blue line, 1.4 mM) and $[Mn^{III}H_3buea(OH)]^{-}$ (green line, 1.4 mM) recorded in DMSO.

The electronic absorbance spectra for the new Mn^{III}–O complexes ($[Mn^{III}H_3\mathbf{3}^{Ph}(O)]^{2-}$ and $[Mn^{III}H_3\mathbf{3}^{F}(O)]^{2-}$) are characterized by bands at λ_{max}/nm ~ 500 and 710 with extinction coefficients less than 500 M^{-1} cm^{-1} (Figure 3.4 and Table 3.1).[15] This is consistent with the properties of the previously characterized $[Mn^{III}H_3buea(O)]^{2-}$.[15] In the Mn^{III}–O complexes, there is a progressive shift of the low-energy band to higher energy as more electron withdrawing groups are attached to the phenyl ring. No effect is observed on the high-energy band of the Mn^{III}–O complexes, as it appears at the same energy for all three of the complexes. The electronic absorbance spectrum of $[Mn^{III}H_2\mathbf{3}^{5F}(OH)]^{2-}$ contains an absorbance band at λ_{max}/nm = 675 with an extinction coefficient less than 300 M^{-1} cm^{-1} (Figure 3.4 and Table

3.1). These spectroscopic features are very different than $[Mn^{III}H_3buea(OH)]^-$, which contains absorbance bands at λ_{max}/nm = 427 and 724 with extinction coefficients less than 550 M^{-1} cm^{-1}.[15] A more appropriate comparison of the electronic absorbance spectrum of $[Mn^{III}H_2\mathbf{3}^{5F}(OH)]^{2-}$ to $[Mn^{III}H_2bupa(O)(H)]^-$, shows a nearly identical spectrum with an absorbance band at λ_{max}/nm = 675 with an extinction coefficient of 360 M^{-1} cm^{-1}.[13] These complexes are more comparable because the secondary coordination spheres around the metal ion in $[Mn^{III}H_2\mathbf{3}^{5F}(OH)]^{2-}$ and $[Mn^{III}H_2bupa(O)(H)]^-$ are more similar than $[Mn^{III}H_3buea(OH)]^-$. In $[Mn^{III}H_2\mathbf{3}^{5F}(OH)]^{2-}$ and $[Mn^{III}H_2bupa(O)(H)]^-$ the molecular structure suggests there are three intramolecular H-bonds, whereas $[Mn^{III}H_3buea(OH)]^-$ contains two intramolecular H-bonds (Figure 3.2).

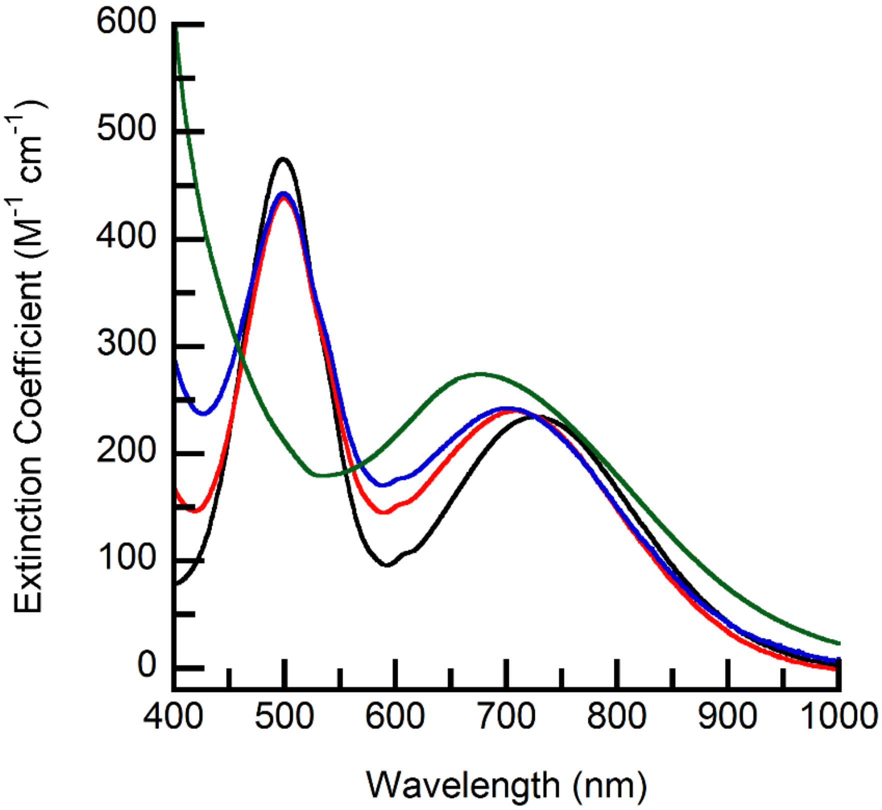

Figure 3.4. Electronic absorbance spectra for $[Mn^{III}H_3buea(O)]^{2-}$ (black line), $[Mn^{III}H_3\mathbf{3}^{Ph}(O)]^{2-}$ (red line), $[Mn^{III}H_3\mathbf{3}^{F}(O)]^{2-}$ (blue line), and $[Mn^{III}H_2\mathbf{3}^{5F}(OH)]^{2-}$ (green line) recorded in DMSO at room temperature

Table 3.1. Electronic Absorbance Properties of the Mn^{III}–O and Mn^{III}–OH Complexes

	λ_{max} (nm), (ε, M cm^{-1})
$[Mn^{III}H_3buea(O)]^{2-}$	725, (235); 498, (475)
$[Mn^{III}H_3\mathbf{3}^{Ph}(O)]^{2-}$	710, (240); 498, (438)
$[Mn^{III}H_3\mathbf{3}^{F}(O)]^{2-}$	706, (242); 498, (443)
$[Mn^{III}H_2\mathbf{3}^{5F}(OH)]^{2-}$	677, (274)

Solid-State Structural Properties. The molecular structure of $[Mn^{III}H_2\mathbf{3}^{5F}(OH)]^{2-}$ was examined by X-ray diffraction (XRD) (Figure 3.5 and Table 3.2). A single crystal of $(NMe_4)_2[Mn^{III}H_2\mathbf{3}^{5F}(OH)]$ was obtained by reaction of $K_2[Mn^{III}H_2\mathbf{3}^{5F}(OH)]$ with 2 equiv of NMe_4OAc in acetonitrile and vapor diffusion of Et_2O into the acetonitrile solution. Single crystals of $K_2[Mn^{III}H_3\mathbf{3}^{Ph}(O)]$ and $K_2[Mn^{III}H_3\mathbf{3}^{F}(O)]$ were attempted with a variety of solvent combinations (dimethylformamide (DMF), DMA, dimethyl sulfoxide (DMSO), Et_2O, tetrahydrofuran (THF)) and counterions (NMe_4^+, NBu_4^+, $K\subset(2.2.2\text{-cryptand})^+$), however, suitable crystals for XRD were not obtained under any conditions. The structure of $[Mn^{III}H_3buea(O)]^{2-}$ and $[Mn^{III}H_2bupa(O)(H)]$ (Figure 3.6 and Table 3.3) has been reported previously and is discussed here in comparison to $[Mn^{III}H_2\mathbf{3}^{5F}(OH)]^{2-}$.

The molecular structure of $[Mn^{III}H_2\mathbf{3}^{5F}(OH)]^{2-}$ revealed a trigonal bipyramidal coordination geometry around the Mn^{III} center with the trigonal plane defined by the three deprotonated nitrogen donors from the $[H_2\mathbf{3}^{5F}]^{4-}$ ligand. The hydrogen atom on O1 was located from the difference-Fourier map, which led to the assignment of this complex as a Mn^{III}–OH species. Additionally, the difference-Fourier map showed no residual electron density within bonding distance to N7, suggesting N7 is deprotonated. There are statistically significant differences in the Mn1–N bond lengths in the trigonal plane between the different nitrogen donors. The Mn1–N4 bond distance of 2.017(5) Å is shorter than Mn1–N2 and Mn1–N3 bond distances (2.057(5) and 2.070(5) Å). This likely arises from the strong H-bond

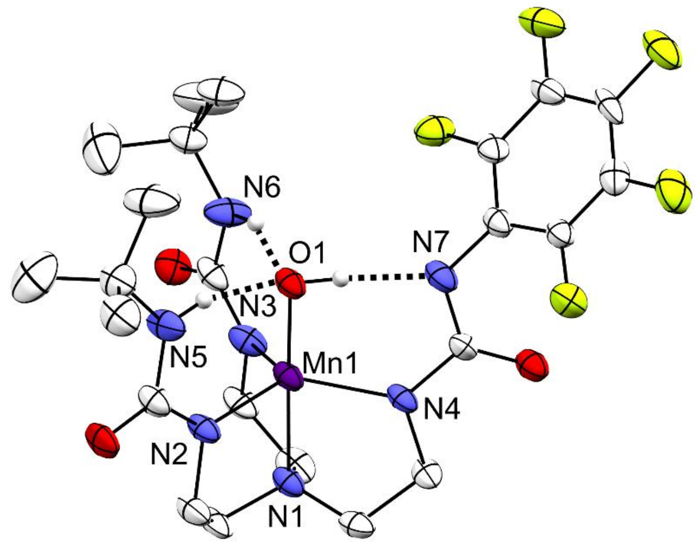

Figure 3.5. Thermal ellipsoid plot of $[Mn^{III}H_2\mathbf{3}^{5F}(OH)]^{2-}$. Thermal ellipsoids are drawn at the 50% probability level. Hydrogen atoms not involved in H-bonding are omitted for clarity.

Table 3.2. Selected Bond Distances (Å) and Angles (°) for $[Mn^{III}H_2\mathbf{3}^{5F}(OH)]^{2-}$

Mn1–O1	1.818(4)
Mn1–N1	2.059(5)
Mn1–N2	2.055(5)
Mn1–N3	2.070(5)
Mn1–N4	2.018(5)
d(N5···O1)	2.764(6)
d(N6···O1)	2.796(7)
d(O1···N7)	2.611(6)
O1–Mn1–N1	178.6(2)
O1–Mn1–N2	98.28(18)
O1–Mn1–N3	99.4(2)
O1–Mn1–N4	96.18(18)
N4–Mn1–N1	82.45(19)
N4–Mn1–N2	124.3(2)
N4–Mn1–N3	117.6(2)
N2–Mn1–N1	82.26(19)
N2–Mn1–N3	112.5(2)
N1–Mn1–N3	81.6(2)

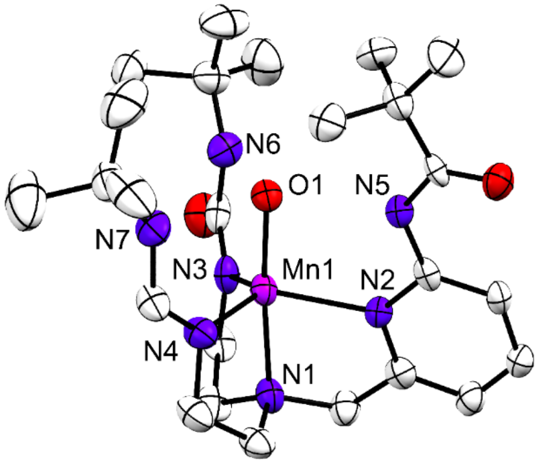

Figure 3.6. Thermal ellipsoid plot of $[Mn^{III}H_2bupa(O)(H)]^-$. Thermal ellipsoids are drawn at the 50% probability level. Hydrogen atoms involved in H-bonding were not located in the structure. All hydrogen atoms are removed for clarity.[13]

Table 3.3. Selected Bond Distances (Å) and Angles (°) for $[Mn^{III}H_2bupa(O)(H)]^{-\,a}$

Mn1–O1	1.822(4)
Mn1–N1	2.043(5)
Mn1–N2	2.169(4)
Mn1–N3	2.022(4)
Mn1–N4	2.010(5)
d(N5···O1)	2.654(5)
d(N6···O1)	2.775(5)
d(N7···O1)	2.773(5)
O1–Mn1–N1	175.34(17)
O1–Mn1–N2	95.80(17)
O1–Mn1–N3	99.56(18)
O1–Mn1–N4	99.66(18)
N4–Mn1–N1	82.94(18)
N4–Mn1–N2	114.09(18)
N4–Mn1–N3	122.23(19)
N2–Mn1–N1	79.63(18)
N2–Mn1–N3	117.36(17)
N1–Mn1–N3	82.13(19)

[a] average values are reported for the four anions in the asymmetric unit cell.[13]

that forms between hydroxido ligand and N7, resulting in a contraction of the Mn1–N4 distance. The molecular structure suggests the presence of three intramolecular H-bonds. All three H-bond interactions have O1⋯N distances of less than 2.8 Å, a distance that is below the 3.0 Å distance that is normally used to indicate an H-bond. The O1⋯N7 distance of 2.612(6) Å is significantly shorter compared to those of N5⋯O1 and N6⋯O1 (2.764(6) and 2.796(7) Å). In the previously characterized complex $[Mn^{III}H_2bupa(O)(H)]^-$, the N5⋯O1 distance of 2.654(5) Å is significantly shorter compared to those of N6⋯O1 and N7⋯O1 (2.775(5) and 2.773(5) Å).

A Mn1–O1 distance of 1.819(4) Å is observed in $[Mn^{III}H_2\mathbf{3}^{5F}(OH)]^{2-}$, which is longer than the corresponding bond length of 1.780(5) Å found in $[Mn^{III}H_3buea(O)]^{2-}$. The lengthening of the Mn1–O1 distance arises because, as discussed above, the Mn^{III} center is bound to a hydroxido ligand and not an oxido like in $[Mn^{III}H_3buea(O)]^{2-}$. However, this Mn1–O1 distance is shorter than the 1.877(2) Å observed in $[Mn^{III}H_3buea(OH)]^-$.[2] The hybrid system $[Mn^{III}H_2bupa(O)(H)]^-$ has a Mn1–O1 distance of 1.822(4) Å, which statistically identical to the 1.819(4) Å that is observed for $[Mn^{III}H_2\mathbf{3}^{5F}(OH)]^{2-}$. The Mn1–N1 distance of 2.060(5) Å was found to be more comparable to the 2.023(3) Å observed in $[Mn^{III}H_3buea(OH)]^-$ than the 2.141(5) Å observed in $[Mn^{III}H_3buea(O)]^{2-}$. This contraction of the Mn1–N1 distance is a result of a hydroxido ligand having a weaker trans influence than an oxido ligand. Additionally, in the hybrid system $[Mn^{III}H_2bupa(O)(H)]^-$ a similar Mn1–N1 distance of 2.043(5) Å is observed.[13]

Magnetic Properties. Electron paramagnetic resonance (EPR) spectroscopy was used to evaluate the spin state of the series of Mn^{III} complexes. The parallel-mode EPR spectra measured at 10K of the three complexes showed a signal centered around g ~ 8 with a six-line hyperfine pattern (Figure 3.7 andTable 3.4). This is indicative of monomeric Mn^{III} with a high-spin, S = 2 spin state. The complexes $[Mn^{III}H_3\mathbf{3}^{Ph}(O)]^{2-}$ and $[Mn^{III}H_3\mathbf{3}^{F}(O)]^{2-}$ have similar line-shape and hyperfine splitting to the previously reported $[Mn^{III}H_3buea(O)]^{2-}$. However, the complex $[Mn^{III}H_2\mathbf{3}^{5F}(OH)]^{2-}$ has a different line shape and a narrowed hyperfine splitting. A subtle change in the hyperfine splitting by 10 MHz is seen between the Mn^{III}–O and Mn^{III}–OH complexes of $[H_3buea]^{3-}$; however, a larger change of 20 MHz is seen between the $[Mn^{III}H_3\mathbf{3}^{Ph}(O)]^{2-}$ and $[Mn^{III}H_2\mathbf{3}^{5F}(OH)]^{2-}$.

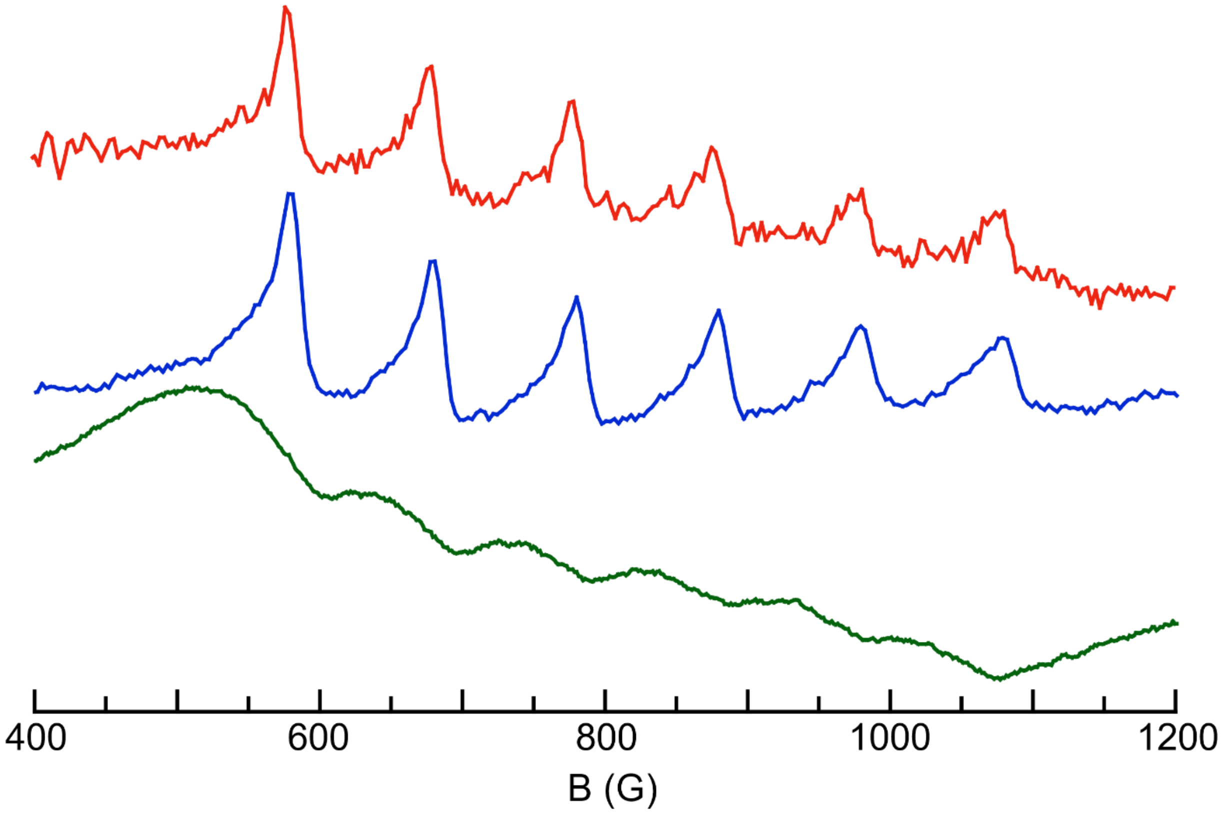

Figure 3.7. Parallel mode EPR spectra of $[Mn^{III}H_3\mathbf{3}^{Ph}(O)]^{2-}$ (red line), $[Mn^{III}H_3\mathbf{3}^{F}(O)]^{2-}$ (blue line), and $[Mn^{III}H_2\mathbf{3}^{5F}(OH)]^{2-}$ (green line) collected at 10K in a mixture of DMF:THF.

Table 3.4. EPR Properties of Mn^{III}–O(H) Complexes

	g	A (MHz)
$[Mn^{III}H_3buea(O)]^{2-}$ [a]	8.08	280
$[Mn^{III}H_3buea(OH)]^{-}$ [a]	8.14	270
$[Mn^{III}H_3\mathbf{3}^{Ph}(O)]^{2-}$	7.95	278
$[Mn^{III}H_3\mathbf{3}^{F}(O)]^{2-}$	7.95	278
$[Mn^{III}H_2\mathbf{3}^{5F}(OH)]^{2-}$	7.97	262

[a] EPR parameters previously reported for $[Mn^{III}H_3buea(O)]^{2-}$[18] and $[Mn^{III}H_3buea(OH)]^{-}$.[17]

pK_a Measurements. The pK_a was experimentally determined to observe the effect of H-bonding on the Mn^{III} complexes. $[Mn^{III}H_3buea(O)]^{2-}$ was titrated with 4-aminopyridine ($pK_a = 26.5$) and the reaction was monitored spectrophotometrically.[19] Upon addition of the acid, 4-aminopyridine, clean conversion to $[Mn^{III}H_3buea(OH)]^{-}$ is observed with spectral features matching the previously characterized complex (Figure 3.8).[20] The pK_a of $[Mn^{III}H_3\mathbf{3}^{Ph}(O)]^{2-}$ and $[Mn^{III}H_3\mathbf{3}^{F}(O)]^{2-}$ were measured by spectrophotometric titration (Figure 3.9 and Figure 3.10) with 2–aminopyrimidine ($pK_a = 25.3$).[19]

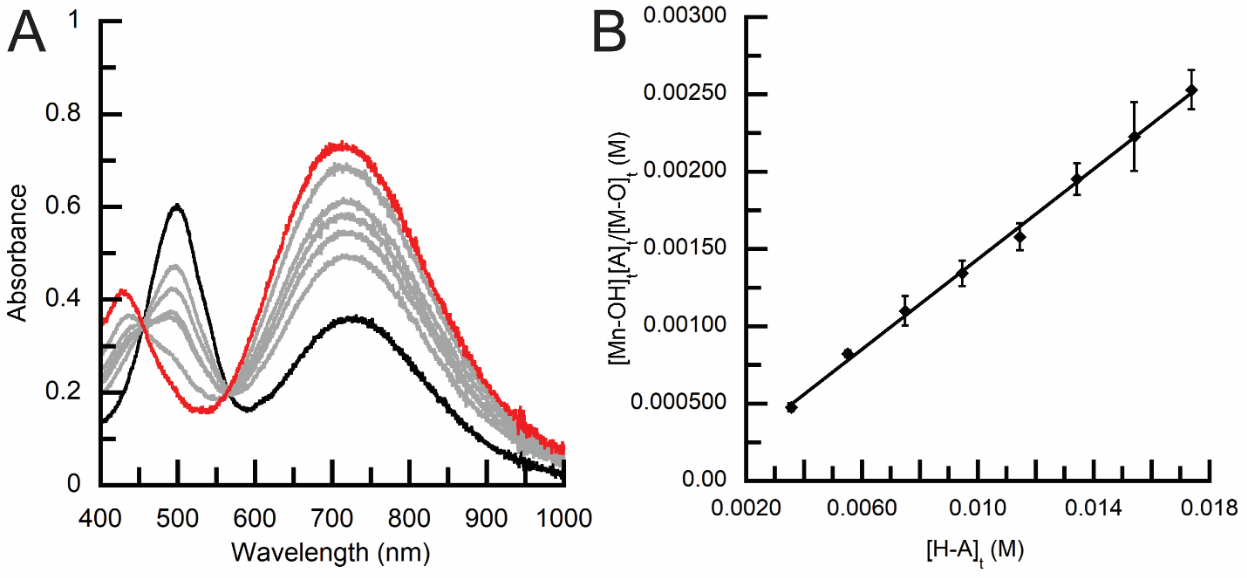

Figure 3.8. (A) Spectrophotometric titration of $[Mn^{III}H_3buea(O)]^{2-}$ with 4-aminopyridine and (B) plot of $([Mn–OH]_t/[Mn–O]_t)[A]_t$ vs. $[H\text{-}A]_t$ to determine the equilibrium constant K.

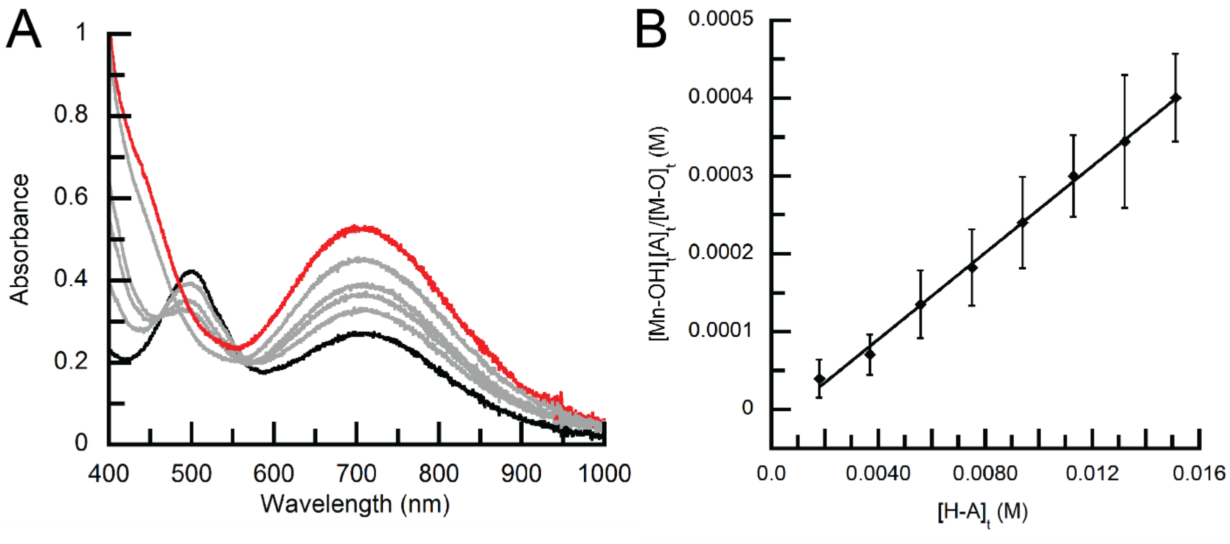

Figure 3.9. (A) Spectrophotometric titration of $[Mn^{III}H_3\mathbf{3}^{Ph}(O)]^{2-}$ with 2–aminopyrimidine and (B) plot of $([Mn–OH]_t/[Mn–O]_t)[A]_t$ vs. $[H\text{-}A]_t$, which is used to determine the equilibrium constant K.

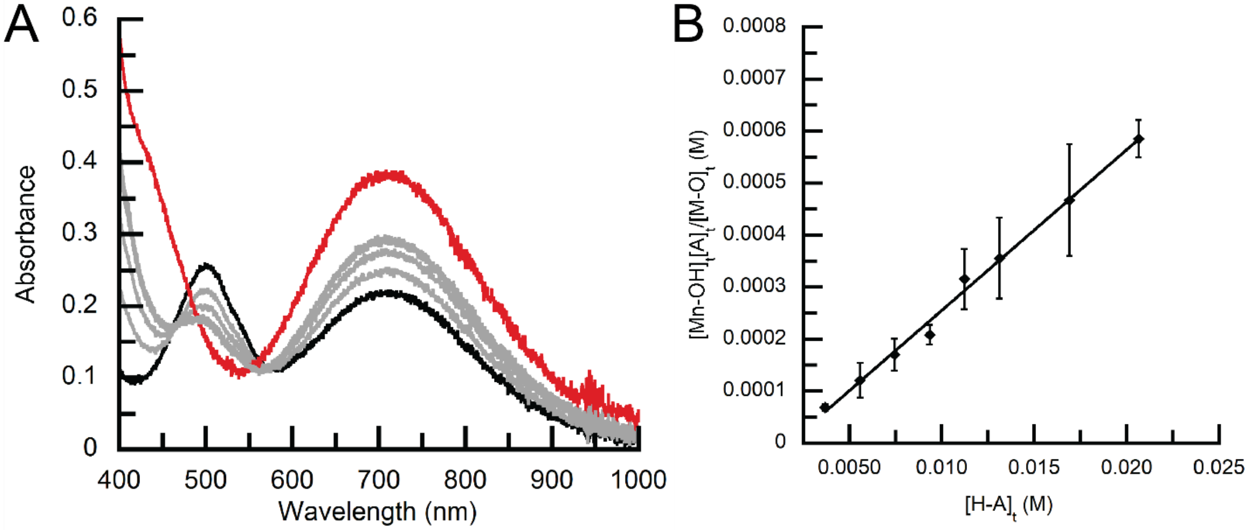

Figure 3.10. (A) Spectrophotometric titration of $[Mn^{III}H_3\mathbf{3}^{F}(O)]^{2-}$ with 2–aminopyrimidine and (B) plot of $([Mn–OH]_t/[Mn–O]_t)[A]_t$ vs. $[H\text{-}A]_t$, which is used to determine the equilibrium constant K.

The measured pK_a values for the four $Mn^{III}–O(H)$ complexes in DMSO are listed in Table 3.5. The complex $[Mn^{III}H_3buea(O)]^{2-}$ has the largest pK_a of 25.5(1) in the series. Upon adding more electron withdrawing substituents, $[Mn^{III}H_3\mathbf{3}^{Ph}(O)]^{2-}$ and $[Mn^{III}H_3\mathbf{3}^{F}(O)]^{2-}$, the pK_a drops to 23.7(1) and 23.8(1) respectively. The pK_a of $[Mn^{III}H_3\mathbf{3}^{Ph}(O)]^{2-}$ and $[Mn^{III}H_3\mathbf{3}^{F}(O)]^{2-}$ are within experimental error of each other, but they are approximately 50 times less basic than $[Mn^{III}H_3buea(O)]^{2-}$. An absolute pK_a of $[Mn^{III}H_2\mathbf{3}^{5F}(OH)]^{2-}$ was not obtained because of the limited stability of the protonated species. Attempts to bracket the pKa value was investigated by treating $[Mn^{III}H_2\mathbf{3}^{5F}(OH)]^{2-}$ with a series of acids (Scheme 3.3). The complex does not react upon addition of fluorene (pK_a = 22.6), but upon addition of indene (pK_a = 20.1), a slight growth of indenide can be seen. Finally, when imidazole (pK_a = 18.6) is added, conversion to a new species no defined absorbance bands between from 300 – 1000 nm (Figure 3.11), suggesting a bracketing of the pK_a from 22.6 to 18.6.[19]

Scheme 3.3. Reaction of $[Mn^{III}H_2\mathbf{3}^{5F}(OH)]^{2-}$ with Acids[a]

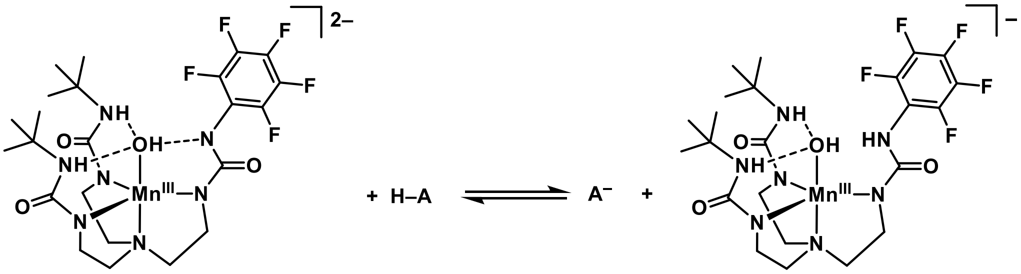

[a] H-A = fluorene, indene, imidazole.

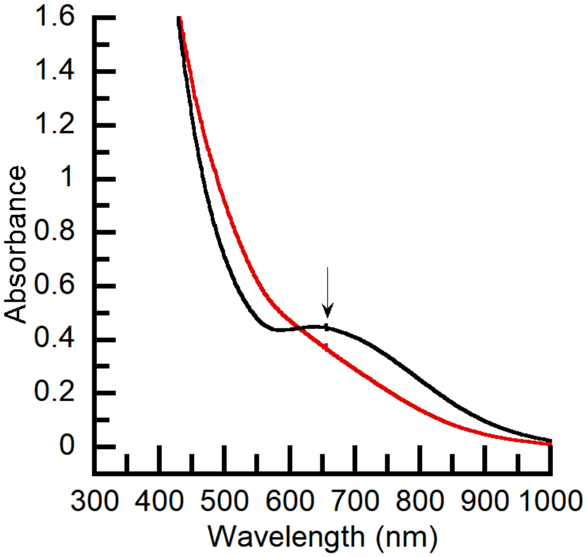

Figure 3.11. Reaction of $[Mn^{III}H_3\mathbf{3}^{5F}(OH)]^{2-}$ with imidazole in DMSO at room temperature.

These results suggest that the H-bonding network plays an important role in modulating the basicity of metal complexes. The decrease in pK_a for $[Mn^{III}H_3\mathbf{3}^{Ph}(O)]^{2-}$ and $[Mn^{III}H_3\mathbf{3}^{F}(O)]^{2-}$ could be caused by an change in a single H-bond that involves the urea arm with phenyl group. In $[Mn^{III}H_3buea(O)]^{2-}$, $[Mn^{III}H_3\mathbf{3}^{Ph}(O)]^{2-}$ and $[Mn^{III}H_3\mathbf{3}^{F}(O)]^{2-}$, the data suggests they are all Mn^{III}–oxido complexes, however, in these complexes the environment around the oxido ligand has been modulated resulting in changes in the pK_a of the NH group on the different urea-arm. There is no statistical difference in the pK_a of [Mn^{III}H$_3$**3**^{Ph}(O)]$^{2-}$ and [Mn^{III}H$_3$**3**^{F}(O)]$^{2-}$, which agrees with the *para*-Hammett parameter (σ_p) for –H is 0.00 and –F is 0.06 that suggests that their electron withdrawing properties are similar. In [Mn^{III}H$_2$**3**^{5F}(OH)]$^{2-}$, structural and spectroscopic properties indicate that the complex is a Mn^{III}–OH and is more than 1000 times less basic than [Mn^{III}H$_3$buea(O)]$^{2-}$. The most basic site in this complex is not known, but is likely the deprotonated urea nitrogen atom.

Table 3.5. Measured pK_a values of Mn^{III}–O(H) Complexes

	pK_a (DMSO, 26 °C)
[Mn^{III}H$_3$buea(O)]$^{2-}$	25.5(1)
[Mn^{III}H$_3$**3**^{Ph}(O)]$^{2-}$	23.7(1)
[Mn^{III}H$_3$**3**^{F}(O)]$^{2-}$	23.8(1)
[Mn^{III}H$_2$**3**^{5F}(OH)]$^{2-}$	22.6 – 18.6

Electrochemical Properties. Cyclic voltammetry (CV) was used to evaluate the redox properties of the Mn^{III}–O(H) complexes. CV experiments performed at room temperature in DMSO showed that each complex had a one-electron event that was assigned to the Mn^{IV}/Mn^{III} redox process (Figure 3.12 and Table 3.6). The redox process was quasi-reversible for each of the complexes. The $E_{1/2}$ potentials for the Mn^{III}–O(H) complexes ranged from –0.53 to –1.04 V vs. [FeCp$_2$]$^{+/0}$. The potentials for the Mn^{III}–O complexes ranged from –0.80 V to –1.04 V vs. [FeCp$_2$]$^{+/0}$. The complex with the symmetrical ligand, [Mn^{III}H$_3$buea(O)]$^{2-}$ has the most negative $E_{1/2}$ values. The $E_{1/2}$ value shifts 240 mV more positive in [Mn^{III}H$_3$**3**^{F}(O)]$^{2-}$. This effect could arise from the stronger H-bonding interaction to the oxido ligand from the *para*-fluorophenyl urea NH. This stronger H-bonding interaction makes the oxido ligand a weaker donor to the Mn^{III} center than in [Mn^{III}H$_3$buea(O)]$^{2-}$. Moreover, the $E_{1/2}$ value shifts to – 0.53 V vs. [FeCp$_2$]$^{+/0}$ in [Mn^{III}H$_2$**3**^{5F}(OH)]$^{2-}$, which likely arises from a combination of two effects. The first effect is that the primary coordination sphere around the Mn^{III} center has changed; the fifth ligand is now a hydroxido, which is a weaker donor to the Mn^{III} center than an oxido. The second effect is the change in the H-bond network in the secondary coordination sphere of $[Mn^{III}H_2\mathbf{3}^{5F}(OH)]^{2-}$. The Mn^{III}–O(H) complexes in this series systemically change only one H-bond in the secondary coordination sphere resulting in significant changes to the redox properties of these compounds.

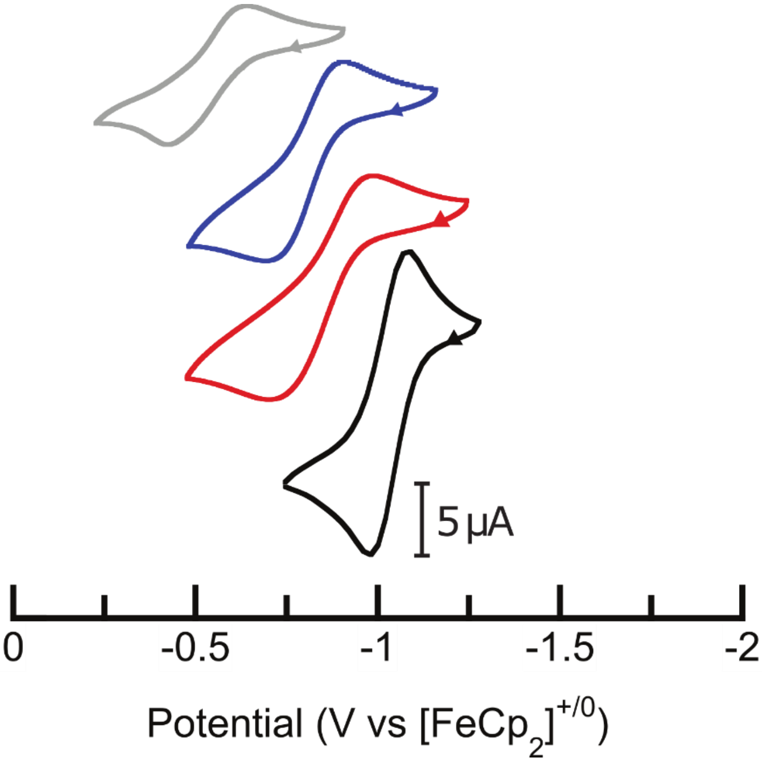

Figure 3.12. Cyclic voltammograms of $[Mn^{III}H_3buea(O)]^{2-}$ (black line), $[Mn^{III}H_3\mathbf{3}^{Ph}(O)]^{2-}$ (red line), $[Mn^{III}H_3\mathbf{3}^{F}(O)]^{2-}$ (blue line), and $[Mn^{III}H_2\mathbf{3}^{5F}(OH)]^{2-}$ (grey line) recorded in DMSO. Measurements were done at room temperature under argon at 50 mV s^{-1}.

Table 3.6. Electrochemical Properties of Mn^{III}–O(H) Complexes Recorded in DMSO

	$E_{1/2}$ (V vs. $[FeCp_2]^{+/0}$)
$[Mn^{III}H_3buea(O)]^{2-}$	– 1.04
$[Mn^{III}H_3\mathbf{3}^{Ph}(O)]^{2-}$	– 0.84
$[Mn^{III}H_3\mathbf{3}^{F}(O)]^{2-}$	– 0.80
$[Mn^{III}H_2\mathbf{3}^{5F}(OH)]^{2-}$	– 0.53

Kinetic Properties. Our group has previously reported the reactivity of $[Mn^{III}H_3buea(O)]^{2-}$ with the substrate 9,10-dihydroanthracene (DHA) and determined a second-order rate constant and activation parameters.[4] This organic substrate oxidation occurs even though the Mn^{III}–O complex has redox potentials that are extremely negative and are typically associated with reductants ($E_{1/2}$($[Mn^{III}H_3buea(O)]^{2-}$ = – 1.04 V vs $[FeCp_2]^{+/0}$) . The low value of the $E_{1/2}$ suggests that the basicity of the Mn^{III}–O may play an important role in the observed reactivity. To gain further insight into how the reactivity of Mn^{III}–O species reactivity is influenced by H-bonds to the Mn^{III}–O unit, a kinetic analysis was conducted for the reaction involving DHA.

Kinetic data were obtained by spectrophotometrically monitoring absorbance features corresponding to the Mn^{III}–O compounds during their reaction with excess DHA in DMSO solutions (Figure 3.13). Under these conditions, the reactions with Mn^{III}–O and DHA exhibited pseudo-first-order kinetics for greater than 3 half-lives. The pseudo-first-order rate constant (k_{obs}) varied linearly with the concentration of DHA, which indicates a second-order rate law (rate = k[Mn–O(H)][DHA]) (Table 3.7)). For $[Mn^{III}H_3buea(O)]^{2-}$, the second order rate constant at 20 °C (k = 0.48(4) M^{-1} s^{-1}) is more than an *order of magnitude larger* than the second order rate constant for $[Mn^{III}H_3\mathbf{3}^{Ph}(O)]^{2-}$ and $[Mn^{III}H_3\mathbf{3}^{F}(O)]^{2-}$ (k = 0.030(2) and 0.019(2) M^{-1} s^{-1}, respectively) (Figure 3.14 and Figure 3.15).[4] The complex $[Mn^{III}H_2\mathbf{3}^{5F}(OH)]^{2-}$ reacts with DHA on a time-scale that is too slow to determine a second order rate constant. Even at elevated temperatures up to 50 °C, the reaction with excess DHA does not go through one half-life within a 24 h period.

Table 3.7. Second Order Rate Constants in the Reaction of DHA with $Mn^{III/IV}$–O(H) Complexes

	k (M^{-1} s^{-1})
$[Mn^{III}H_3buea(O)]^{2-}$ [a]	0.48(4)
$[Mn^{IV}H_3buea(O)]^{2-}$ [a]	0.026(2)
$[Mn^{III}H_3\mathbf{3}^{Ph}(O)]^{2-}$	0.030(2)
$[Mn^{III}H_3\mathbf{3}^{F}(O)]^{2-}$	0.019(2)
$[Mn^{III}H_2\mathbf{3}^{5F}(OH)]^{2-}$	Too Slow

[a] kinetic data obtained from ref [4]

The temperature dependence of the second order rate constants were determined for $[\mathrm{Mn^{III}H_3}\mathbf{3}^{\mathrm{Ph}}\mathrm{(O)}]^{2-}$ to probe if there were differences in the previously reported activation parameters for $[\mathrm{Mn^{III}H_3buea(O)}]^{2-}$ (Figure 3.14 and Table **3.8**).[4] Activation parameters ($\Delta H^{\ddagger}$, $\Delta S^{\ddagger a}$, or $\Delta G^{\ddagger}$) were calculated from an Eyring analysis. $[\mathrm{Mn^{III}H_3buea(O)}]^{2-}$ and $[\mathrm{Mn^{III}H_3}\mathbf{3}^{\mathrm{Ph}}\mathrm{(O)}]^{2-}$ show positive enthalpy and negative entropy of activation, indicating that the reaction proceeds through an associative mechanism. However, the activation parameters for $[\mathrm{Mn^{III}H_3buea(O)}]^{2-}$ and $[\mathrm{Mn^{III}H_3}\mathbf{3}^{\mathrm{Ph}}\mathrm{(O)}]^{2-}$ are not statistically different, suggesting that the transition state is similar for the two reactions. This is expected for the free energy of activation ($\Delta G^{\ddagger}$) because an order of magnitude difference in rate constant is equivalent to ~1.3 kcal mol^{-1} ($\Delta G^{\ddagger} = RT\ln k^{\ddagger}$), which is within error for the experiment.

One possible reason for the large difference in rate constants $[\mathrm{Mn^{III}H_3buea(O)}]^{2-}$ and the new $\mathrm{Mn^{III}{-}O(H)}$ complexes is the basicity of the complexes in the series. With the increased H-bonding in complexes with $[\mathrm{H_3}\mathbf{3}^{\mathrm{Ph}}]^{3-}$, $[\mathrm{H_3}\mathbf{3}^{\mathrm{F}}]^{3-}$, and $[\mathrm{H_2}\mathbf{3}^{\mathrm{5F}}]^{4-}$ ligands, the basicity of these complexes is less than those with $[\mathrm{H_3buea}]^{3-}$. This reactivity could occur by a two-step mechanism where proton transfer occurs then electron transfer (PT-ET mechanism). If the reaction proceeded by a PT-ET mechanism, lower basicity could result in slower reaction kinetics. The complex $[\mathrm{Mn^{IV}H_3buea(O)}]^{-}$ has a significantly lower $\mathrm{p}K_\mathrm{a}$ and rate constant than $[\mathrm{Mn^{III}H_3buea(O)}]^{2-}$ ($\Delta \mathrm{p}K_\mathrm{a} \sim 10$, $k^{\mathrm{Mn(III)}}/k^{\mathrm{Mn(IV)}} \sim 20$), suggesting that the $\mathrm{p}K_\mathrm{a}$ could play an important role in this reaction. More electron withdrawing and donating substituents are necessary to probe the relationship between H-bonding strength, $\mathrm{p}K_\mathrm{a}$, and reaction kinetics.

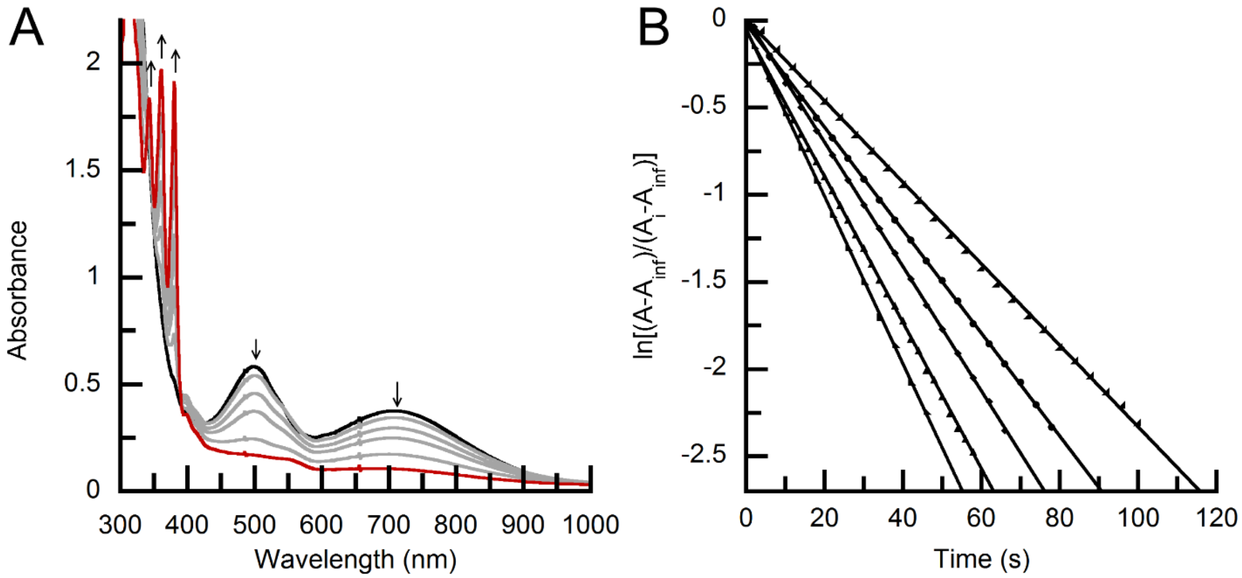

Figure 3.13. (A) Example of the spectrophotometric data for the reaction of Mn^{III}–O with DHA and (B) example of rate data used to determine the k_{obs} values for $[Mn^{III}H_3\mathbf{3}^{Ph}(O)]^{2-}$ at 20° C. Each independent linear fit represents a different concentration of DHA.

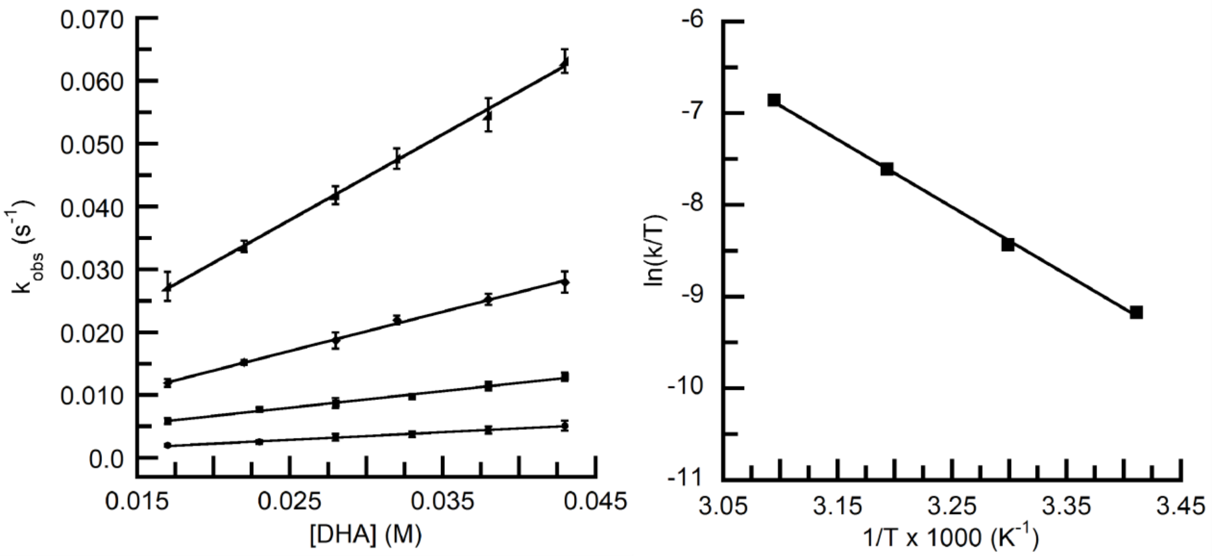

Figure 3.14. Kinetic data for the reaction of $[Mn^{III}H_3\mathbf{3}^{Ph}(O)]^{2-}$ with DHA at various temperatures to determine second order rate constants (A) and Eyring plot (B). Temperature Key (°C): 20 (•); 30 (■); 40 (♦); 50 (►).

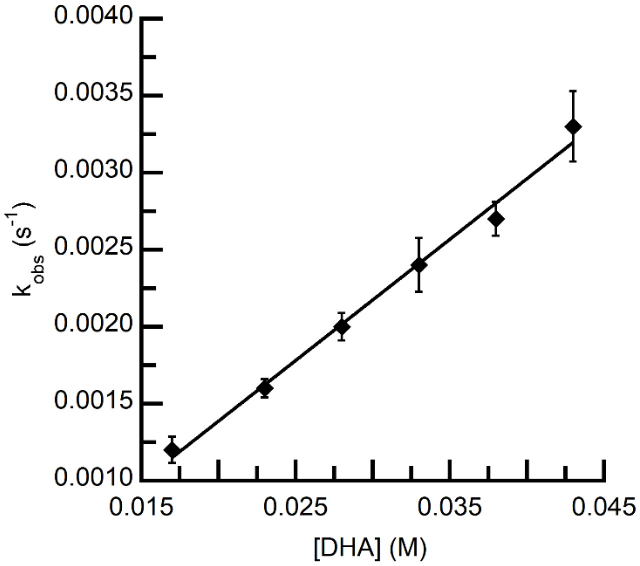

Figure 3.15. Kinetic data for the reaction of $[Mn^{III}H_3\mathbf{3}^F(O)]^{2-}$ with DHA at 20 °C to determine the second order rate constant.

Table 3.8. Activation Parameters for Reaction of $Mn^{III/IV}(O)$ Complexes with DHA

	$[Mn^{III}H_3\mathbf{3}^{Ph}(O)]^{2-}$	$[Mn^{III}H_3buea(O)]^{2-}$	$[Mn^{IV}H_3buea(O)]^{2-}$
$\Delta H^{\ddagger a}$	15(1)	14(2)	5(1)
$\Delta S^{\ddagger b}$	−16(2)	−14(6)	- 49(4)
$\Delta G^{\ddagger a,c}$	20(2)	18(3)	19(2)
k^d	0.030(2)	0.48(4)	0.026(2)

[a] kcal mol^{-1}. [b] eu. [c] 20 °C. [d] M^{-1} s^{-1}. $[Mn^{III}H_3buea(O)]^{2-}$ and $[Mn^{IV}H_3buea(OH)]^{2-}$ were previously reported.[4]

Summary and Conclusion

In this chapter, a new series of hybrid tripodal urea ligands and the corresponding Mn^{III}–O(H) complexes were reported: $[Mn^{III}H_3\mathbf{3}^F(O)]^{2-}$, $[Mn^{III}H_3\mathbf{3}^H(O)]^{2-}$, and $[Mn^{III}H_2\mathbf{3}^{5F}(OH)]^{2-}$. All three have similar trigonal bipyramidal coordination geometry with an N_4O donor set coordinated to the Mn center. They differ in that one arm of the tripodal ligand was modified with a substituted-phenyl urea, which allows for systematic modulation of the acidity, and H-bond donor ability, of a single urea NH located in the secondary coordination sphere. Changes in H-bond donor strength of the phenyl urea NH group allowed for the investigation how a single H-bond can influence the structural, physical and reactivity properties of a metal-oxido complexes. This approach and subsequent study showed that the position of the proton can be modulated within the cavity that surrounds a Mn^{III}–O unit: in $[Mn^{III}H_2\mathbf{3}^{5F}(OH)]^{2-}$, structural and spectroscopic evidence suggest that proton resides on the oxido ligand to form a hydroxido species. In the other two hybrid systems, $[Mn^{III}H_3\mathbf{3}^{F}(O)]^{2-}$ and $[Mn^{III}H_3\mathbf{3}^{Ph}(O)]^{2-}$, the measured properties suggest Mn^{III}–oxido species are present. In the three complexes, there are three intramolecular H-bond involving the Mn^{III}–oxido unit; for $[Mn^{III}H_3\mathbf{3}^{F}(O)]^{2-}$ and $[Mn^{III}H_3\mathbf{3}^{Ph}(O)]^{2-}$ the network is the same to that found in the parent complex, $[Mn^{III}H_3buea(O)]^{2-}$ with the three NH groups of the urea arms serving as H-bond donors. In $[Mn^{III}H_2\mathbf{3}^{5F}(OH)]^{2-}$ there are still three intramolecular H-bonds but the network is different because one H-bond is reversed. Structural and spectroscopic results agree that the proton from the phenyl-urea arm appears to have moved to the Mn^{III}–O unit (forming a hydroxido ligand) and remaining N atom is deprotonated (that is, $Mn–OH\cdots N_{urea}$ is present). and thus the H-bond changes is the donor group and a deprotonated in N-atom of the urea. Evidence that support this premise is a significant contraction of the Mn1–O1 distance and shift to more positive Mn^{IV}/Mn^{III} potential compared to other Mn^{III}–oxido complexes. Moreover, there is a large change in the reactivity toward C–H bond activation. In $[Mn^{III}H_3\mathbf{3}^{F}(O)]^{2-}$ and $[Mn^{III}H_3\mathbf{3}^{Ph}(O)]^{2-}$ second order rate constants could be measured that are approximately an order of magnitude smaller than that observed for $[Mn^{III}H_3buea(O)]^{2-}$. The exact reason for this difference is not yet known and other complexes in this series are being studied by other members of our group to gain more insights. Nevertheless, this reaction is nearly stopped in $[Mn^{III}H_2\mathbf{3}^{5F}(OH)]^{2-}$, a result that we argue is predominatly caused by the changes in the orientation of a single H-bond within the secondary coordination sphere. These results show the strong effect that H-bonds have on the properties of metal-oxido complexes and their influence on chemical reactivity.

Experimental Section

General Procedures. Unless otherwise stated, all manipulations were performed under an argon atmosphere in a Vac-atmospheres dry box. *N,N*-Dimethylacetamide was purchased from Sigma-Aldrich in 99.8% purity and stirred over BaO for two days, refluxed for 1 h, followed by vacuum distillation. 1-tert-Butyl-3–(2–chloroethyl)urea, N-tert-Butoxycarbonyl–1,2–diaminoethane, 1,1'-(((2–aminoethyl)azanediyl)bis(ethane-2,1-diyl))bis(3–(tert-butyl)urea), (*N*'-*tert*-butyoxycarbonyl)-*N*-ethyl]-bis[(*N*'-*tert*-butylureayl)-*N*-ethyl]amine, ligand precursor 1,1′,1″-(nitrilotris(ethane-2,1-diyl))tris(3–(*tert*-butyl)urea) (H_6buea) and the metal complex $K_2[Mn^{III}H_3buea(O)]$ were synthesized using literature procedures.[8–11] (*N*'-*tert*-butyoxycarbonyl)-*N*-ethyl]-bis[(*N*'-*tert*-butylureayl)-*N*-ethyl]amine was purified by flash chromatography over silica gel, eluting with 10% MeOH, 1% Triethylamine, and 89% EtOAc. The metal precursor $Mn^{II}(OAc)_2$ was purchased from Sigma-Aldrich in ≥ 99% purity and used as received. Potassium hydride (KH) as a 30% dispersion in mineral oil was filtered with a glass frit and washed with pentane and Et_2O, dried by vacuum, and stored under an argon atmosphere. DHA was purchased from Sigma-Aldrich in ≥ 99% purity and crystallized from ethanol three times, washed with pentane, and dried by vacuum. 4-Aminopyridine was purchased from Sigma-Aldrich in ≥ 99% purity and crystallized from toluene and washed with Et_2O and dried by vacuum. 2–Aminopyrimidine was purchased from Sigma-Aldrich in 97% purity and crystallized from EtOH three times, washed with Et_2O and dried by vacuum.

Physical Methods. Electronic absorption spectra for kinetics experiments were recorded in a 1 cm cuvette on an 8453 Agilent UV-Vis spectrometer equipped with an Unisoku Unispeks cryostat. Room temperature electronic absorption spectra for determining extinction coefficients were recorded in a 1 cm cuvette on a Cary 50 spectrometer. Room temperature electronic absorption spectra for measuring the pK_a of the complexes were recorded in a 1 cm cuvette on a Cary 60 in a N_2 atmosphere glove box connected by fiber optic cables. EPR spectra were recorded using a Bruker EMX spectrometer equipped with an ER041XG microwave bridge, an Oxford Instrument liquid-helium quartz cryostat, and a dual mode cavity (ER4116DM). ^1H and ^{13}C nuclear magnetic resonance (NMR) spectroscopies were conducted using a Bruker DRX500 spectrometer. Cyclic voltammetric experiments were conducted using a CHI600C electrochemical analyzer. A 2.0 mm glassy carbon electrode was used as the working electrode at scan velocities of 50 mV s^{-1}. A ferrocenium/ferrocene couple ($FeCp_2^+/FeCp_2$) was used to monitor the Ag wire reference electrode, and all potentials are referenced to the $[FeCp_2]^{+/0}$.

X-Ray Crystallographic Methods. A Bruker SMART APEX II diffractometer was used for molecular structure determination. The APEX2[21] program package was used to determine the unit-cell parameters and for data collection. The raw data was processed using SAINT[22] and SADABS[23] to yield the reflection data file. Subsequent calculations were carried out using the SHELXTL[24] program. The structures were solved by direct methods and refined to convergence. The analytical scattering factors[25] for neutral atoms were used throughout the analysis. Hydrogen atoms on O1, N5, and N6 were located from a difference-Fourier map and refined (x,y,z and U_{iso}) and the remaining hydrogen atoms were included using a riding model.

Table 3.9. Crystallographic Data for $(NMe_4)_2[Mn^{III}H_2 3^{5F}(OH)]$•2MeCN

	$(NMe_4)_2[Mn^{III}H_2\mathbf{3}^{5F}(OH)]$•2MeCN
Empirical Formula	$C_{35}H_{63}F_5MnN_{11}O_4$
Fw	851.90
T (K)	128(2)
space group	$P\bar{1}$
a (Å)	9.648(3)
b (Å)	13.538(4)
c (Å)	17.653(5)
α (deg)	73.166(4)
β (deg)	82.859(4)
γ (deg)	79.983(4)
Z	2
V (Å^3)	2166.6(10)
δ_{calcd} (Mg/m^3)	1.306
R1	0.0916
wR2	0.2662
GOF	1.007

Kinetic Studies of Mn^{III} Complexes with Substrates. For a typical experiment, a 1-2 mM stock solution of Mn^{III} complex was prepared in DMSO. The concentration of each Mn^{III} complex was determined using the extinction coefficient at λ_{max} = 498 nm. A Mn^{III} complex solution (2 mL) was added to a 1 cm cuvette containing a stir-bar using a volumetric pipette. Stock solutions of substrates were prepared by dissolving 400 to 500 mg in DMSO in a 5 mL volumetric flask to generate solutions between 400-500 mM. Solutions of substrates were injected by gas-tight syringes and the progress of the reaction was monitored optically. Experiments at each temperature were repeated at least three times. The second order rate constant for the reaction of $[Mn^{III}H_3buea(O)]^{2-}$ with DHA was experimentally determined (0.52(4) M^{-1} s^{-1}) and compared to the previously reported rate (0.48(4) M^{-1} s^{-1}), and the two second order rate constants were found to be within experimental error (Figure 3.16).

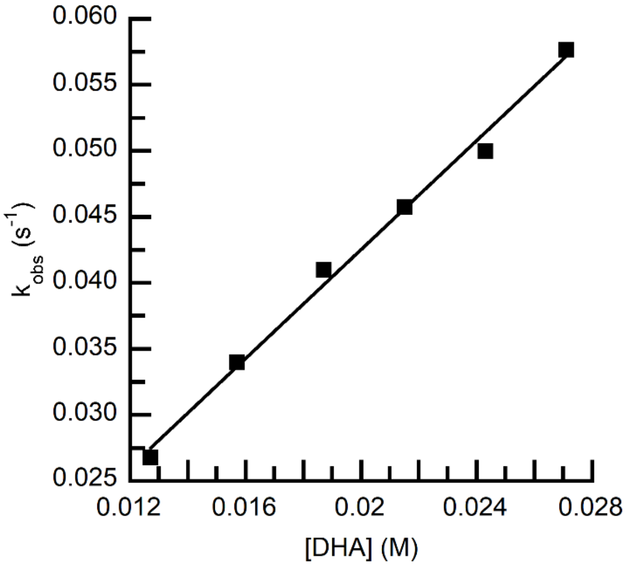

Figure 3.16. Kinetic data for the reaction of $[Mn^{III}H_3buea(O)]^{2-}$ with DHA at 20 °C to determine the second order rate constant.[4]

All kinetic experiments were performed with an excess of substrate to achieve pseudo-first-order reaction conditions. The absorbance at time 't' (A) of a sample was recorded until there was no further changes in the absorbance spectrum. The final absorbance was used as the endpoint for the reaction (A_{inf}). Time was plotted against the expression, $\ln[(A - A_{inf})/(A_i - A_{inf})]$ (A_i is the initial absorbance) for the first three half-lives of a given reaction to give a linear relationship. The observed pseudo first-order rate constants (k_{obs}, s^{-1}) for each reaction were determined from the plot of $\ln[(A - A_{inf})/(A_i - A_{inf})] = 2(k_{obs})(t)$ (Figure 3.13). The factor of 2 is necessary to account for the stoichiometry of the reaction which involves two equiv of Mn^{III} to 1 equiv of DHA. The concentration of DHA was plotted against the observed pseudo-first-order rate constant k_{obs} to give a linear relationship, where the slope is the second-order rate constant using the relationship $k_{obs} = k'[DHA]$. The second-order rate constants were divided by 4 to normalize for the 4 reactive C–H bonds per DHA molecule ($k = k'/4$).

Activation parameters were derived from the Eyring plot of 1/T vs. ln(k/T), where T is the temperature for each experiment (20, 30, 40, or 50 °C) and k is the corrected second-order rate constant for each reaction.

$$\ln\left(\frac{k}{T}\right) = -\frac{\Delta H^{\ddagger}}{R}\frac{1}{T} + ln\frac{k_B}{h} + \frac{\Delta S^{\ddagger}}{R} \qquad \text{(Eq 3.1)}$$

pK_a Measurements of Mn^{III} Compounds. For a typical experiment, a 1-2 mM stock solution of Mn^{III} complex was prepared in DMSO. The concentration of each Mn^{III} complex was determined using the extinction coefficient at λ_{max} = 498 nm. A solution of Mn^{III} complex (3 mL) was added to a 1 cm cuvette using a volumetric pipette. Stock solutions of acids were prepared with concentrations between 0.5-2M. Solutions of acids were injected using 10–100 µL syringe and the solutions were allowed to mix and come to equilibrium before each titration point was monitored optically. $[Mn^{III}H_3buea(O)]^{2-}$ was titrated with the acid 4-aminopyridine (pK_a = 26.5 in DMSO).[19] $[Mn^{III}H_3\mathbf{3}^{Ph}(O)]^{2-}$ and $[Mn^{III}H_3\mathbf{3}^{F}(O)]^{2-}$ were titrated with the acid 2–aminopyrimidine (pK_a = 25.3 in DMSO).[19]

The pK_a was determined from the plot of [H–A] vs. $[Mn–OH][A^-]/[Mn–O]$. The concentrations of [Mn–O], [Mn–OH], [H–A], and $[A^-]$ were determined assuming mass balance. At the wavelengths monitored, the absorbance due to [H–A] and $[A^-]$ are negligible and are excluded. Equation 4.1 describes the initial absorbance at any wavelength, when the solution is purely Mn^{III}–O. The quantity $[H–A]_x$ describes the amount of acid added to the solution at any given titration point.

$$A_i = \epsilon_{Mn-O} l [Mn - O]_i \qquad \text{(Eq 3.2)}$$

Equation 4.4 describes the final absorbance at any wavelength. The solution is purely Mn^{III}–OH and excess acid has been added to convert fully to Mn–OH.

$$A_f = \epsilon_{Mn-OH} l [Mn - OH]_f \qquad \text{(Eq 3.3)}$$

During the titration, the total concentration of $\mathrm{Mn^{III}}$ is equal to the initial concentration of [Mn–O] and the final concentration [Mn–OH], as described in equation 4.5.

$$[Mn-O]_i = [Mn-OH]_f = [Mn-O]_t + [Mn-OH]_t \qquad \text{(Eq 3.4)}$$

The total concentration of acid/conjugate base at equilibrium is equal to the amount of acid added, as described by equation 4.6.

$$[H-A]_x = [A]_t + [H-A]_t \qquad \text{(Eq 3.5)}$$

Assuming mass balance, as described above, the ratio of [Mn–OH]/Mn–O] at any point in the titration can be described by equation 4.7.

$$\frac{A_t-A_i}{A_f-A_t} = \frac{\epsilon_{Mn-O}[Mn-O]_t+\epsilon_{Mn-OH}[Mn-OH]_t - \epsilon_{Mn-O}[Mn-O]_i}{\epsilon_{Mn-OH}[Mn-OH]_f-\epsilon_{Mn-O}[Mn-O]_t-\epsilon_{Mn-OH}[Mn-OH]_t} =$$

$$\frac{\epsilon_{Mn-O}([Mn-O]_t-[Mn-O]_i)+\epsilon_{Mn-OH}[Mn-OH]_t}{\epsilon_{Mn-OH}([Mn-OH]_f-(Mn-OH]_t)-\epsilon_{Mn-O}[Mn-O]_t} = \frac{\epsilon_{Mn-OH}[Mn-OH]_t-\epsilon_{Mn-O}[Mn-OH]_t}{\epsilon_{Mn-OH}[Mn-O]_t-\epsilon_{Mn-O}[Mn-O]_t} = \frac{[Mn-OH]_t}{[Mn-O]_t} \qquad \text{(Eq 3.6)}$$

Rearrangement of equation 4.7, gives the concentration of Mn–OH as a function of Mn–O at each titration point, as described in equation 4.8.

$$\frac{A_t-A_i}{A_f-A_t}[Mn-O]_t = [Mn-OH]_t \qquad \text{(Eq 3.7)}$$

Combining equation 4.5 and 4.8 gives the concentration of Mn–OH in terms of initial concentration of Mn–O, as described in equation 4.9

$$[Mn-OH]_t = \frac{\frac{A_t-A_i}{A_f-A_t}}{1+\frac{A_t-A_i}{A_f-A_t}}\ [Mn-O]_i \qquad \text{(Eq 3.8)}$$

At equilibrium, the concentration of Mn–OH is equal to the concentration of A^- (equation 4.10)

$$[Mn-OH]_t = [A^-]_t \qquad \text{(Eq 3.9)}$$

Combining equation 4.6 and 4.10, gives equation 4.11, which gives the amount of available acid in solution, relative to the amount of Mn–OH.

$$[H-A]_t = [H-A]_x - [Mn-OH]_t \qquad \text{(Eq 3.10)}$$

The reaction at equilibrium is described by equation 4.12.

$$Mn-O + H-A \rightleftharpoons Mn-OH + A^- \qquad \text{(Eq 3.11)}$$

Therefore, the equilibrium constant for the reaction is described by equation 4.13.

$$K = \frac{[Mn-OH]_t[A^-]_t}{[Mn-O]_t[H-A]_t} \qquad \text{(Eq 3.12)}$$

Equation 4.13 can be rearranged to yield equation 4.14.

$$[H-A]_t K = \frac{[Mn-OH]_t[A^-]_t}{[Mn-O]_t} \qquad \text{(Eq 3.13)}$$

Therefore, a plot of $[H–A]_t$ vs. $([Mn–OH]_t/[Mn–O]_t)[A^-]_t$ gives the equilibrium constant K. These values are given by the previous equations. The pK_a can be obtained by using equation 4.15.

$$pK_a(Mn-OH) = \log K + pK_a(H-A) \qquad \text{(Eq 3.14)}$$

Each titration was done three times and the error in pK_a is reported as ± 2σ.

Preparative Methods.

1-(2–(bis(2–(3–(tert-butyl)ureido)ethyl)amino)ethyl)-3–phenylurea (H_63^{Ph}). 1,1'-(((2–aminoethyl)azanediyl)bis(ethane-2,1-diyl))bis(3–(tert-butyl)urea) (2.71 g, 7.86 mmol) was dissolved in 60 mL of CH_2Cl_2 and cooled to 0 ^{0}C in an ice bath. Phenyl isocyanate (0.961 g, 0.807 mmol) was dissolved in 60 mL of CH_2Cl_2 and was added dropwise to the amine over 1 h. The ice bath was removed and the reaction was stirred overnight. Volatiles were removed under reduced pressure to give a white solid. The white solid was purified by column chromatography over silica gel, eluting with EtOAc followed by 5:100 MeOH/EtOAc and then 10:100 MeOH/EtOAc to give 2.70 g of the desired product (75%) . ^{1}H NMR (500 MHz, DMSO, ppm): 1.27 (s, 18H), 2.56 (m, 6H), 3.07 (q, 4H), 3.18 (q, 2H), 5.77 (m, 4H) 6.26 (t, 1H), 6.93 (t, 1H), 7.26 (t, 2H), 7.45 (d, 2H), 8.59 (s, 1H). ^{13}C NMR (500 MHz, CDCl$_3$, ppm): 158.91, 157.03, 139.72, 128.98, 122.31, 119.03, 55.65, 50.12, 38.36, 29.71. HRMS (ES$^+$) [$C_{23}H_{41}N_7O_3$ + Na$^+$], 486.3169. Found 486.3159. FTIR (ATR, cm^{-1}): 3319, 2963, 1632, 1498, 1442, 1389, 1360, 1276, 1212, 1070, 751, 693.

1-(2–(bis(2–(3–(tert-butyl)ureido)ethyl)amino)ethyl)-3–(4-fluorophenyl)urea (H$_6$3^F). The ligand precursor was prepared using a similar procedure described above for H$_6$**3**^{Ph} with 4-fluorophenyl isocyanate (0.446 g, 3.25 mmol) and 1,1'-(((2–aminoethyl)azanediyl)-bis(ethane-2,1-diyl))bis(3–(tert-butyl)urea) (1.15 g, 3.33 mmol). The white solid was isolated after removal of solvents by vacuum and purified by column chromatography over silica gel, eluting with EtOAc followed by 5:100 MeOH/EtOAc and then 15:100 MeOH/EtOAc to give 1.2 g of the desired product (77%). ^{1}H NMR (500 MHz, CDCl$_3$, ppm): 1.25 (s, 18 H), 2.43 (m, 6H), 3.11 (q, 4H), 3.21 (q, 2H), 5.02 (s, 2H), 5.62 (t, 2H), 6.69 (t, 1H), 6.93 (m, 2H), 7.36 (m, 2H), 8.00 (s, 1H). ^{13}C NMR (500 MHz, CDCl$_3$, ppm): 158.96, 156.92, 135.77, 120.58, 115.52, 55.55, 50.21, 38.33, 29.59. HRMS (ES+) [$C_{23}H_{40}FN_7O_3$ + Na$^+$], 504.3074. Found 504.3054. FTIR (ATR, cm^{-1}): 3318, 2965, 3070, 1635, 1549, 1506, 1453, 1361, 1390, 1276, 1205, 829, 769.

1-(2–(bis(2–(3–(tert-butyl)ureido)ethyl)amino)ethyl)-3–(perfluorophenyl)urea (H$_6$3^{5F}). The ligand precursor was prepared using a similar procedure described above for H$_6$**3**^{Ph} with pentafluorophenyl isocyanate (0.458 g, 3.84 mmol) and 1,1'-(((2–aminoethyl)azanediyl)bis(ethane-2,1-diyl))bis(3–(tert-butyl)urea) (1.26 g, 3.67 mmol). The white solid was isolated after removal of solvents by vacuum and was purified by column chromatography over silica gel, eluting with EtOAc followed by 5:100 MeOH/EtOAc and then 10:100 MeOH/EtOAc to give 1.60 g of the desired white solid (78 %). ^{1}H NMR (500 MHz, $CDCl_3$, ppm): 1.27 (s, 18H), 2.49 (m, 4H), 2.57 (m, 4H), 3.14 (q, 4H), 3.25 (q, 2H), 5.00 (s, 2H), 5.56 (t, 2H), 7.13 (t, 1H), 7.84 (s, 1H). ^{13}C NMR (500 MHz, $CDCl_3$, ppm): 159.02, 156.04, 144.06, 142.15, 139.94, 138.73, 137.94, 136.74, 67.98, 55.67, 50.03, 38.89, 38.43, 29.47, 25.63 . HRMS (ES+) [$C_{23}H_{36}N_7O_3F_5 + H^+$], 554.2878. Found 554.2894. FTIR (ATR, cm^{-1}): 3306, 2967, 2932, 2870, 2826, 1634, 1555, 1519, 1452, 1392, 1360, 1323, 1271, 1240, 1211, 1170, 1108, 1070, 1036, 1005, 882, 763, 657.

$K_2[Mn^{III}H_3\mathbf{3}^{Ph}(O)]$. Solid KH (0.0501 g, 1.25 mmol) was treated with a 3 mL DMA solution of $H_6\mathbf{3}^{Ph}$ (0.1429 g, 0.3082 mmol) and stirred for 45 min until bubbling ceased. $Mn^{II}(OAc)_2$ (0.0534 g, 0.309 mmol) was then added as one portion and the resultant solution was stirred for 1 h to give a colorless heterogeneous mixture. The mixture was transferred to a Schlenk flask and sealed with a rubber septum and treated with dry O_2 (3.5 mL, 0.16 mmol), which produced a purple color immediately. The mixture was allowed to stir for 2 h, then degassed under vacuum for 5 min. The purple mixture was filtered through a medium porous-glass filter, and 10 mL of Et_2O was allowed to diffuse resulting in a purple precipitate after 2 d. The purple precipitate was collected on a medium porous-glass filter and washed with 20 mL of MeCN and 20 mL of Et_2O to give 0.089 g of the desired purple solid (47%). $\lambda_{max/nm}$ (DMSO, ε, M^{-1} cm^{-1}): 710, (240); 498, (438). EPR (DMF:THF, 10 K): g = 8.03, A = 277 MHz). MS (ES+): [$C_{23}H_{38}K_2MnN_7O_4 + 3K^+$], 648.13; Found, 648.00. Anal. Calcd (found) for $C_{23}H_{38}K_2MnN_7O_4$•DMA: C, 46.54 (46.46); H, 6.80 (6.98); N, 16.08 (15.59). FTIR (ATR, cm^{-1}):

2960, 2899, 2856, 2811, 1641, 1592, 1574, 1532, 1497, 1478, 1449, 1412, 1384, 1354, 1331, 1262, 1249, 1219, 1169, 1139, 1098, 1034, 914, 834, 778, 767, 748, 693, 617.

$K_2[Mn^{III}H_3$3$^F(O)]$. The salt was prepared using a similar procedure described above for $K_2[Mn^{III}H_3$**3**$^{Ph}(O)]$ with KH (0.0385 g, 0.960 mmol), H_6**3**^{F} (0.113 g, 0.235 mmol), $Mn^{II}(OAc)_2$ (0.0412 g, 0.238 mmol), and dry O_2 (2.6 mL, 0.12 mmol). The salt was isolated as a fine purple powder after diffusion of Et_2O into the DMA solution. The purple powder was collected on a medium porous-glass filter and washed with 20 mL of MeCN and 20 mL of Et_2O to give 0.063 g of the desired purple solid (43%). $\lambda_{max/nm}$ (DMSO, ε, M^{-1} cm^{-1}): 706, (242), 498, (443). EPR (DMF:THF, 10 K): g = 8.04 , A = 278 MHz). MS (ES+): $[C_{23}H_{37}K_2FMnN_7O_4 + 3K^+]$, 666.1; Found, 666.0. Anal. Calcd (found) for $C_{23}H_{37}FK_2MnN_7O_4$•DMA: C, 45.37 (45.25); H, 6.49 (6.71); N, 15.68 (15.70). FTIR (ATR, cm^{-1}): 2959, 2897, 2856, 1627, 1589, 1530, 1504, 1447, 1411, 1396, 1383, 1351, 1326, 1257, 1250, 1223, 1198, 1087, 1057, 1036, 1013, 912, 831, 785, 767, 681, 590.

$K_2[Mn^{III}H_3$3$^{5F}(O)]$. The salt was prepared using a similar procedure described above for $K_2[Mn^{III}H_3$**3**$^{Ph}(O)]$ with KH (0.0920 g, 2.29 mmol), H_6**3**^{5F} (0.3155 g, 0.5699 mmol), $Mn^{II}(OAc)_2$ (0.0998 g, 0.577 mmol), and dry O_2 (6.4 mL, 0.29 mmol). The salt was isolated as a green powder after diffusion of Et_2O into the DMA solution. The green precipitate was collected on a medium porous-glass filter and washed with 10 mL of MeCN and 20 mL of Et_2O to give 0.265 g (66%) of the desired green solid (66%). Single crystals of $(NMe_4)_2[Mn^{III}H_2$**3**$^{5F}(OH)]$ were obtained by adding 2 equiv of NMe_4OAc to a mixture of $K_2[Mn^{III}H_2$**3**$^{5F}(OH)]$ in MeCN, filtering through a medium porous-glass filter and allowing Et_2O to diffuse to give single crystals of the desired product. $\lambda_{max/nm}$ (DMSO, ε, M^{-1} cm^{-1}): 390 (1350), 677 (274). EPR (DMF:THF, 10 K): g = 7.97 , A = 262 MHz). Anal. Calcd (found) for $C_{23}H_{33}F_5K_2MnN_7O_4$•$0.5Et_2O$: C, 40.76 (40.52); H, 5.20 (5.53); N, 13.31 (13.27).

References

(1) Hammes, B. S.; Young, Jr., V. G.; Borovik, A. S. Hydrogen-Bonding Cavities about Metal Ions: A Redox Pair of Coordinatively Unsaturated Paramagnetic Co-OH Complexes. *Angew. Chemie Int. Ed.* **1999**, *38* (5), 666–669.

(2) MacBeth, C. E.; Gupta, R.; Mitchell-Koch, K. R.; Young, V. G.; Lushington, G. H.; Thompson, W. H.; Hendrich, M. P.; Borovik, A. S. Utilization of Hydrogen Bonds To Stabilize M−O(H) Units: Synthesis and Properties of Monomeric Iron and Manganese Complexes with Terminal Oxo and Hydroxo Ligands. *J. Am. Chem. Soc.* **2004**, *126* (8), 2556–2567.

(3) Gupta, R.; MacBeth, C. E.; Young, V. G.; Borovik, A. S. Isolation of Monomeric Mn(III/II)−OH and Mn(III)−O Complexes from Water: Evaluation of O−H Bond Dissociation Energies. *J. Am. Chem. Soc.* **2002**, *124* (7), 1136–1137.

(4) Parsell, T. H.; Yang, M.-Y.; Borovik, A. S. C−H Bond Cleavage with Reductants: Re-Investigating the Reactivity of Monomeric Mn(III/IV)−Oxo Complexes and the Role of Oxo Ligand Basicity. *J. Am. Chem. Soc.* **2009**, *131* (8), 2762–2763.

(5) Chuchani, G.; Frohlich, A. The pK a Values of Mono-Substituted Phenols and Benzenethiols and the Conjugation of Substituents Having a Strong +K Effect. *J. Chem. Soc. B Phys. Org.* **1971**, 1417.

(6) Gilli, G.; Gilli, P. *The Nature of the Hydrogen Bond*; Oxford University Press, 2009.

(7) Gilli, P.; Pretto, L.; Bertolasi, V.; Gilli, G. Predicting Hydrogen-Bond Strengths from Acid-Base Molecular Properties. the pKa Slide Rule: Toward the Solution of a Long-Lasting Problem. *Acc. Chem. Res.* **2009**, *42* (1), 33–44.

(8) Douat-Casassus, C.; Marchand-Geneste, N.; Diez, E.; Gervois, N.; Jotereau, F.; Quideau, S. Synthetic Anticancer Vaccine Candidates: Rational Design of Antigenic Peptide Mimetics That Activate Tumor-Specific T-Cells. *J. Med. Chem.* **2007**, *50* (7), 1598–1609.

(9) Lucas, R. L.; Zart, M. K.; Murkerjee, J.; Sorrell, T. N.; Powell, D. R.; Borovik, A. S. A Modular Approach toward Regulating the Secondary Coordination Sphere of Metal Ions: Differential Dioxygen Activation Assisted by Intramolecular Hydrogen Bonds. *J. Am. Chem. Soc.* **2006**, *128* (48), 15476–15489.

(10) Lucas, R. L. Development of Methods for Varying the Hydrogen Bond Network Around Metal Ions: Site-Directed Modification of the Secondary Coordination Sphere, University of Kansas, 2005.

(11) Jones, J. R.; Ziller, J. W.; Borovik, A. S. Modulating the Primary and Secondary Coordination Spheres within a Series of Co(II)-OH Complexes. *Inorg. Chem.* **2017**, *56* (3), 1112–1120.

(12) Gupta, R.; MacBeth, C. E.; Young, V. G. J.; Borovik, A. S. Isolation of Monomeric Mn(III/II)-OH and Mn(III)-O Complexes from Water: Evaluation of O-H Bond Dissociation Energies. *J. Am. Chem. Soc.* **2002**, *124* (7), 1136–1137.

(13) Shook, R. L.; Peterson, S. M.; Greaves, J.; Moore, C.; Rheingold, A. L.; Borovik, A. S. Catalytic Reduction of Dioxygen to Water with a Monomeric Manganese Complex at Room Temperature. *J. Am. Chem. Soc.* **2011**, *133* (15), 5810–5817.
(14) Shook, R. L.; Gunderson, W. A.; Greaves, J.; Ziller, J. W.; Hendrich, M. P.; Borovik, A. S. A Monomeric Mn(III)−Peroxo Complex Derived Directly from Dioxygen. *J. Am. Chem. Soc.* **2008**, *130* (28), 8888–8889.
(15) Gupta, R.; MacBeth, C. E.; Young, V. G.; Borovik, A. S. Isolation of Monomeric Mn(III/II) −OH and Mn(III)−O Complexes from Water: Evaluation of O−H Bond Dissociation Energies. *J. Am. Chem. Soc.* **2002**, *124* (7), 1136–1137.
(16) Parsell, T. H.; Behan, R. K.; Green, M. T.; Hendrich, M. P.; Borovik, A. S. Preparation and Properties of a Monomeric Mn(IV)-Oxo Complex. *J. Am. Chem. Soc.* **2006**, *128* (27), 8728–8729.
(17) Taguchi, T.; Stone, K. L.; Gupta, R.; Kaiser-Lassalle, B.; Yano, J.; Hendrich, M. P.; Borovik, A. S. Preparation and Properties of an Mn(IV)–hydroxide Complex: Proton and Electron Transfer at a Mononuclear Manganese Site and Its Relationship to the Oxygen Evolving Complex within Photosystem II. *Chem. Sci.* **2014**, *5* (8), 3064.
(18) Taguchi, T.; Gupta, R.; Lassalle-Kaiser, B.; Boyce, D. W.; Yachandra, V. K.; Tolman, W. B.; Yano, J.; Hendrich, M. P.; Borovik, A. S. Preparation and Properties of a Monomeric High-Spin Mn(V)–Oxo Complex. *J. Am. Chem. Soc.* **2012**, *134* (4), 1996–1999.
(19) Bordwell, F. G. Equilibrium Acidities in Dimethyl Sulfoxide Solution. *Acc. Chem. Res.* **1988**, *21* (12), 456–463.
(20) Gupta, R.; Borovik, A. S. Monomeric Mn(III/II) and Fe(III/II) Complexes with Terminal Hydroxo and Oxo Ligands: Probing Reactivity via O−H Bond Dissociation Energies. *J. Am. Chem. Soc.* **2003**, *125* (43), 13234–13242.
(21) Bruker AXS, I. APEX2 Version 2014.11-0. Madison, WI 2014.
(22) Bruker AXS, I. SAINT Version 8.34a. Madison, WI 2013.
(23) Sheldrick, G. M. SADABS. Bruker AXS, Inc: Madison 2014.
(24) Sheldrick, G. M. SHELXTL. Bruker AXS, Inc: Madison 2014.
(25) Wilson, A. J. C.; Geist, V. International Tables for Crystallography. Volume C: Mathematical, Physical and Chemical Tables. Kluwer Academic Publishers, Dordrecht/Boston/London 1992 (Published for the International Union of Crystallography), 883 Seiten, ISBN 0-792-3-16-38X. *Cryst. Res. Technol.* **1993**, *28* (1), 110–110.

CHAPTER 4

Mn^{IV}–O(H) and Mn^{V}=O Complexes with Urea-based Hybrid Ligands

Introduction

Metal–oxido complexes have been implicated as important intermediates for facilitating difficult chemical transformations in both synthetic and biological systems.[1–4] Some of these reactions include oxygen-atom transfer reactions and hydrogen-atom abstraction for external substrates. In addition, high-valent Mn–oxido species are suggested to play an important role in the oxidation of water to dioxygen in the oxygen-evolving complex (OEC) of Photosystem II.[5–7] The OEC is a Mn_4CaO_5 cluster that is surrounded by a network of hydrogen bonds (H-bonds), which are crucial to function. One of the key roles for the H-bond networks is to facilitate movement of protons out of the catalytic site, which is essential to the water-splitting reaction.[8]

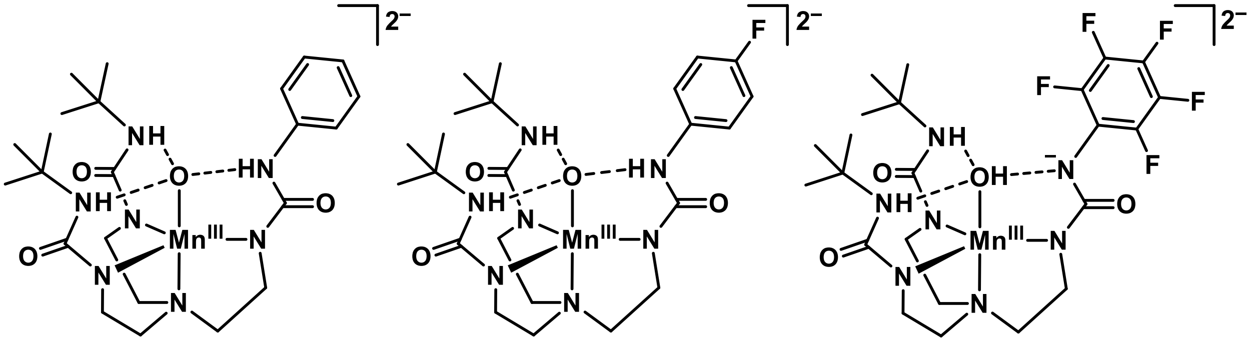

Figure 4.1. Mn^{III}–O(H) complexes reported in the previous chapter.

In the previous Chapter, a new set of hybrid tripodal ligands were described that modulate the H-bond network around Mn^{III}–O(H) complexes via changes in a single H-bond (Figure 4.1). The syntheses of a series of Mn^{III}–O(H) complexes were reported and in the complex $[Mn^{III}H_2\mathbf{3}^{5F}(OH)]^{2-}$, the proton is seen to move to the oxido ligand from a urea nitrogen to form a hydroxido ligand and a deprotonated N-atom. The movement of the proton is presumably a result of the electron withdrawing nature of the perfluorinated phenyl ring appended to the urea, which lowers the pK_a of the urea NH to such an extent that it can be deprotonated by the basic oxido ligand. It was also shown in chapter 3 that the H-bonding network plays an important role in the kinetic rates reaction of the Mn^{III}–O(H) complexes with the substrate 9,10-dihydroanthracene (DHA). The complexes with the more electron withdrawing substituents attached to the urea were shown to react slower with DHA.

Our group has been able to characterize the $Mn^{III/IV/V}$–O and $Mn^{II/III/IV}$–OH complexes with the tripodal urea based ligand $[H_3buea]^{3-}$ (Scheme 4.1).[9–13] The spectroscopic features of these complexes are known and are used as references to study the oxidation reactions with the Mn^{III}–O(H) complexes presented in Chapter 3. In this Chapter, the oxidation chemistry of $[Mn^{III}H_3\mathbf{3}^{Ph}(O)]^{2-}$ and $[Mn^{III}H_2\mathbf{3}^{5F}(OH)]^{2-}$ will be explored. New Mn^{IV} and Mn^{V}

Scheme 4.1. Series of Previously Reported Mn-O(H) Complexes with $[H_3buea]^{3-}$

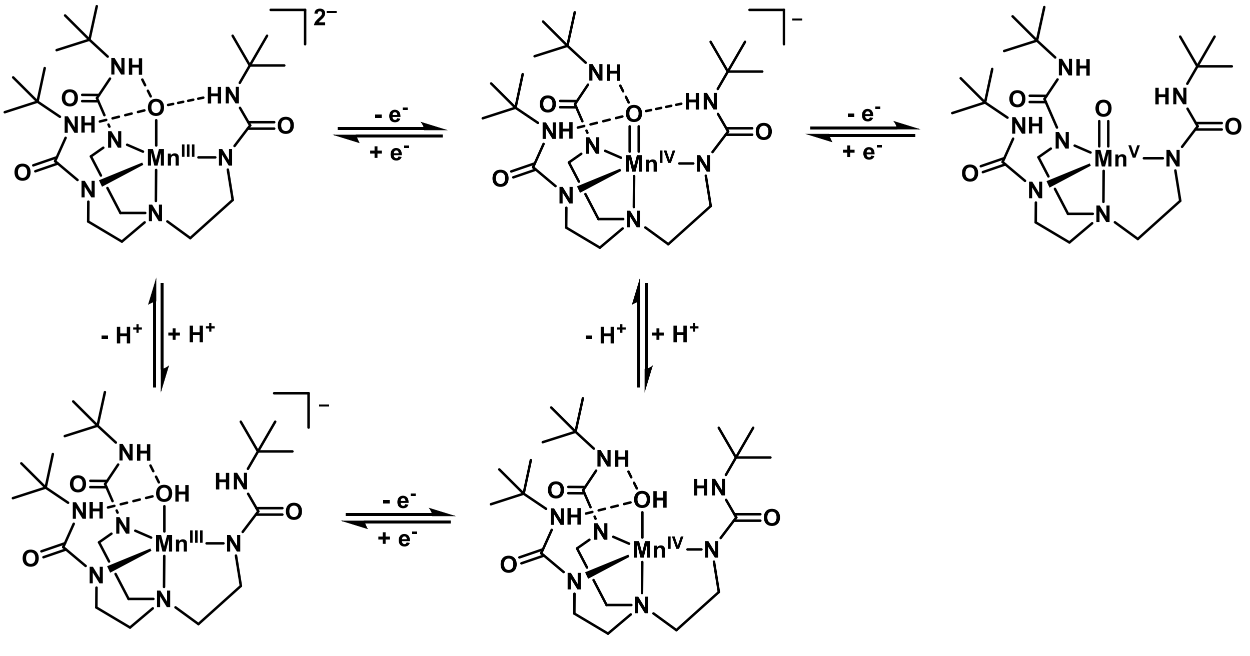

complexes with the $[H_3\mathbf{3}^{Ph}]^{3-}$ and $[H_2\mathbf{3}^{5F}]^{4-}$ ligands are prepared and their reactions with protons will be investigated. Possible intramolecular proton transfer between a H-bond donor/accepter upon oxidation of $[Mn^{III}H_2\mathbf{3}^{5F}(OH)]^{2-}$ is discussed.

Results and Discussion

Oxidation of $[Mn^{III}H_3\mathbf{3}^{Ph}(O)]^{2-}$ at Low Temperatures. The complex $[Mn^{III}H_3\mathbf{3}^{Ph}(O)]^{2-}$ was reported in the previous chapter and its Mn^{IV}/Mn^{III} redox couple was found to be – 0.84 V vs. $[FeCp_2]^{+/0}$. Consistent with this measurement, treatment of $[Mn^{III}H_3\mathbf{3}^{Ph}(O)]^{2-}$ with one equivalent (equiv) of $[FeCp_2]^+$ at – 80 °C in a dimethylformamide:tetrahydrofuran (DMF:THF) mixture produced a new species that has been assigned as $[Mn^{IV}H_3\mathbf{3}^{Ph}(O)]^-$ (Figure 4.2 and Table 4.1). Spectrophotometric monitoring of the reaction showed loss of the characteristic bands of $[Mn^{III}H_3\mathbf{3}^{Ph}(O)]^{2-}$ at λ_{max}/nm = 710 and 498 and new bands for $[Mn^{IV}H_3\mathbf{3}^{Ph}(O)]^{2-}$ at λ_{max}/nm (ε/M^{-1} cm^{-1}) = 432 (3500) and 700 (500) (Figure 4.2A) that persist at – 80 °C. These features are similar to the absorbance peaks for $[Mn^{IV}H_3buea(O)]^-$ that are observed at λ_{max}/nm = 420 and 635, however, the lower energy band for $[Mn^{IV}H_3\mathbf{3}^{Ph}(O)]^-$ appears as a shoulder and not a well-defined absorbance band like in $[Mn^{IV}H_3buea(O)]^-$.[11,14]

Monitoring this reaction using perpendicular-mode electron paramagnetic resonance (EPR) spectroscopy showed the growth of a new signals at g = 5.52, 5.33, 2.27, 1.76, and 1.34 consistent with a high-spin S=3/2 Mn^{IV} center (Figure 4.2B and Table 4.1). There are two sets of a six-line hyperfine patterns, centered at g = 5.33 (A = 183 MHz) and 5.52 (A = 216 MHz). The measured E/D value for the complex is 0.29, which suggests a slightly more rhombic coordination environment than $[Mn^{IV}H_3buea(O)]^-$, which has an experimentally determined E/D value of 0.26.[14] Both Mn^{IV} species have highly rhombic EPR spectra, which is due to the Jahn-Teller effect of the Mn^{IV} ion in a trigonal field, leading to a distortion of the geometry. The slightly more rhombic coordination environment in $[Mn^{IV}H_3\mathbf{3}^{Ph}(O)]^-$ could be due to an asymmetry in the H-bonding network supporting the oxo ligand. The phenyl urea NH is expected to form a stronger H-bond with the oxido ligand than the other two H-bond donors, which could distort the coordination environment in the trigonal plane. However, H-bonds to an oxido ligand are expected to decrease with increasing oxidation state of the Mn center because the oxido ligand becomes more electrophilic with increasing oxidation state, so the reason for the more rhombic EPR spectrum is not clear.

Table 4.1. Selected Properties of Mn^{IV} Species

	λ_{max} (nm), (ε, M^{-1} cm^{-1})	g, (E/D)	A, MHz
$[Mn^{IV}H_3buea(O)]^{-\,a}$	420	5.15 (0.26)	190
$[Mn^{IV}H_3buea(OH)]^{\,a}$	466 (5700)	5.43, 5.56, 5.01, 5.84 (0.31), (0.17)	190, 210, 210, 210
$[Mn^{IV}H_3\mathbf{3}^{Ph}(O)]^-$	432 (3500)	5.32, 5.52, (0.29)	183, 216
$[Mn^{IV}H_2\mathbf{3}^{5F}(O)(H)]^-$	411 (3100)	5.13, 5.67, (0.23)	189, 221

[a] Data obtained from ref 14–16. $[Mn^{IV}H_3buea(OH)]$ has two E/D values since there are two species.

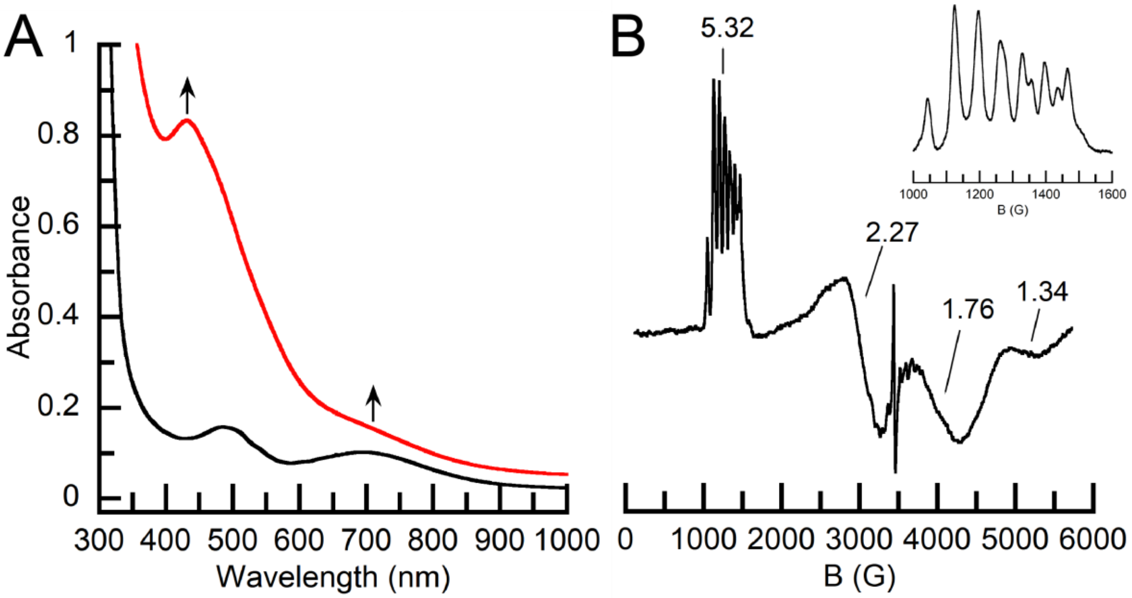

Figure 4.2. (A) Absorbance spectra and of the oxidation of $[Mn^{III}H_3\mathbf{3}^{Ph}(O)]^{2-}$ (black line) with $[FeCp_2]^{+/0}$ to $[Mn^{IV}H_3\mathbf{3}^{Ph}(O)]^-$ (red line) recorded in DMF:THF at – 80 °C. (B) X-band EPR spectrum of $[Mn^{IV}H_3\mathbf{3}^{Ph}(O)]^-$ measured at 10 K; reaction was conducted in DMF:THF at – 80 °C. Inset: Enlargement of the g = 5 region. The multi-line hyperfine signal near g = 2 is attributed to a minor impurity from a mixed valent dinuclear Mn species

Treatment of $[Mn^{IV}H_3\mathbf{3}^{Ph}(O)]^-$ with one equiv of the acid $[PhNH_3]^+$ resulted in loss of absorbance features at λ_{max}/nm = 432 and 700 nm and growth of a new absorbance band at λ_{max}/nm (ε/M^{-1} cm^{-1}) = 485 (3700) (Figure 4.3A). The new species was assigned as $[Mn^{IV}H_3\mathbf{3}^{Ph}(OH)]$. The absorbance band attributed to the $[Mn^{IV}H_3\mathbf{3}^{Ph}(OH)]$ is slightly red shifted relative to the band at λ_{max}/nm = 466 for $[Mn^{IV}H_3buea(OH)]$.[16] Monitoring the protonation reaction by perpendicular-mode EPR spectroscopy corroborated the generation of a Mn^{IV} species. The spectrum showed growth of new features centered around g = 5.49, 5.38, 3.01, and 1.45 corresponding to a S = 3/2 Mn^{IV} center (Figure 4.3B). There are two sets of a six-line hyperfine patterns centered around g = 5.38 (A = 188 MHz) and 5.49 (A = 210 MHz). The hyperfine splitting for the Mn^{IV}–OH species is nearly identical to the 190 and 210 MHz observed for $[Mn^{IV}H_3buea(OH)]$.[16]

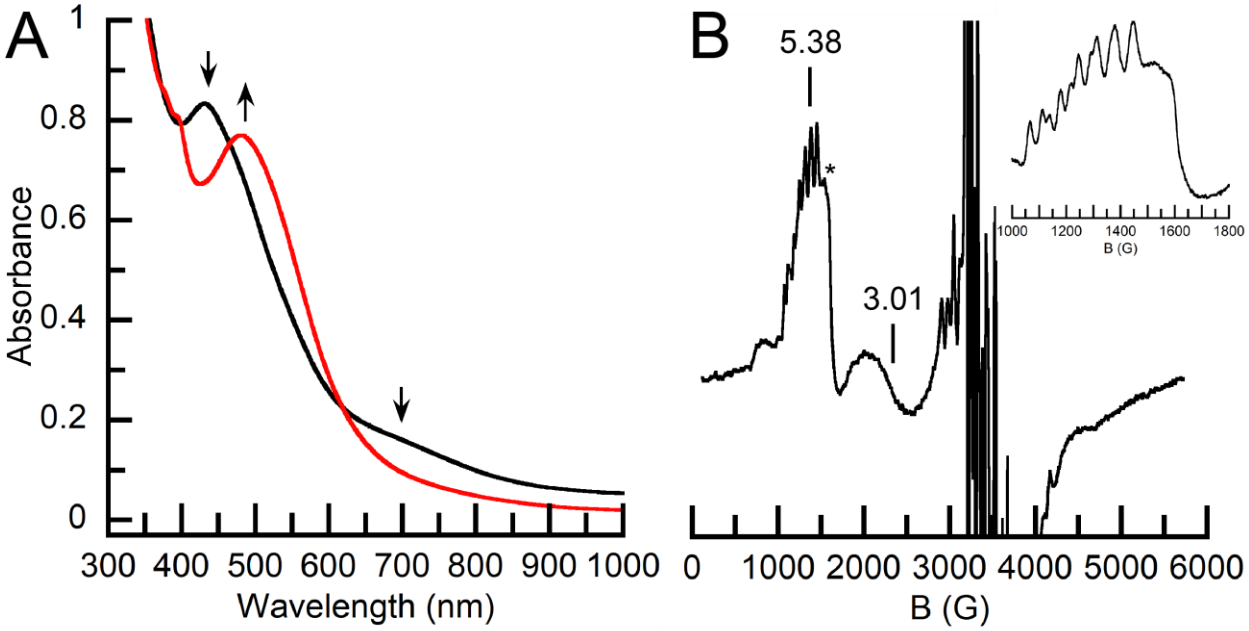

Figure 4.3. (A) Electronic absorbance spectra and (B) X-band EPR spectrum of the reaction of $[Mn^{IV}H_3\mathbf{3}^{Ph}(O)]^-$ with $[PhNH_3]^+$ in DMF:THF at – 80 °C. $[FeCp_2]^+$ is indicated in the figure with a *. Inset: Enlargement of the g = 5 region. The multi-line hyperfine signal near g = 2 is attributed to a minor impurity from a mixed valent dinuclear Mn species

The $[Mn^{III}H_3\mathbf{3}^{Ph}(O)]^{2-}$ complex can be further oxidized with a subsequent equiv of $[FeCp_2]^+$ in a DMF:THF solution at – 80 °C. The doubly oxidized Mn^{III}–O compound produces a new species that has been assigned as $[Mn^{V}H_3\mathbf{3}^{Ph}(O)]$. Spectrophotometric monitoring of the reaction shows loss of the characteristic bands for $[Mn^{III}H_3\mathbf{3}^{Ph}(O)]^{2-}$ and growth of new absorbance features at λ_{max}/nm = 425, 618, and 854 (Figure 4.4A). Extinction coefficients were not calculated for $[Mn^{V}H_3\mathbf{3}^{Ph}(O)]$ because of the instability even at – 80˚C. These new absorbance features are comparable to those observed for the previously characterized $[Mn^{V}H_3buea(O)]$ complex (λ_{max}/nm = 430, 620, and 820).[11] The resulting Mn^{V}=O complex is unstable and reacts within minutes at – 80 °C to form a new species with an absorbance feature at λ_{max}/nm = 485, matching that of $[Mn^{IV}H_3\mathbf{3}^{Ph}(OH)]$. This reaction could occur by $[Mn^{V}H_3\mathbf{3}^{Ph}(O)]$ abstracting a H-atom from solvent to form $[Mn^{IV}H_3\mathbf{3}^{Ph}(OH)]$. Monitoring the decay of the Mn^{V} species shows a half-life of 250 seconds (Figure 4.4B and Figure 4.5). The half-life of the hybrid species is significantly shorter than that of the symmetrical $[Mn^{V}H_3buea(O)]$, which was reported to be stable for hours at – 80 °C. One possible cause for the increased reactivity of $[Mn^{V}H_3\mathbf{3}^{Ph}(O)]$ could arise from the ligand $[H_3\mathbf{3}^{Ph}]^{3-}$ providing less steric protection than $[H_3buea]^{3-}$, leaving the Mn^{V}=O unit more exposed.

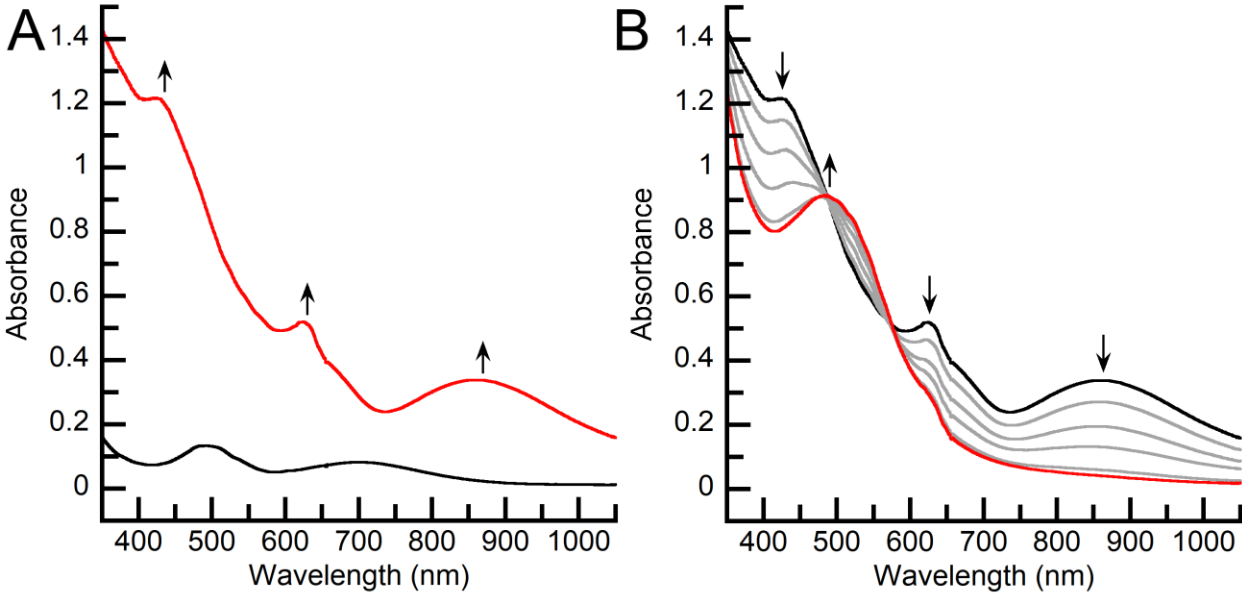

Figure 4.4. (A) Electronic absorbance spectra for the reaction of $[Mn^{III}H_3\mathbf{3}^{Ph}(O)]^{2-}$ with 2 equiv of $[FeCp_2]^+$ and (B) decay of the Mn^V species. Spectra recorded in a DMF:THF at – 80 °C.

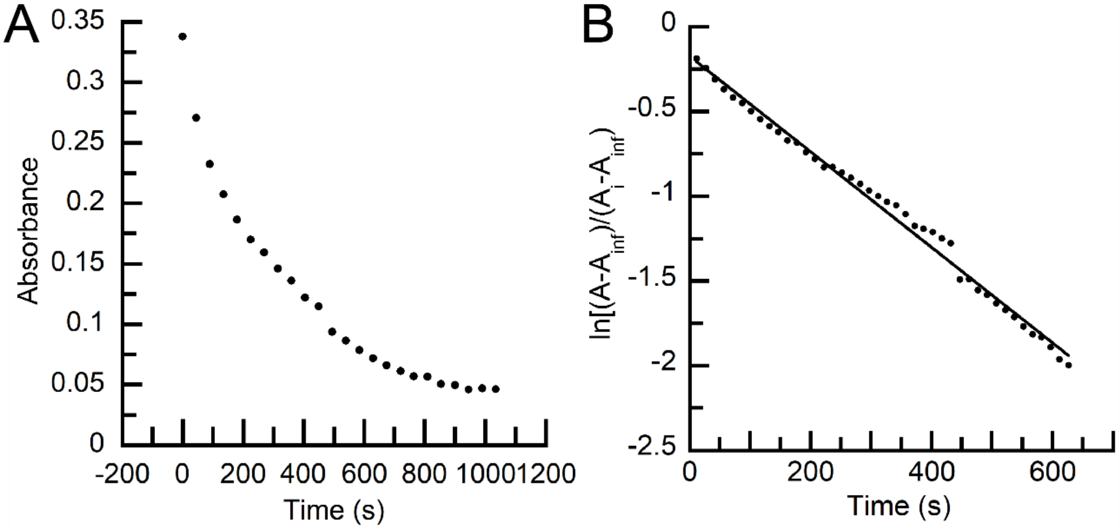

Figure 4.5. (A) Decay of the 854 nm absorbance band of $[Mn^{V}H_3\mathbf{3}^{Ph}(O)]$ in DMF:THF at – 80 °C and (B) first-order fit used to calculate the half-life.

Monitoring the reaction using EPR spectroscopy showed loss of the signal corresponding to $[Mn^{III}H_3\mathbf{3}^{Ph}(O)]^{2-}$, but no further signals were generated in parallel mode. An S = 1 signal is observed for $[Mn^{V}H_3buea(O)]$, however S = 1 signals are often difficult to observe in parallel mode EPR spectroscopy. In addition, the limited stability of the

$[\mathrm{Mn^{V}H_3}\mathbf{3}^{\mathrm{Ph}}(\mathrm{O})]$ would make observing this signal difficult because the $\mathrm{Mn^{V}}$ species decomposes quickly upon generation at – 80 °C. However, the perpendicular mode EPR spectra showed growth of a species with a spectrum matching $[\mathrm{Mn^{IV}H_3}\mathbf{3}^{\mathrm{Ph}}(\mathrm{OH})]$ (Figure 4.6).

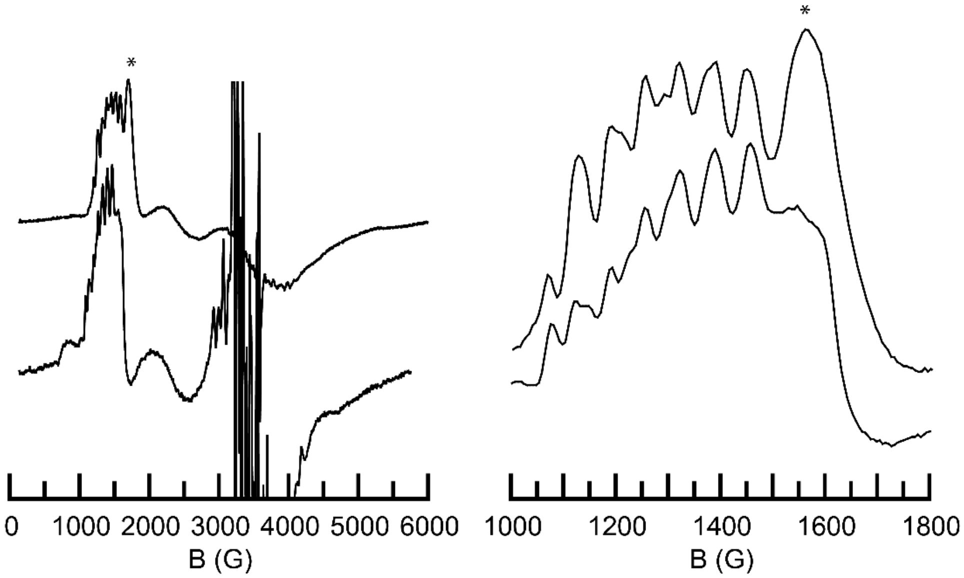

Figure 4.6. (A) Full X-band EPR spectra and (B) zoom of g = 5 region of the reaction of $[\mathrm{Mn^{IV}H_3}\mathbf{3}^{\mathrm{Ph}}(\mathrm{O})]^{-}$ with $[\mathrm{PhNH_3}]^{+}$ (bottom) and the reaction of $[\mathrm{Mn^{III}H_3}\mathbf{3}^{\mathrm{Ph}}(\mathrm{O})]^{2-}$ with 2 equiv $[\mathrm{FeCp_2}]^{+}$ (top) in DMF:THF at – 80 °C. $[\mathrm{FeCp_2}]^{+}$ is indicated in the figure with a *. The multi-line hyperfine signal near g = 2 is attributed to a minor impurity from a mixed valent dinuclear Mn species

Oxidation of $[\mathrm{Mn^{III}H_2}\mathbf{3}^{\mathrm{5F}}(\mathrm{OH})]^{2-}$ at Low Temperatures. The starting complex $[\mathrm{Mn^{III}H_2}\mathbf{3}^{\mathrm{5F}}(\mathrm{OH})]^{2-}$ was reported in the previous chapter. It should be reiterated that this complex is a $\mathrm{Mn^{III}}$–OH species and contains a different H-bonding network than $[\mathrm{Mn^{III}H_3}\mathbf{3}^{\mathrm{Ph}}(\mathrm{O})]^{2-}$. Two of the intramolecular H-bonds are derived from the *tert*-butyl urea NH to the hydroxido ligand and the third comes from the hydroxido ligand to the deprotonated perfluorinated phenyl urea nitrogen. Due to this difference in the H-bonding network, the ligand has a basic site that can allow for movement of a proton within the ligand cavity. Treatment of $[\mathrm{Mn^{III}H_2}\mathbf{3}^{\mathrm{5F}}(\mathrm{OH})]^{2-}$ with one equiv of $[\mathrm{FeCp_2}]^{+}$ produces a new species that has been assigned as $[\mathrm{Mn^{IV}H_2}\mathbf{3}^{\mathrm{5F}}(\mathrm{O})(\mathrm{H})]^{-}$ (Figure 4.7A and Figure 4.8). The location of the proton within the complex is not yet known. Spectrophotometric monitoring of this reaction shows loss of the characteristic bands for $[Mn^{III}H_2\mathbf{3}^{5F}(OH)]^{2-}$ at λ_{max}/nm = 677 and growth of new absorbance bands at λ_{max}/nm (ε/M^{-1} cm^{-1}) = 411 (3100) and 650 (580) nm (Figure 4.7A). The absorbance bands associated with the new Mn^{IV} species are comparable to what is observed for $[Mn^{IV}H_3\mathbf{3}^{Ph}(O)]^-$ and $[Mn^{IV}H_3buea(O)]^-$. If the compound is more like a Mn^{IV}–oxido species that would suggest the proton is localized in the urea N atom rather than the exogenous O ligand. The high-energy band at 411 nm in $[Mn^{IV}H_2\mathbf{3}^{5F}(O)(H)]^-$ is shifted to slightly higher energy than the 432 nm that is observed for $[Mn^{IV}H_3\mathbf{3}^{Ph}(O)]^-$ (Figure 4.8). Similar to $[Mn^{IV}H_3\mathbf{3}^{Ph}(O)]^-$ a broad shoulder at near 650 nm is observed rather than the more defined absorbance band observed in $[Mn^{IV}H_3buea(O)]^-$.

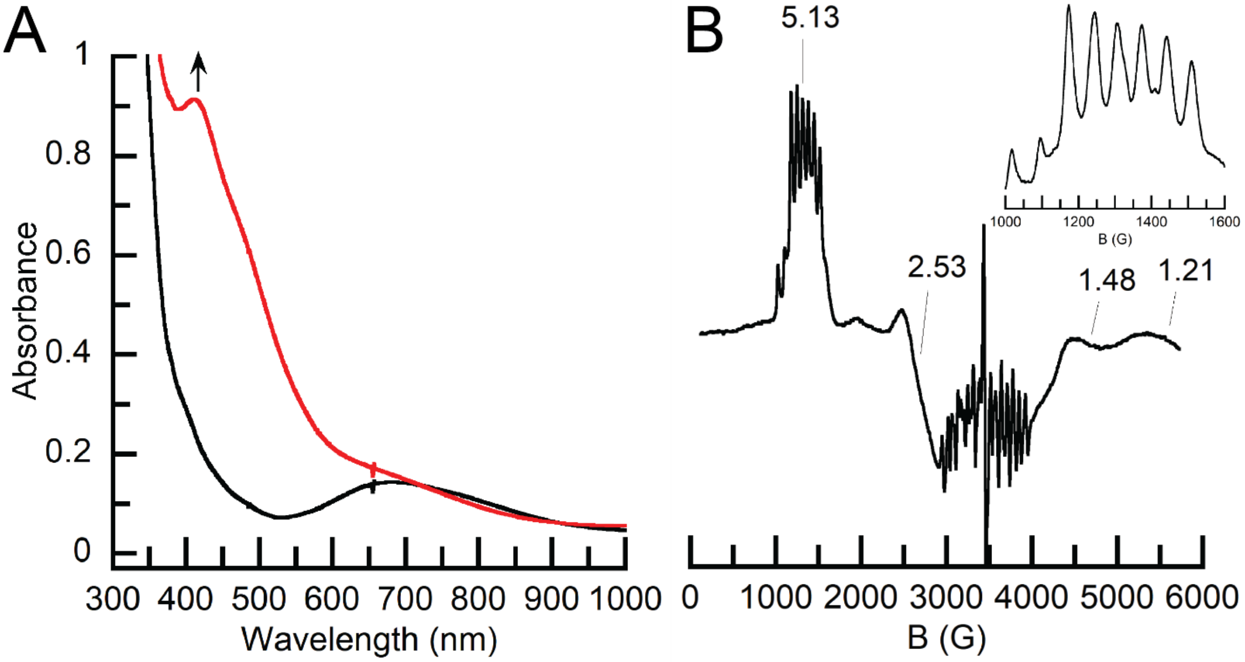

Figure 4.7. (A) Absorbance spectra of the oxidation of $[Mn^{III}H_2\mathbf{3}^{5F}(OH)]^{2-}$ (black line) with $[FeCp_2]^+$ to $[Mn^{IV}H_2\mathbf{3}^{5F}(O)(H)]^-$ (red line) and (B) X-band EPR spectrum of $[Mn^{IV}H_2\mathbf{3}^{5F}(O)(H)]^-$ measured at 10 K; Both reactions were conducted in DMF:THF at – 80 °C. Inset: Enlargement of the g = 5 region.

Monitoring this reaction using EPR spectroscopy showed loss of the signal associated with $[Mn^{III}H_2\mathbf{3}^{5F}(OH)]^{2-}$ and growth of a new perpendicular mode signal centered at g = 5.67, 5.13, 2.53, 1.48, and 1.21, which is characteristic of a S = 3/2 species (Figure 4.7B). There are two sets of a six-line hyperfine patterns, centered at g = 5.13 (A = 189 MHz) and, 5.67 (A = 221 MHz). The hyperfine constant is consistent with a Mn^{IV} species, and is slightly higher than the 183 and 216 MHz that is observed for $[Mn^{IV}H_3\mathbf{3}^{Ph}(O)]^-$. The E/D value for the complex is 0.23, which suggests that the coordination environment is slightly more symmetrical compared to $[Mn^{IV}H_3buea(O)]^-$ and $[Mn^{IV}H_3\mathbf{3}^{Ph}(O)]^-$, which have E/D values of 0.26 and 0.29, respectively.

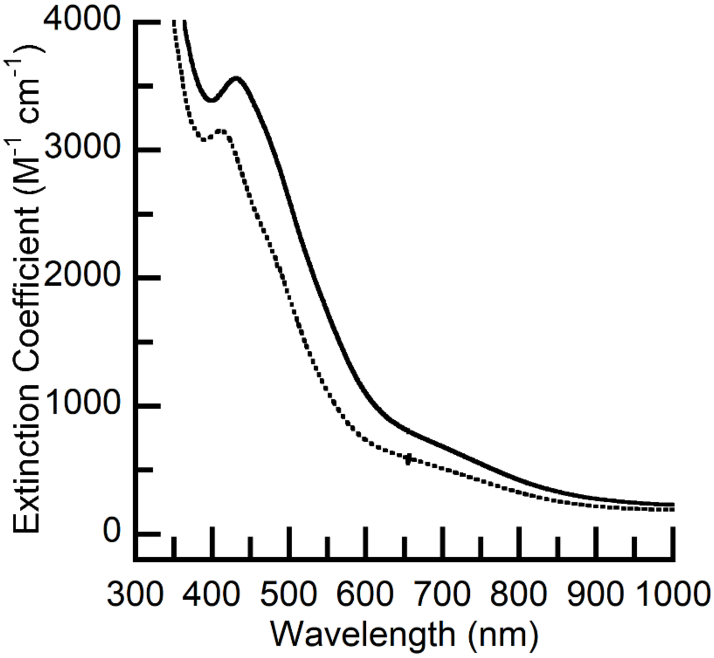

Figure 4.8. Electronic absorbance spectra of $[Mn^{IV}H_3\mathbf{3}^{Ph}(O)]^-$ (black line) and $[Mn^{IV}H_2\mathbf{3}^{5F}(O)(H)]^-$ (dashed line) recorded in DMF:THF at – 80 °C.

The Mn^{IV} species was treated with one equiv of the acid $[PhNH_3]^+$ to generate a new species with absorbance features at λ_{max}/nm (ε/M^{-1} cm^{-1}) = 464 (2700) (Figure 4.9A). These features are comparable to what is observed for $[Mn^{IV}H_3buea(OH)]$ (λ_{max}/nm = 466 nm) and $[Mn^{IV}H_3\mathbf{3}^{Ph}(OH)]$ (λ_{max}/nm = 485 nm), suggesting a formulation of $[Mn^{IV}H_3\mathbf{3}^{5F}(OH)]$. Monitoring this reaction using EPR spectroscopy showed growth of a new perpendicular mode signal centered at g = 5.50, 5.38 and 1.45 (Figure 4.9B). There are two sets of a six-line hyperfine patterns, centered at g = 5.38 (A = 188 MHz) and, 5.50 (A = 208 MHz). The signals and hyperfine constants are similar to what is observed for $[\mathrm{Mn^{IV}H_3}\mathbf{3}^{\mathrm{Ph}}(\mathrm{OH})]^-$ (g = 5.38 (A = 188 MHz) and 5.49 (A = 210 MHz)).

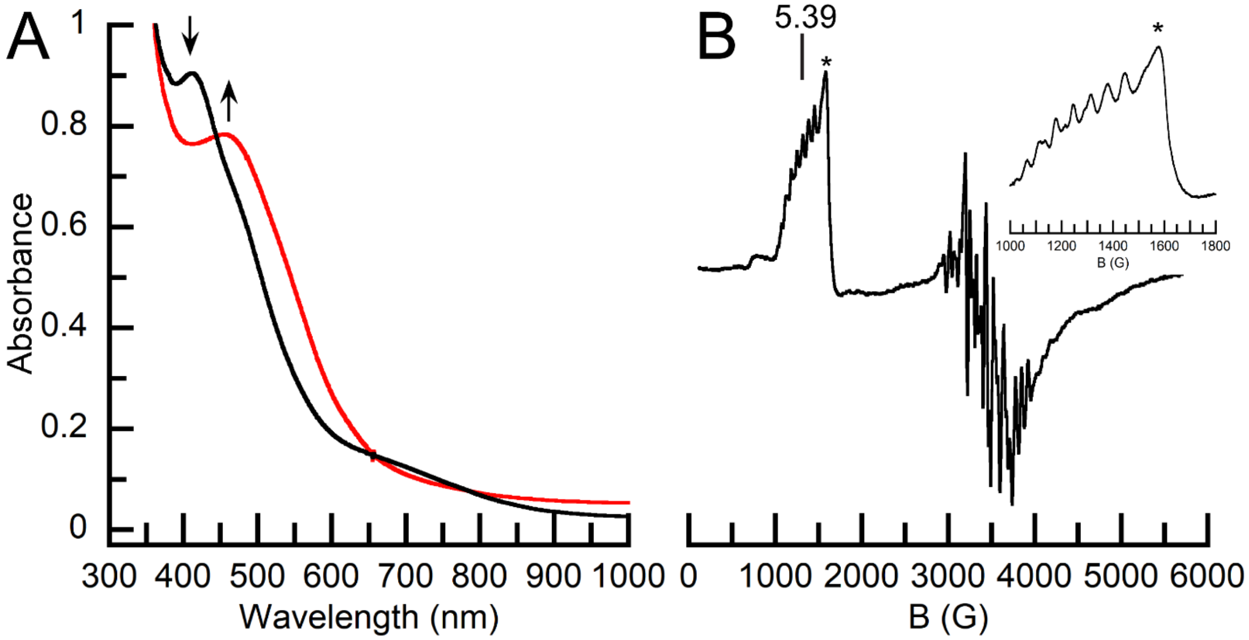

Figure 4.9. (A) Electronic absorbance spectra of the reaction of $[\mathrm{Mn^{IV}H_2}\mathbf{3}^{\mathrm{5F}}(\mathrm{O})(\mathrm{H})]^-$ with $[\mathrm{PhNH_3}]^+$ recorded at – 80 °C and (B) EPR spectrum of the reaction of $[\mathrm{Mn^{IV}H_2}\mathbf{3}^{\mathrm{5F}}(\mathrm{O})(\mathrm{H})]^-$ with $[\mathrm{PhNH_3}]^+$ recorded at 10K. Both reactions conducted in DMF:THF mixture at – 80 °C. Inset: Enlargement of the g = 5 region.

$[\mathrm{Mn^{IV}H_2}\mathbf{3}^{\mathrm{5F}}(\mathrm{O})(\mathrm{H})]^-$ does not react further with additional equivalents of $[\mathrm{FeCp_2}]^+$, which suggests that the electrochemical properties have changed relative to $[\mathrm{Mn^{IV}H_3}\mathbf{3}^{\mathrm{Ph}}(\mathrm{O})]^-$ and $[\mathrm{Mn^{IV}H_3buea(O)}]^-$. The change in redox properties could be attributed to the stronger H-bond that forms from the perfluorinated phenyl urea, which reduces the amount of donation to the $\mathrm{Mn^{IV}}$ center from the oxido or hydroxido ligand. The donor ability of the coordinated nitrogen of the perfluorinated phenyl urea could also be diminished from the electron withdrawing groups. Additionally, this could arise from the fifth ligand being a hydroxido and not an oxido causing a positive shift in the $\mathrm{Mn^{V/IV}}$ redox potentials compared to $[\mathrm{Mn^{IV}H_3buea(O)}]^-$ and $[\mathrm{Mn^{IV}H_3}\mathbf{3}^{\mathrm{Ph}}(\mathrm{O})]^-$. For the oxidation of $[\mathrm{Mn^{IV}H_2}\mathbf{3}^{\mathrm{5F}}(\mathrm{O})(\mathrm{H})]^-$ methylene chloride (CH_2Cl_2) and THF were used to allow for the use of stronger oxidants than $[FeCp_2]^+$. $K_2[Mn^{III}H_2\mathbf{3}^{5F}(OH)]$ was dissolved in THF by adding 18-crown-6 and was reacted with two equiv of $[FeCp(C_5H_4COMe)]^+$ ($[AcFeCp_2]^+$) in CH_2Cl_2. Spectrophotometric monitoring of the reaction revealed growth of new absorbance bands at λ_{max}/nm (ε/M^{-1} cm^{-1}) = 425 (5800), 634 (3000), and 812 (2100) (Figure 4.10 and Table 4.2) that is stable at – 80 °C. These absorbance bands are comparable to the observed features for $[Mn^VH_3buea(O)]$ (λ_{max}/nm = 430, 620, and 820) and $[Mn^VH_3\mathbf{3}^{Ph}(O)]$ (λ_{max}/nm = 425, 618, and 854), suggesting the possible formulation of the product as $[Mn^VH_3\mathbf{3}^{5F}(O)]$. The similarity in electronic absorbance spectra suggest that the proton could have moved from the oxygen atom to the perfluorinated phenyl urea nitrogen. Proton movement with changing oxidation state is not surprising due to the decreased pK_a of a bound hydroxido or aquo ligand with increased oxidation state of the metal center.[17] These preliminary results, showing possible intramolecular proton movement in $[Mn^VH_3\mathbf{3}^{5F}(O)]$ illustrates how H-bond donors and acceptors can facilitate movement of protons without the assistance of solvent, which is similar to what is seen in active sites of enzymes.

Table 4.2. Electronic Properties of Mn^V Complexes

	λ_{max} (nm), (ε, M^{-1} cm^{-1})
$[Mn^VH_3buea(O)]$ [a]	430 (10000), 620 (3400), 820 (3600)
$[Mn^VH_3\mathbf{3}^{Ph}(O)]$ [b]	425, 618, and 854
$[Mn^VH_3\mathbf{3}^{5F}(O)]$ [c]	425 (5800), 634 (3000), 812 (2100)

[a] recorded in DMF:THF at – 80 °C from ref [11]; [b] recorded in DMF:THF at – 80 °C, extinction coefficients are not reported due to instability; [c] recorded in CH_2Cl_2:THF at – 80 °C.

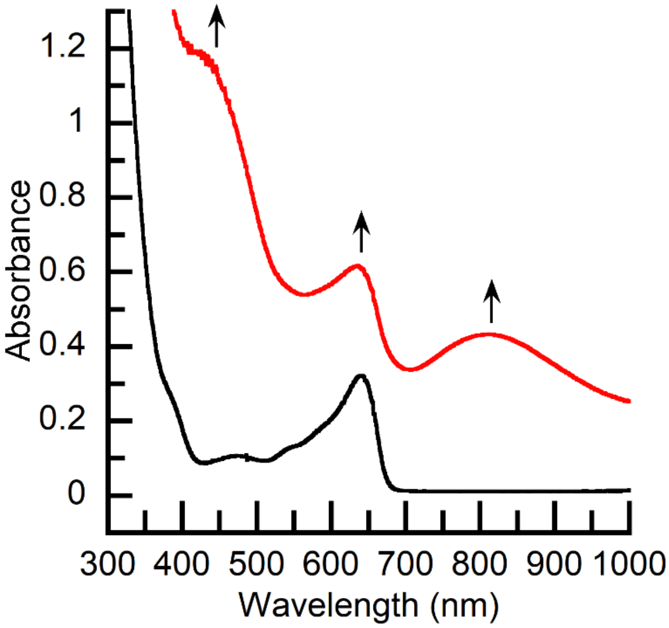

Figure 4.10. Electronic absorbance spectra of the reaction of $[\mathrm{Mn^{III}H_2}\mathbf{3}^{5F}(\mathrm{OH})]^{2-}$ with $[\mathrm{AcFeCp_2}]^+$ measured in $\mathrm{CH_2Cl_2}$:THF at – 80 °C.

Summary and Conclusion

The new hybrid urea based tripodal ligands are capable of moving protons within the ligand cavity. Using the ligands $[\mathrm{H_3}\mathbf{3}^{Ph}]^{3-}$ and $[\mathrm{H_2}\mathbf{3}^{5F}]^{4-}$, it has been demonstrated that $\mathrm{Mn^{IV}}$ and $\mathrm{Mn^{V}}$ complexes can be generated. $[\mathrm{Mn^{V}H_3}\mathbf{3}^{Ph}(\mathrm{O})]$ is significantly less stable in solution compared to $[\mathrm{Mn^{V}H_3buea(O)}]$, which could arise from less steric protection provided by $[\mathrm{H_3}\mathbf{3}^{Ph}]^{3-}$ than $[\mathrm{H_3buea}]^{3-}$ or the different H-bonding environments provided by the two ligands. While the reactivity of the Mn complexes with $[\mathrm{H_3}\mathbf{3}^{Ph}]^{3-}$ are different than the analogous complexes with $[\mathrm{H_3buea}]^{3-}$, their spectroscopic features support the assignment of them to be a Mn–oxido in the +3, +4, and +5 oxidation states of Mn. However, the assignment of Mn–oxido or Mn–hydroxido is less clear in complexes with the $[\mathrm{H_2}\mathbf{3}^{5F}]^{4-}$ ligand, which only $\mathrm{Mn^{III}}$ oxidation state has a clear assignment of the location of the proton within the metal complex. In the $\mathrm{Mn^{III}}$ state the ligand is a hydroxido, the $\mathrm{Mn^{IV}}$ state is unclear the position of the proton, and finally in Mn^{V} the complex preliminary results suggest the complex could be a Mn^{V}=O species, but further studies are needed to confirm this.

$[Mn^{IV}H_3\mathbf{3}^{Ph}(O)]^-$ and $[Mn^{IV}H_2\mathbf{3}^{5F}(O)(H)]^-$ can be treated with acids to generate the corresponding Mn^{IV}–OH complexes with similar spectroscopic features to that of $[Mn^{IV}H_3buea(OH)]$. Knowing the spectroscopic features of all the analogous complexes with $[H_3buea]^{3-}$ provides a powerful tool for studying the identity of new complexes with tripodal urea ligands. Vibrational studies are still needed to determine the identity of the new Mn^{IV} and Mn^{V} complexes. Other variants of the ligand with different electron withdrawing or donating character appended to the phenyl attached to the urea are needed to complete this series of complexes and may lead to more discrete species with defined spectroscopic and structural properties.

Experimental Section

General Procedures. All manipulations, unless otherwise stated, were performed under an argon atmosphere in a Vac-atmospheres dry box. $[Mn^{III}H_3\mathbf{3}^{Ph}(O)]^{2-}$ and $[Mn^{III}H_2\mathbf{3}^{5F}(OH)]^{2-}$ were prepared according to the procedures in chapter 3. All chemicals were purchased from commercial sources and used without further purification unless otherwise stated. $FeCp_2BF_4$ and $AcFcBF_4$ were prepared according to published procedures.[18]

Physical Methods. Electronic absorption spectra were recorded in a 1 cm cuvette on an 8453 Agilent UV-Vis spectrometer equipped with an Unisoku Unispeks cryostat. Electronic paramagnetic resonance (EPR) spectra were recorded using a Bruker EMX spectrometer equipped with an ER041XG microwave bridge, an Oxford Instrument liquid-helium quartz cryostat, and a dual mode cavity (ER4116DM).

Oxidation of $[Mn^{III}H_3\mathbf{3}^{Ph}(O)]^{2-}$ at Low Temperature using UV-vis Spectroscopy. A stock solution of $[Mn^{III}H_3\mathbf{3}^{Ph}(O)]^{2-}$ at 8.9 mM (6.5 mg, 0.011 mmol) was prepared in a DMF:THF solution (1.2 mL). In a typical experiment, 3 mL of DMF:THF was loaded into the cuvette, sealed with a rubber septum and cooled to – 80 °C for 20 minutes. To the cuvette, 70 μL of Mn^{III} solution was transferred to generate a 0.21 mM solution of $[Mn^{III}H_3\mathbf{3}^{Ph}(O)]^{2-}$. A stock solution of $FeCp_2BF_4$ at 19 mM (5.2 mg, 0.019 mmol) was prepared in a DMF:THF solution (1 mL). To the $[Mn^{III}H_3\mathbf{3}^{Ph}(O)]^{2-}$ solution, either one or two equiv of $FeCp_2BF_4$ was added via gas-tight syringe. The reactions were monitored spectrophotometrically until no further changes to the UV-vis spectrum were observed.

Oxidation of $[Mn^{III}H_3\mathbf{3}^{Ph}(O)]^{2-}$ at Low Temperature using EPR Spectroscopy. A stock solution of $[Mn^{III}H_3\mathbf{3}^{Ph}(O)]^{2-}$ at 10 mM (6.2 mg, 0.010 mmol) was prepared in a DMF:THF solution (1 mL). In a typical experiment, 250 μL of this Mn^{III} solution was injected into an EPR tube, sealed with a rubber septum, and cooled to – 78 °C using a dry-ice/acetone bath for 20 minutes. A stock solution of $FeCp_2BF_4$ at 68 mM (18.5 mg, 0.0678 mmol) was prepared in a DMF:THF solution (1 mL). To the pre-cooled $[Mn^{III}H_3\mathbf{3}^{Ph}(O)]^{2-}$ solution, one or two equiv of $FeCp_2BF_4$ was added via gas-tight syringe. The EPR tube was shaken to mix the two reactants and the solution was frozen by placing the EPR tube in liquid N_2.

Oxidation of $[Mn^{III}H_2\mathbf{3}^{5F}(OH)]^{2-}$ to $[Mn^{IV}H_2\mathbf{3}^{5F}(O)(H)]^{-}$ using UV-vis Spectroscopy. This reaction was done using the same procedure described above for the oxidation of $[Mn^{III}H_3\mathbf{3}^{Ph}(O)]^{2-}$ using UV-vis spectroscopy. 70 μL of 14mM $[Mn^{III}H_2\mathbf{3}^{5F}(OH)]^{2-}$ (9.7 mg, 0.014 mmol, 1 mL DMF) into 4 mL of DMF:THF solution in the cuvette, 55 μL of 21 mM $FeCp_2BF_4$ (5.6 mg, 0.021 mmol, 1 mL DMF:THF).

Oxidation of $[\mathrm{Mn^{III}H_3}\mathbf{3}^{5F}(\mathrm{O})]^{2-}$ to $[\mathrm{Mn^{V}H_3}\mathbf{3}^{5F}(\mathrm{O})]$ using UV-vis Spectroscopy. A stock solution of $[\mathrm{Mn^{III}H_2}\mathbf{3}^{5F}(\mathrm{OH})]^{2-}$ at 8.7 mM (6.1 mg, 8.7 mmol) was prepared in a THF solution (1 mL) with 18-crown-6 (9.1 mg, 34 mmol). In a typical experiment, 3 mL of $\mathrm{CH_2Cl_2}$ solution was loaded into a cuvette, sealed with a rubber septum, and cooled to – 80 °C for 20 minutes. A stock solution of $\mathrm{AcFcBF_4}$ at 13 mM (4.2 mg, 0.013 mmol) was prepared in a $\mathrm{CH_2Cl_2}$ solution (1 mL). To the cuvette, 90 µL of $\mathrm{AcFcBF_4}$ was added to generate a 0.39 mM solution of $\mathrm{AcFcBF_4}$. To the pre-cooled solution of $\mathrm{AcFcBF_4}$ in $\mathrm{CH_2Cl_2}$, 65 µL of the $[\mathrm{Mn^{III}H_3}\mathbf{3}^{5F}(\mathrm{O})]^{2-}$ solution in THF was added via a gas-tight syringe. The reaction was monitored spectrophotometrically until no further changes to the UV-vis spectrum were observed.

Oxidation of $[\mathrm{Mn^{III}H_2}\mathbf{3}^{5F}(\mathrm{OH})]^{2-}$ at Low Temperature using EPR Spectroscopy. This reaction was done using the same procedure described above for the oxidation of $[\mathrm{Mn^{III}H_3}\mathbf{3}^{Ph}(\mathrm{O})]^{2-}$ using EPR spectroscopy. 300 µL of 10 mM $[\mathrm{Mn^{III}H_2}\mathbf{3}^{5F}(\mathrm{OH})]^{2-}$ (6.2 mg, 0.010 mmol, 1 mL DMF:THF) in EPR tube and 30 µL of 68 mM $\mathrm{FeCp_2BF_4}$ at (18.5 mg, 0.0678 mmol, 1 mL DMF:THF).

Protonation of $[\mathrm{Mn^{IV}H_3}\mathbf{3}^{Ph}(\mathrm{O})]^{-}$ at Low Temperature using UV-vis Spectroscopy. A 3 mL solution of 0.21 mM $[\mathrm{Mn^{IV}H_3}\mathbf{3}^{Ph}(\mathrm{O})]^{-}$ was generated at – 80 °C in a 1 cm cuvette using the procedures described above. A stock solution of 44 mM $\mathrm{PhNH_3BF_4}$ (0.0081 g, 0.045 mmol) was prepared in DMF (1 mL). To the cooled solution of $[\mathrm{Mn^{IV}H_3}\mathbf{3}^{Ph}(\mathrm{O})]^{-}$, 15 µL of $\mathrm{PhNH_3BF_4}$ was added via gas-tight syringe. The reactions were monitored spectrophotometrically until no further changes to the UV-vis spectrum were observed.

Protonation of $[\mathrm{Mn^{IV}H_3}\mathbf{3}^{Ph}(\mathrm{O})]^{-}$ at Low Temperature using EPR Spectroscopy. A 200 µL solution of 16 mM $[\mathrm{Mn^{IV}H_3}\mathbf{3}^{Ph}(\mathrm{O})]^{-}$ was generated at – 80 °C in an EPR tube using the procedures described above. A stock solution of 78 mM $\mathrm{PhNH_3BF_4}$ (0.014 g, 0.078 mmol) was prepared in DMF:THF (1 mL). To the cooled solution of $[Mn^{IV}H_3\mathbf{3}^{Ph}(O)]^-$, 30 μL of $PhNH_3BF_4$ was added via gas-tight syringe. The EPR tube was shaken to mix the two reactants and the solution was frozen by placing the EPR tube in liquid N_2.

Protonation of $[Mn^{IV}H_2\mathbf{3}^{5F}(O)(H)]^-$ at Low Temperature using UV-vis Spectroscopy. This reaction was done using the same procedure described above for the protonation of $[Mn^{IV}H_3\mathbf{3}^{Ph}(O)]^{2-}$ using UV-vis spectroscopy. 4 mL of 0.28 mM $[Mn^{IV}H_2\mathbf{3}^{5F}(O)(H)]^-$ in the cuvette, 33 μL of $PhNH_3BF_4$ (0.0059 g, 0.033 mmol, 1 mL DMF).

Protonation of $[Mn^{IV}H_2\mathbf{3}^{5F}(O)(H)]^-$ at Low Temperature using EPR Spectroscopy. This reaction was done using the same procedure described above for the protonation of $[Mn^{IV}H_3\mathbf{3}^{Ph}(O)]^{2-}$ using EPR spectroscopy. 250 μL of 17 mM $[Mn^{IV}H_2\mathbf{3}^{5F}(O)(H)]^-$, 56 μL of $PhNH_3BF_4$ (0.014 g, 0.078 mmol, 1 mL DMF).

Calculation of Half-Life for $[Mn^{V}H_3\mathbf{3}^{Ph}(O)]$. A solution of $[Mn^{III}H_3\mathbf{3}^{Ph}(O)]^{2-}$ in DMF:THF was oxidized with two equiv of $FeCp_2BF_4$, as described in the procedure above. The decay of the 854nm absorbance band corresponding to the Mn^V species was monitored. The absorbance at time 't' (A) of a sample was recorded until there was no further changes in the absorbance spectrum. The final absorbance was used as the endpoint for the reaction (A_{inf}). Time was plotted against the expression, $\ln[(A - A_{inf})/(A_i - A_{inf})]$ (A_i is the initial absorbance) for the first three half-lives of a given reaction to give a linear relationship, suggesting a first-order decay of the Mn^V species. The observed first-order rate constants (k, s^{-1}) for the decay was determined from the plot of $\ln[(A - A_{inf})/(A_i - A_{inf})] = kt$. The half-life was calculated by the expression $t_{1/2} = \ln(2)/k$.

References

(1) Holm, R. H. Metal-Centered Oxygen Atom Transfer Reactions. *Chem. Rev.* **1987**, *87* (6), 1401–1449.

(2) Mayer, J. M. Hydrogen Atom Abstraction by Metal-Oxo Complexes: Understanding the Analogy with Organic Radical Reactions. *Acc. Chem. Res.* **1998**, *31* (8), 441–450.

(3) Yin, G. Active Transition Metal Oxo and Hydroxo Moieties in Nature's Redox, Enzymes and Their Synthetic Models: Structure and Reactivity Relationships. *Coord. Chem. Rev.* **2010**, *254* (15–16), 1826–1842.

(4) Chen, Z.; Yin, G. The Reactivity of the Active Metal Oxo and Hydroxo Intermediates and Their Implications in Oxidations. *Chem. Soc. Rev.* **2015**, *44* (5), 1083–1100.

(5) Dismukes, G. C. The Metal Centers of the Photosynthetic Oxygen-Evolving Complex. *Photochem. Photobiol.* **1986**, *43* (1), 99–115.

(6) Vrettos, J. S.; Brudvig, G. W. Water Oxidation Chemistry of Photosystem II. *Philos. Trans. R. Soc. B Biol. Sci.* **2002**, *357* (1426), 1395–1405.

(7) McEvoy, J. P.; Brudvig, G. W. Water-Splitting Chemistry of Photosystem II. *Chem. Rev.* **2006**, *106* (11), 4455–4483.

(8) Ishikita, H.; Saito, K. Proton Transfer Reactions and Hydrogen-Bond Networks in Protein Environments. *J. R. Soc. Interface* **2013**, *11* (91), 20130518–20130518.

(9) MacBeth, C. E.; Hammes, B. S.; Young, V. G.; Borovik, A. S. Hydrogen-Bonding Cavities about Metal Ions: Synthesis, Structure, and Physical Properties for a Series of Monomeric M−OH Complexes Derived from Water. *Inorg. Chem.* **2001**, *40* (18), 4733–4741.

(10) Parsell, T. H.; Behan, R. K.; Green, M. T.; Hendrich, M. P.; Borovik, A. S. Preparation and Properties of a Monomeric MnIV-Oxo Complex. *J. Am. Chem. Soc.* **2006**, *128* (27), 8728–8729.

(11) Taguchi, T.; Gupta, R.; Lassalle-Kaiser, B.; Boyce, D. W.; Yachandra, V. K.; Tolman, W. B.; Yano, J.; Hendrich, M. P.; Borovik, A. S. Preparation and Properties of a Monomeric High-Spin Mn(V)-Oxo Complex. *J. Am. Chem. Soc.* **2012**, *134* (4), 1996–1999.

(12) Taguchi, T.; Stone, K. L.; Gupta, R.; Kaiser-Lassalle, B.; Yano, J.; Hendrich, M. P.; Borovik, A. S. Preparation and Properties of an MnIV–hydroxide Complex: Proton and Electron Transfer at a Mononuclear Manganese Site and Its Relationship to the Oxygen Evolving Complex within Photosystem II. *Chem. Sci.* **2014**, *5* (8), 3064.

(13) MacBeth, C. E.; Gupta, R.; Mitchell-Koch, K. R.; Young, V. G.; Lushington, G. H.; Thompson, W. H.; Hendrich, M. P.; Borovik, A. S. Utilization of Hydrogen Bonds To Stabilize M−O(H) Units: Synthesis and Properties of Monomeric Iron and Manganese Complexes with Terminal Oxo and Hydroxo Ligands. *J. Am. Chem. Soc.* **2004**, *126* (8), 2556–2567.

(14) Parsell, T. H.; Behan, R. K.; Green, M. T.; Hendrich, M. P.; Borovik, A. S. Preparation and Properties of a Monomeric Mn IV −Oxo Complex. *J. Am. Chem. Soc.* **2006**, *128* (27), 8728–8729.

(15) Parsell, T. H.; Yang, M.-Y.; Borovik, A. S. C−H Bond Cleavage with Reductants: Re-Investigating the Reactivity of Monomeric MnIII/IV−Oxo Complexes and the Role of Oxo Ligand Basicity. *J. Am. Chem. Soc.* **2009**, *131* (8), 2762–2763.

(16) Gupta, R.; Taguchi, T.; Borovik, A. S.; Hendrich, M. P. Characterization of Monomeric Mn(II/III/IV)-Hydroxo Complexes from X- and Q-Band Dual Mode Electron Paramagnetic Resonance (EPR) Spectroscopy. *Inorg. Chem.* **2013**, *52* (21), 12568–

12575.

(17) Grzybkowski, W. Nature and Properties of Metal Cations in Aqueous Solutions. *Polish J. Environ. Stud.* **2006**, *15* (4), 655–663.

(18) Connelly, N. G.; Geiger, W. E. Chemical Redox Agents for Organometallic Chemistry. *Chem. Rev.* **1996**, *96* (2), 877–910.

CHAPTER 5

Fe–O(H) Complexes with Hybrid Tripodal Ligands

Introduction

Our group has synthesized and characterized $Fe^{III/IV}$–O and $Fe^{II/III}$–OH complexes with the ligand $[H_3buea]^{3-}$.[1,2] The electron paramagnetic resonance (EPR) spectra of the Fe^{III}–O ($[Fe^{III}H_3buea(O)]^{2-}$) and Fe^{III}–OH ($[Fe^{III}H_3buea(OH)]^{-}$) complexes are indicative of the protonation state of the complexes. In $[Fe^{III}H_3buea(OH)]^{-}$, a rhombic spectrum is observed because the presence of a hydroxido ligand results in a distortion to the H-bond cavity. However, in $[Fe^{III}H_3buea(O)]^{2-}$ an axial EPR spectrum is found because of the symmetrically arrangement of the three tripodal arms around the Fe–O unit. In Chapter 3, the synthesis, characterization and properties of Mn^{III} complexes with the hybrid tripodal urea ligands $[H_2\mathbf{3}^{R}]^{4-}$ was described and compared to the previously characterized complexes with $[H_3buea]^{3-}$. The two ligands $[H_2\mathbf{3}^{Ph}]^{4-}$ and $[H_2\mathbf{3}^{F}]^{4-}$ produced Mn^{III}–O complexes, whereas the ligand $[H_2\mathbf{3}^{5F}]^{4-}$ with the most electron withdrawing substituents resulted in a Mn^{III}–OH complex. In this chapter, preliminary $Fe^{III/IV}$ chemistry with $[H_2\mathbf{3}^{Ph}]^{4-}$ and $[H_2\mathbf{3}^{5F}]^{4-}$ are reported. The identity of the axial ligand is probed using EPR spectroscopy and the oxidation chemistry of these Fe^{III} complexes are reported.

Results and Discussion

Synthesis of Fe^{III} *Complexes with* $[H_2\mathbf{3}^{Ph}]^{4-}$ *and* $[H_2\mathbf{3}^{5F}]^{4-}$. The Fe^{III}–O(H) complex of $[H_2\mathbf{3}^{Ph}]^{4-}$ and $[H_2\mathbf{3}^{5F}]^{4-}$ were synthesized by according to the procedure for $[Fe^{III}H_3buea(O)]^{2-}$ and the Mn^{III} complexes reported in Chapter 3.[3] The synthesis began by deprotonating the ligand precursor $H_6\mathbf{3}^{Ph}$ or $H_6\mathbf{3}^{5F}$ in dimethylacetamide (DMA) with 4 equivalents (equiv) of KH under an argon atmosphere and then adding

$Fe^{II}(OAc)_2$ to give a colorless heterogeneous mixture (Scheme 5.1). The mixture was treated with 0.5 equiv of dry O_2, resulting in an immediate color change to deep red. The mixture was filtered to remove KOAc and was purified by vapor diffusion of Et_2O into the DMA solution of the salt. As shown in Scheme 5.1, the position of the proton is not known in the two complexes, however they are written as $[Fe^{III}H_3\mathbf{3}^{Ph}(O)]^{2-}$ and $[Fe^{III}H_2\mathbf{3}^{5F}(OH)]^{2-}$ for the rest of the chapter because of the data from the Mn^{III} complexes presented in Chapter 3. The molecular structures of the two Fe^{III} complexes were not obtained by X-ray diffraction (XRD) because suitable single crystals could not be obtained.

Scheme 5.1. Preparative Routes to Fe^{III} Complexes with Hybrid Tripodal Urea Ligands

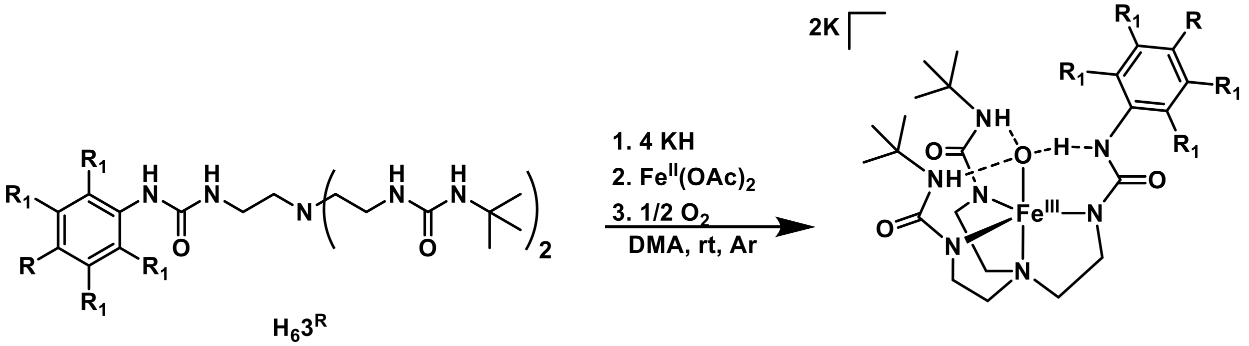

Electronic Properties of Fe^{III} Complexes. The electronic properties of the Fe^{III} complexes were probed using electronic absorbance spectroscopy and compared to $[Fe^{III}H_3buea(O)]^{2-}$ and $[Fe^{III}H_3buea(OH)]^{-}$ that were previously reported (Figure 5.1 and Table 5.1).[3,4] The Fe^{III}–O and Fe^{III}–OH complexes in this study are characterized by absorbance bands at λ_{max} = 387 and 384 nm, respectively with extinction coefficients greater than 4000 M^{-1} cm^{-1}. The shifts in the electronic absorbance spectra of these complexes depending on their protonation state are more subtle than the Mn^{III} complexes presented in Chapter 3.

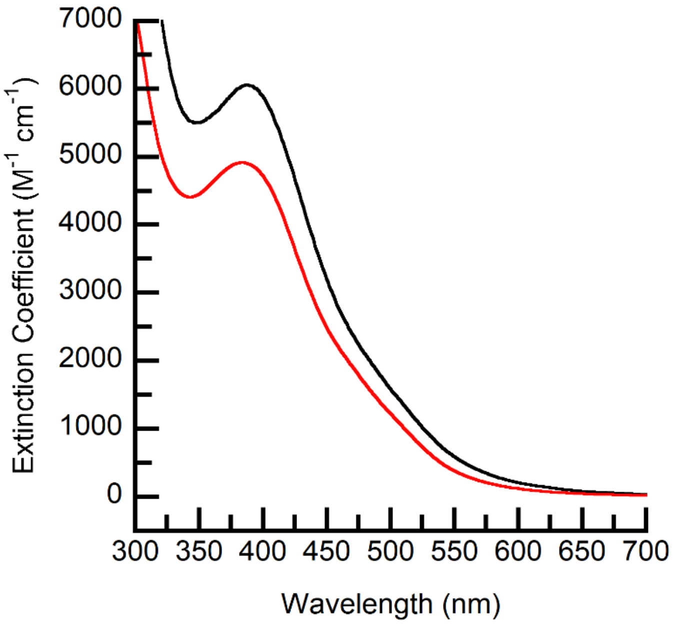

Figure 5.1. Electronic absorbance spectra for $[\mathrm{Fe^{III}H_3}\mathbf{3}^{\mathrm{Ph}}(\mathrm{O})]^{2-}$ (black line) and $[\mathrm{Fe^{III}H_2}\mathbf{3}^{\mathrm{5F}}(\mathrm{OH})]^{2-}$ (red line) recorded in DMA at room temperature.

Table 5.1. Electronic Absorbance Properties of $\mathrm{Fe^{III}}$–O and $\mathrm{Fe^{III}}$–OH Complexes

	λ_{max} (nm), (ε, M $\mathrm{cm^{-1}}$)
$[\mathrm{Fe^{III}H_3buea(O)}]^{2-}$ [a]	392 (2100)
$[\mathrm{Fe^{III}H_3buea(OH)}]^{-}$ [a]	382 (4000)
$[\mathrm{Fe^{III}H_3}\mathbf{3}^{\mathrm{Ph}}(\mathrm{O})]^{2-}$	387 (6100)
$[\mathrm{Fe^{III}H_2}\mathbf{3}^{\mathrm{5F}}(\mathrm{O})(\mathrm{H})]^{2-}$	384 (4900)

[a] Data obtained from ref [4]

EPR Properties of Fe^{III} Complexes. The magnetic properties of the $\mathrm{Fe^{III}}$ complexes were studied using EPR spectroscopy. The perpendicular-mode EPR spectra are very sensitive to the coordination geometry around the $\mathrm{Fe^{III}}$ center. The perpendicular mode EPR spectra conducted at 10K of $[\mathrm{Fe^{III}H_3}\mathbf{3}^{\mathrm{Ph}}(\mathrm{O})]^{2-}$ revealed broad signals centered around g = 6.0 and 2.0 (Figure 5.2), which is representative of an $\mathrm{Fe^{III}}$ center with a S = 5/2 spin ground state. The spectrum is consistent with the complex having axial symmetry with an E/D value of ~ 0. The signal at g = 4.3 represents adventitious $\mathrm{Fe^{III}}$, which is less than 10% of the total $\mathrm{Fe^{III}}$ in the sample. The axial EPR spectrum is similar to that measured $[\mathrm{Fe^{III}H_3buea(O)}]^{2-}$, in which the three tripodal arms of the $[H_3buea]^{3-}$ ligand are symmetrically arranged around the Fe^{III}–O unit.[3]

The perpendicular-mode EPR spectrum of $[Fe^{III}H_2\mathbf{3}^{5F}(OH)]^{2-}$ shows a more rhombic signal with features at g = 7.7, 4.9, and 3.9. The signal at g = 4.3 again represents adventitious Fe^{III}, which was determined to be less 10% of the total Fe^{III} in the sample by spin quantification. This experimentally determined E/D of 0.21 is more rhombic than $[Fe^{III}H_3buea(OH)]^-$ (Figure 5.2).[3] The more rhombic EPR spectrum could suggest this complex is a Fe^{III}–OH species, which could arise from a H-bond forming between a hydroxido ligand and a deprotonated perfluorinated phenyl urea nitrogen, similar to that found for $[Mn^{III}H_2\mathbf{3}^{5F}(OH)]^{2-}$ (Chapter 3). In $[Mn^{III}H_2\mathbf{3}^{5F}(OH)]^{2-}$ there are statistically significant differences in the Mn1–N_{trig} distances, which would result in a more rhombic EPR spectrum for the analogous Fe complex. In addition, the EPR spectrum of $[Fe^{III}H_3buea(OH)]^-$ contains signals at g = 8.9, 5.3, 3.4, and 1.3 with an E/D of 0.17.[3]

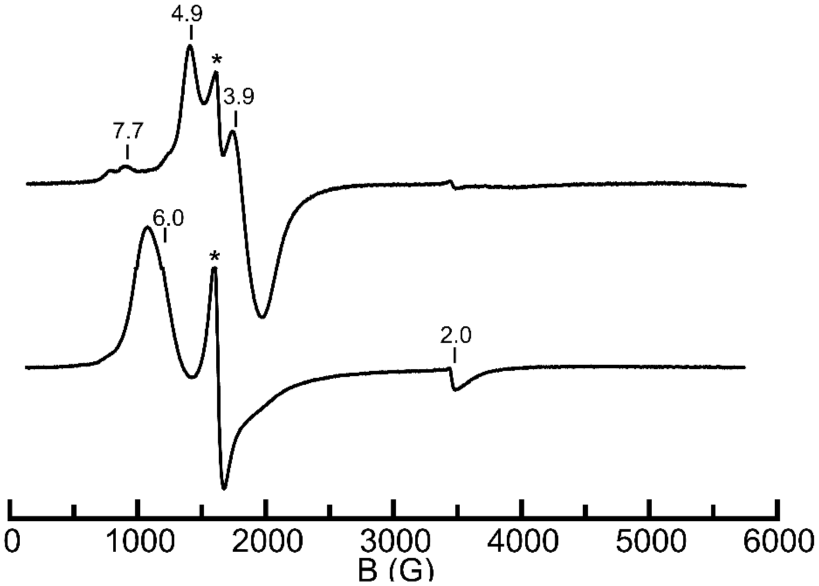

Figure 5.2. Perpendicular mode EPR spectra of $[Fe^{III}H_3\mathbf{3}^{Ph}(O)]^{2-}$ (bottom) and $[Fe^{III}H_2\mathbf{3}^{5F}(OH)]^{2-}$ (top) recorded in DMA at 10K.

*Oxidation of [Fe^{III}H$_3$**3**^{Ph}(O)]$^{2-}$.* Treatment of [Fe^{III}H$_3$**3**^{Ph}(O)]$^{2-}$ with one equiv of [FeCp$_2$]$^+$ at room temperature in DMA results in loss of the characteristic band for [Fe^{III}H$_3$**3**^{Ph}(O)]$^{2-}$ at λ_{max}/nm = 387 and growth of new broad absorbance bands at λ_{max}/nm = 450, 600, and 800, which is similar to the absorbance spectrum for [Fe^{IV}H$_3$buea(O)]$^-$ (λ_{max}/nm = 350, 440, 550, and 808) (Scheme 5.2 and Figure 5.3).[1]

Scheme 5.2. Oxidation of [Fe^{III}H$_3$3^{Ph}(O)]$^{2-}$ with [FeCp$_2$]$^+$

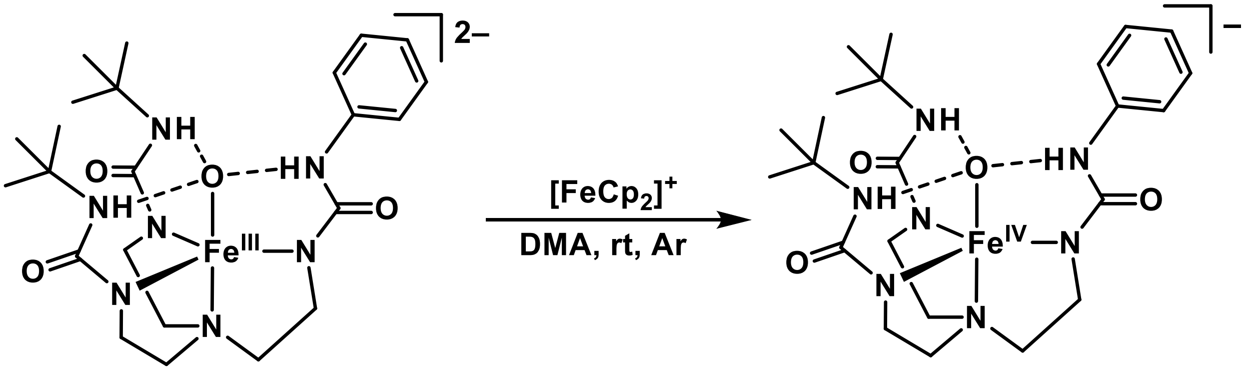

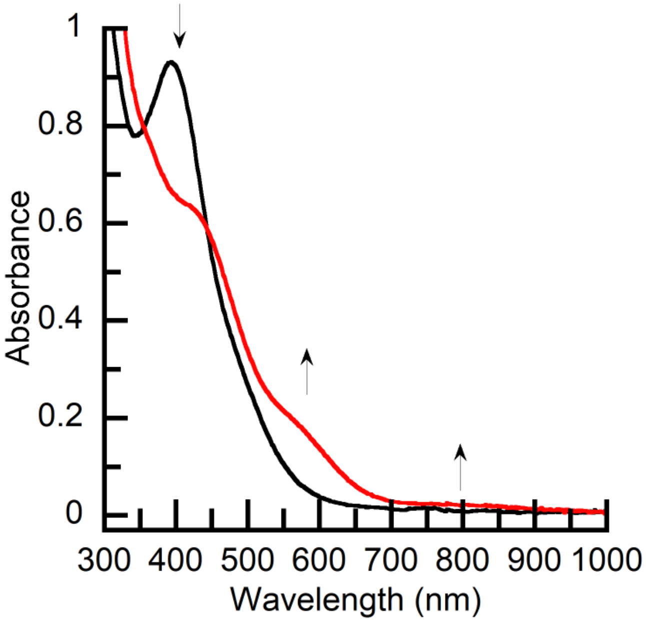

Figure 5.3. Electronic absorbance spectra of the reaction of [Fe^{III}H$_3$**3**^{Ph}(O)]$^{2-}$ with [FeCp$_2$]$^+$ recorded at room temperature in DMA.

Monitoring the oxidation reaction by perpendicular mode EPR spectroscopy shows loss of the axial signal corresponding to $[\mathrm{Fe^{III}H_3}\mathbf{3}^{\mathrm{Ph}}(\mathrm{O})]^{2-}$ and growth of a new rhombic signal at g = 8.6, 5.2, and 3.4 corresponding to new $\mathrm{Fe^{III}}$ species with an S = 5/2 spin ground state (Figure 5.4). The new $\mathrm{Fe^{III}}$ signal is not present in the starting $[\mathrm{Fe^{III}H_3}\mathbf{3}^{\mathrm{Ph}}(\mathrm{O})]^{2-}$ sample and only forms upon oxidation. This rhombic $\mathrm{Fe^{III}}$ accounts for ~ 20% of the starting Fe in the sample, as determined by spin quantification. The experimentally determined E/D for the new $\mathrm{Fe^{III}}$ species is 0.18, which is comparable to the 0.17 that is observed for $[\mathrm{Fe^{III}H_3buea(OH)}]^{2-}$.[1] Monitoring the oxidation by parallel mode EPR spectroscopy shows no signals in parallel mode corresponding to $\mathrm{Fe^{IV}}$. However, the perpendicular mode EPR spectra shows no residual $[\mathrm{FeCp_2}]^+$ left in the reaction, and 80% of the starting Fe is unaccounted for. Additional experiments, including Mössbauer studies, are required to determine fate and oxidation state(s) of the remaining Fe.

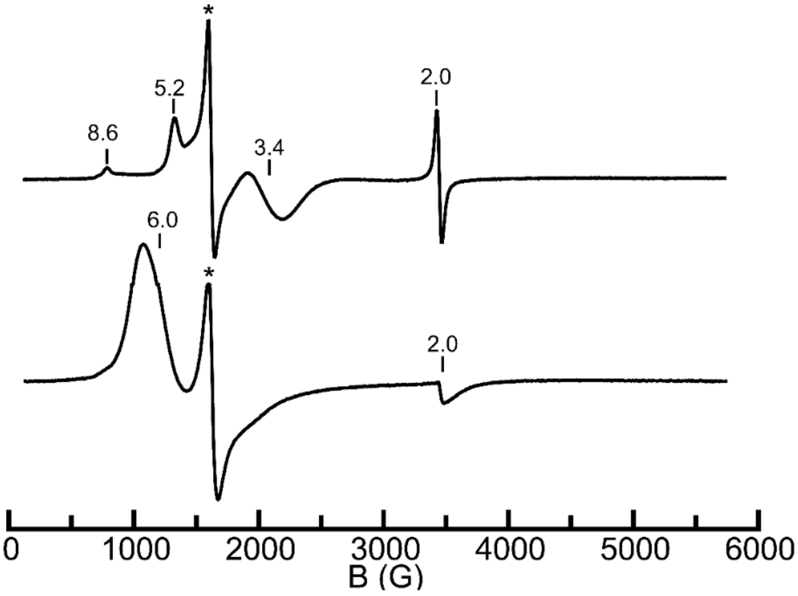

Figure 5.4. Perpendicular mode EPR spectra of $[\mathrm{Fe^{III}H_3}\mathbf{3}^{\mathrm{Ph}}(\mathrm{O})]^{2-}$ (bottom) and the reaction of $[\mathrm{Fe^{III}H_3}\mathbf{3}^{\mathrm{Ph}}(\mathrm{O})]^{2-}$ with $[\mathrm{FeCp_2}]^+$ in DMA at – 20 °C (top). EPR spectra collected at 10 K in DMA.

Oxidation of $[\mathrm{Fe^{III}H_2}\mathbf{3}^{5F}(\mathrm{OH})]^{2-}$. Treatment of $[\mathrm{Fe^{III}H_3}\mathbf{3}^{5F}(\mathrm{OH})]^{2-}$ with one equiv of $[\mathrm{FeCp_2}]^{+}$ results in loss of the characteristic band for $[\mathrm{Fe^{III}H_2}\mathbf{3}^{5F}(\mathrm{OH})]^{2-}$ at λ_{max}/nm = 384 (Figure 5.5). A shoulder at λ_{max}/nm ~ 400 nm is present in the oxidized product. The electronic absorbance spectrum shows complete consumption of $[\mathrm{FeCp_2}]^{+}$. The new species does not have similar absorbance bands to $[\mathrm{Fe^{IV}H_3buea(O)}]^{-}$ or the oxidized product of $[\mathrm{Fe^{III}H_3}\mathbf{3}^{Ph}(\mathrm{O})]^{2-}$.[1]

Scheme 5.3. Oxidation of $[\mathrm{Mn^{III}H_2}3^{5F}(\mathrm{OH})]^{2-}$

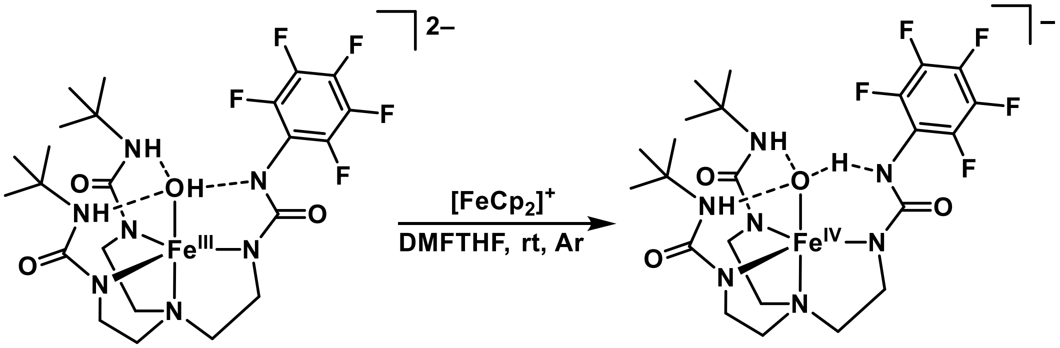

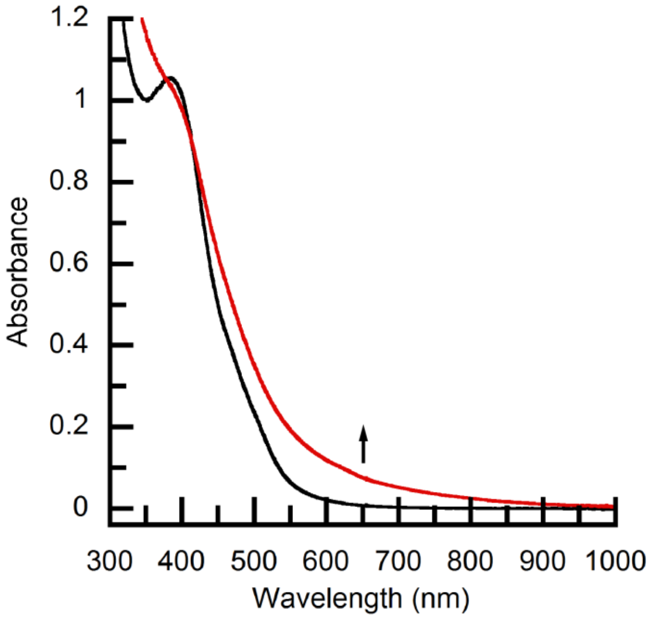

Figure 5.5. Electronic absorbance spectra of the reaction of $[\mathrm{Fe^{III}H_2}\mathbf{3}^{5F}(\mathrm{OH})]^{2-}$ with $[\mathrm{FeCp_2}]^{+}$ recorded at – 40 °C in DMF:THF.

Monitoring this reaction by perpendicular mode EPR spectroscopy shows loss of the starting rhombic signal corresponding to $[\mathrm{Fe^{III}H_2}\mathbf{3}^{5F}(\mathrm{OH})]^{2-}$ and growth of a new rhombic signal at g = 8.6, 5.2, and 3.4 corresponding to high-spin Fe^{III} (Figure 5.6). This new Fe^{III} species has an identical EPR spectrum to the product made from the oxidation of $[Fe^{III}H_3\mathbf{3}^{Ph}(O)]^{2-}$ with $[FeCp_2]^+$ and has a calculated E/D of 0.18. This rhombic Fe^{III} species is only produced upon oxidation and accounts for ~ 20% of the original starting Fe concentration. Monitoring the oxidation by parallel-mode EPR spectroscopy shows no evidence for Fe^{IV}. However, the perpendicular mode EPR spectra shows complete consumption of the $[FeCp_2]^+$. Similar to the oxidation of $[Fe^{III}H_3\mathbf{3}^{Ph}(O)]^{2-}$, 80% of the starting Fe is unaccounted for in the perpendicular and parallel mode EPR spectra and Mössbauer studies are required to determine oxidation state of the remaining Fe.

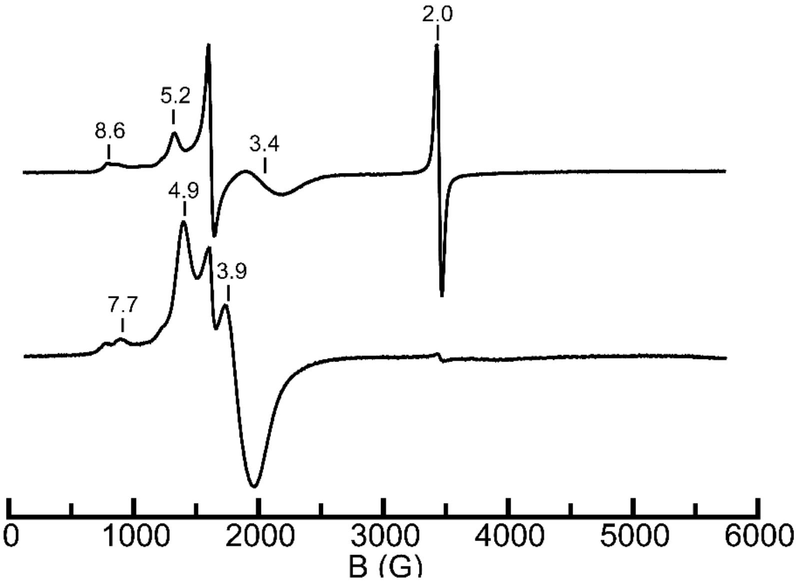

Figure 5.6. Perpendicular mode EPR spectra of $[Fe^{III}H_2\mathbf{3}^{5F}(OH)]^{2-}$ (bottom) and the reaction of $[Fe^{III}H_2\mathbf{3}^{5F}(OH)]^{2-}$ with $[FeCp_2]^+$ in DMA at – 20 °C (top). EPR spectra collected at 10 K in DMA.

The electronic absorbance spectra for the oxidation of $[Fe^{III}H_3\mathbf{3}^{Ph}(O)]^{2-}$ and $[Fe^{III}H_3\mathbf{3}^{5F}(OH)]^{2-}$ with $[FeCp_2]^+$ show different features, however, the EPR spectra shows an identical EPR parameters in perpendicular mode accounting for 20% of the total starting Fe in the sample (Figure 5.7). The remaining Fe in the sample does not show up in perpendicular or parallel mode EPR spectroscopy: there are two at least possibilities to account for this lack of signal. The first is that upon oxidation to an Fe^{IV} species, an Fe^{III}–(μ–O)–Fe^{III} dimers could be formed, which would not have an EPR signal because of antiferromagnetic coupling between the two Fe(III) centers. Alternatively, the Fe^{IV} produced could be difficult to observe in parallel-mode EPR spectroscopy and Mössbauer spectroscopy may be needed to determine the oxidation state of the major product.

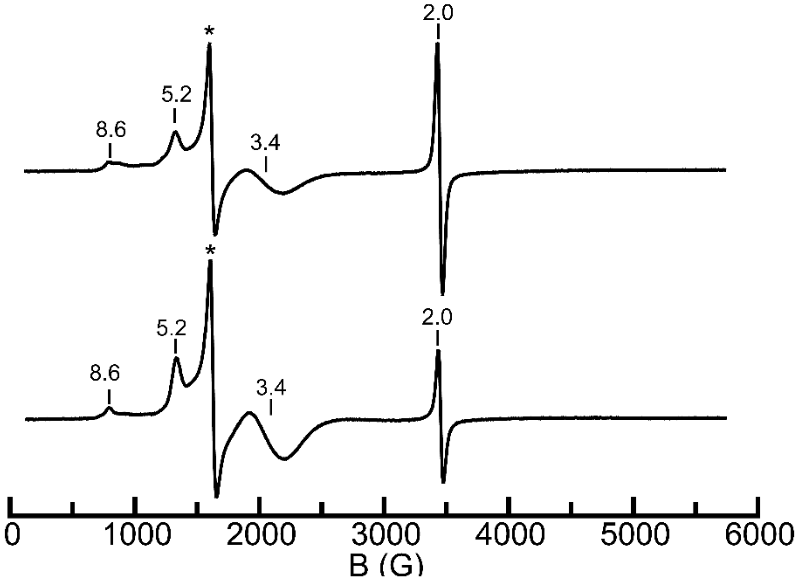

Figure 5.7. Perpendicular mode EPR spectra of the oxidation of [Fe^{III}H$_3$**3**^{Ph}(OH)]$^{2-}$ (top) and [Fe^{III}H$_2$**3**^{5F}(OH)]$^{2-}$ (bottom) with [FeCp$_2$]$^+$ in DMA at – 20 °C. EPR spectra collected at 10 K in DMA. Both rhombic Fe^{III} signals correspond to 20% of the starting Fe concentration.

Summary and Conclusions

New Fe^{III} complexes with [H$_2$**3**^{Ph}]$^{4-}$ and [H$_2$**3**^{5F}]$^{3-}$ were synthesized and characterized. The EPR spectrum of [Fe^{III}H$_3$**3**^{Ph}(O)]$^{2-}$ is axial, similar to [Fe^{III}H$_3$buea(O)]$^{2-}$, suggesting it is an Fe^{III}–O complex. In contrast, the EPR spectrum of [Fe^{III}H$_2$**3**^{5F}(OH)]$^{2-}$ is rhombic, having an E/D = 0.21. These findings suggest a more asymmetric coordination environment than [Fe^{III}H$_3$**3**^{Ph}(O)]$^{2-}$, which could result from the compound being a Fe^{III}–OH with a deprotonated perfluorinated phenyl urea nitrogen, similar to $[Mn^{III}H_2\mathbf{3}^{5F}(OH)]^{2-}$ reported in Chapter 3.

These Fe^{III} complexes can be oxidized with $[FeCp_2]^+$ to produce species with different electronic absorbance spectra. When $[Fe^{III}H_3\mathbf{3}^{Ph}(O)]^{2-}$ is oxidized, it produces an electronic absorbance spectrum that is characteristic of $[Fe^{IV}H_3buea(O)]^-$. However, the oxidation of $[Fe^{III}H_2\mathbf{3}^{5F}(OH)]^{2-}$ produces an electronic absorbance spectrum that is unlike other Fe^{IV}=O species characterized by our group. Monitoring these reactions by EPR spectroscopy shows no evidence for Fe^{IV} and produces an identical rhombic Fe^{III} species accounting for 20% of the starting Fe concentration. The composition of the remaining 80% of Fe is unknown at this point and further Mössbauer studies are required to find the composition of these species.

Experimental Section

General Procedures. All manipulations, unless otherwise stated, were performed under an argon atmosphere in a Vac-atmospheres dry box. All chemicals were purchased from commercial sources and used without further purification unless otherwise stated. *N,N*-Dimethylacetamide was purchased from Sigma-Aldrich in 99.8% purity and stirred over BaO for two days, refluxed for 1 h, followed by vacuum distillation and storage over 4 Å molecular sieves. Potassium hydride (KH) as a 30% dispersion in mineral oil was filtered with a glass frit and washed with pentane and Et_2O, dried by vacuum, and stored under an argon atmosphere. $FeCp_2BF_4$ was prepared according to the published procedure.[5] Ligand precursors $H_6\mathbf{3}^{Ph}$ and $H_6\mathbf{3}^{5F}$ were prepared according to the procedures in Chapter 3.

Physical Methods. Electronic absorption spectra for oxidation reactions were recorded in a 1 cm cuvette on an 8453 Agilent UV-Vis spectrometer equipped with an

Unisoku Unispeks cryostat. Room temperature electronic absorption spectra for determining extinction coefficients were recorded in a 1 cm cuvette on a Cary 50 spectrometer. EPR spectra were recorded using a Bruker EMX spectrometer equipped with an ER041XG microwave bridge, an Oxford Instrument liquid-helium quartz cryostat, and a dual mode cavity (ER4116DM).

Oxidation of $[Fe^{III}H_3\mathbf{3}^{Ph}(O)]^{2-}$ using UV/vis spectroscopy. A stock solution of $[Fe^{III}H_3\mathbf{3}^{Ph}(O)]^{2-}$ at 17 mM concentration (10 mg, 0.017 mmol) was prepared in a DMA solution (1 mL). In a typical experiment, 4 mL of DMA was loaded in the cuvette and sealed with a rubber septum. To the cuvette, 47 µL of Fe^{III} solution was transferred to generate a 0.20 mM solution of $[Fe^{III}H_3\mathbf{3}^{Ph}(OH)]^{2-}$. A stock solution of $FeCp_2BF_4$ at 84 mM (23 mg, 0.084 mmol) was prepared in DMF:THF solution (1 mL). To the $[Fe^{III}H_3\mathbf{3}^{Ph}(OH)]^{2-}$ solution, one equiv of $FeCp_2BF_4$ was added via gas-tight syringe. The reactions were monitored spectrophotometrically until no further changes to the UV/vis spectrum were observed.

Oxidation of $[Fe^{III}H_3\mathbf{3}^{Ph}(O)]^{2-}$ using EPR spectroscopy. Solid KH (0.0203 g, 0.506 mmol) was treated with a 3 mL DMA solution of $H_6\mathbf{3}^{Ph}$ (0.0564 g, 0.122 mmol) and stirred for 45 min until bubbling ceased. $Fe^{II}(OAc)_2$ (0.0220 g, 0.127 mmol) was then added as one portion and the resultant solution was stirred for 1 h to give a colorless heterogeneous mixture. The mixture treated with O_2 (1.4 mL, 0.063 mmol) to give a deep red mixture. The mixture was stirred for 2 h, degassed under vacuum for 5 min, and filtered through a medium porous-glass filter to give a deep red solution. A stock solution of $FeCp_2BF_4$ at 114 mM (0.0312g, 0.114 mmol) was prepared in DMA solution (1 mL). The deep red solution of $[Fe^{III}H_3\mathbf{3}^{Ph}(O)]^{2-}$ was loaded into a EPR tube (150 µL) and cooled to – 20 °C for 15 min. To the solution of

$[Fe^{III}H_3\mathbf{3}^{Ph}(O)]^{2-}$ in the EPR tube, one equiv of $FeCp_2BF_4$ (50 μL) was added via gas-tight syringe and allowed to react for 2 min and then frozen in liquid N_2.

Oxidation of $[Fe^{III}H_2\mathbf{3}^{5F}(O)]^{2-}$ *using UV/vis spectroscopy.* A stock solution of $[Fe^{III}H_2\mathbf{3}^{5F}(O)]^{2-}$ at 10 mM concentration (7.3 mg, 0.010 mmol) was prepared in DMF:THF solution (1 mL). In a typical experiment, 3 mL of DMF:THF was loaded in the cuvette, sealed with a rubber septum, and cooled to – 40 °C for 20 minutes. To the cuvette, 60 μL of Fe^{III} solution was transferred to generate a 0.20 mM solution of $[Fe^{III}H_2\mathbf{3}^{5F}(OH)]^{2-}$. A stock solution of $FeCp_2BF_4$ at 66 mM (18 mg, 0.066 mmol) was prepared in DMF:THF solution (1 mL). To the $[Fe^{III}H_2\mathbf{3}^{5F}(OH)]^{2-}$ solution, one equiv of $FeCp_2BF_4$ was added via gas-tight syringe. The reactions were monitored spectrophotometrically until no further changes to the UV/vis spectrum were observed.

Oxidation of $[Fe^{III}H_2\mathbf{3}^{5F}(O)]^{2-}$ *using EPR spectroscopy.* Solid KH (0.0265 g, 0.661 mmol) was treated with a 3 mL DMA solution of $H_6\mathbf{3}^{5F}$ (0.0892 g, 0.161 mmol) and stirred for 45 min until bubbling ceased. $Fe^{II}(OAc)_2$ (0.0280 g, 0.161 mmol) was then added as one portion and the resultant solution was stirred for 1 h to give a colorless heterogeneous mixture. The mixture treated with O_2 (1.8 mL, 0.080 mmol) to give a deep red mixture. The mixture was stirred for 2 h, degassed under vacuum for 5 min, and filtered through a medium porous-glass filter to give a deep red solution. A stock solution of $FeCp_2BF_4$ at 114 mM (0.0312g, 0.114 mmol) was prepared in DMA solution (1 mL). The deep red solution of $[Fe^{III}H_2\mathbf{3}^{5F}(OH)]^{2-}$ was loaded into a EPR tube (200 μL) and cooled to – 20 °C for 15 min. To the solution of $[Fe^{III}H_2\mathbf{3}^{5F}(O)]^{2-}$ in the EPR tube, one equiv of $FeCp_2BF_4$ (70 μL) was added via gas-tight syringe and allowed to react for 2 min and then frozen in liquid N_2.

Preparative Methods.

K_2[$Fe^{III}H_3$3^{Ph}(O)]. Solid KH (0.0701 g, 1.75 mmol) was treated with a 4 mL DMA solution of H_6**3**^{Ph} (0.2015 g, 0.4346 mmol) and stirred for 45 min until bubbling ceased. $Fe^{II}(OAc)_2$ (0.0760 g, 0.437 mmol) was then added as one portion and the resultant solution was stirred for 1 hr to give a colorless heterogeneous mixture. The mixture was transferred to a schlenk flask and sealed with a rubber septum and treated with dry O_2 (5.0 mL, 0.22 mmol), which produced a red color immediately. The mixture was stirred for 1 h, then degassed under vacuum for 5 min. The red mixture was filtered through a medium porous-glass filter, and 10 mL of Et_2O was allowed to diffuse resulting in a red precipitate after 1 day. The red precipitate was collected on a medium porous-glass filter and washed with 20 mL of MeCN and 20 mL of Et_2O to give 0.152 g of the desired red solid (57%). $\lambda_{max/nm}$ (DMA, ε, M^{-1} cm^{-1}): 387, (6100). EPR (DMA, 10 K): g = 6.0, 2.0 (E/D = 0). Anal. Calcd (found) for $C_{23}H_{38}K_2FeN_7O_4$•DMA: C, 46.48 (46.04); H, 6.79 (6.93); N, 16.06 (15.72). FTIR (ATR, cm^{-1}): 3286, 2961, 2915, 2910, 2845, 1630, 1590, 1541, 1496, 1484, 1446, 1412, 1395, 1384, 1331, 1309, 1260, 1208, 1153, 1149, 1122, 1062, 1035, 1013, 982, 910, 752, 696, 654, 595.

K_2[$Fe^{III}H_2$3^{5F}(OH)]. Solid KH (0.0605 g, 1.51 mmol) was treated with a 4 mL DMA solution of H_6**3**^{5F} (0.2051 mg, 0.3705 mmol) and stirred for 1 h until bubbling ceased. $Fe^{II}(OAc)_2$ (0.0651 mg, 0.374 mmol) was then added as one portion and the resultant solution was stirred for 1 hr to give a colorless heterogeneous mixture. The mixture was transferred to a schlenk flask and sealed with a rubber septum and treated with dry O_2 (4.2 mL, 0.19 mmol), which produced a deep red color immediately. The mixture was stirred for 2 h, then degassed under vacuum for 5 min. The deep red mixture was filtered through a medium porous-glass filter, and 15 mL of Et_2O layered over the DMA solution of the salt, resulting in a red precipitate after 1 day. The red precipitate was collected on a medium porous-glass filter and washed with 10 mL of MeCN and 20 mL of Et_2O to give 0.175 g of the desired red solid (68%). $\lambda_{max/nm}$ (DMA, ε, M^{-1} cm^{-1}): 384, (4900). EPR (DMA, 10 K): g = 7.7, 4.9, 3.9 (E/D = 0.21). FTIR (ATR, cm^{-1}): 3350, 3252, 3023, 2960, 2924, 2854, 1647, 1583, 1536, 1484, 1448, 1381, 1357, 1285, 1213, 1147, 983, 953, 782, 710, 668, 635, 566.

References

(1) Lacy, D. C.; Gupta, R.; Stone, K. L.; Greaves, J.; Ziller, J. W.; Hendrich, M. P.; Borovik, A. S. Formation, Structure, and EPR Detection of a High Spin Fe(IV)—Oxo Species Derived from Either an Fe(III)—Oxo or Fe(III)—OH Complex. *J. Am. Chem. Soc.* **2010**, *132* (35), 12188–12190.

(2) Gupta, R.; Borovik, A. S. Monomeric Mn(III/II) and Fe(III/II) Complexes with Terminal Hydroxo and Oxo Ligands: Probing Reactivity via O−H Bond Dissociation Energies. *J. Am. Chem. Soc.* **2003**, *125* (43), 13234–13242.

(3) MacBeth, C. E.; Golombek, A. P.; Young Jr., V. G.; Yang, C.; Kuczera, K.; Hendrich, M. P.; Borovik, A. S. O2 Activation by Nonheme Iron Complexes: A Monomeric Fe(III)-Oxo Complex Derived from O2. *Science.* **2000**, *289* (5481), 938–941.

(4) MacBeth, C. E.; Gupta, R.; Mitchell-Koch, K. R.; Young, V. G.; Lushington, G. H.; Thompson, W. H.; Hendrich, M. P.; Borovik, A. S. Utilization of Hydrogen Bonds To Stabilize M−O(H) Units: Synthesis and Properties of Monomeric Iron and Manganese Complexes with Terminal Oxo and Hydroxo Ligands. *J. Am. Chem. Soc.* **2004**, *126* (8), 2556–2567.

(5) Connelly, N. G.; Geiger, W. E. Chemical Redox Agents for Organometallic Chemistry. *Chem. Rev.* **1996**, *96* (2), 877–910.

APPENDIX A

M^{II}–OH Complexes with $[H_3\mathbf{3}^{Ph}]^{3-}$ and $[H_3\mathbf{3}^{F}]^{3-}$

Synthesis of Metal Complexes

Synthesis of $K_2[Mn^{II}H_3\mathbf{3}^{Ph}(OH)]$. A solution of $H_6\mathbf{3}^{Ph}$ was treated with four equiv of potassium hydride (KH) in anhydrous dimethylacetmide (DMA). Once H_2 evolution had ceased, $Mn^{II}(OAc)_2$ was added. After 30 min, one equiv of H_2O was added and the mixture was filtered to remove KOAc. Single crystals of the metal salt were obtained by diffusion of diethyl ether (Et_2O) into the DMA solution. The molecular structure of $K_2[Mn^{II}H_3\mathbf{3}^{Ph}(OH)]$ was obtained by X-ray diffraction (XRD), revealing a Mn^{II} center with a trigonal bipyramidal coordination geometry (Figure A.1 and Table A.1).

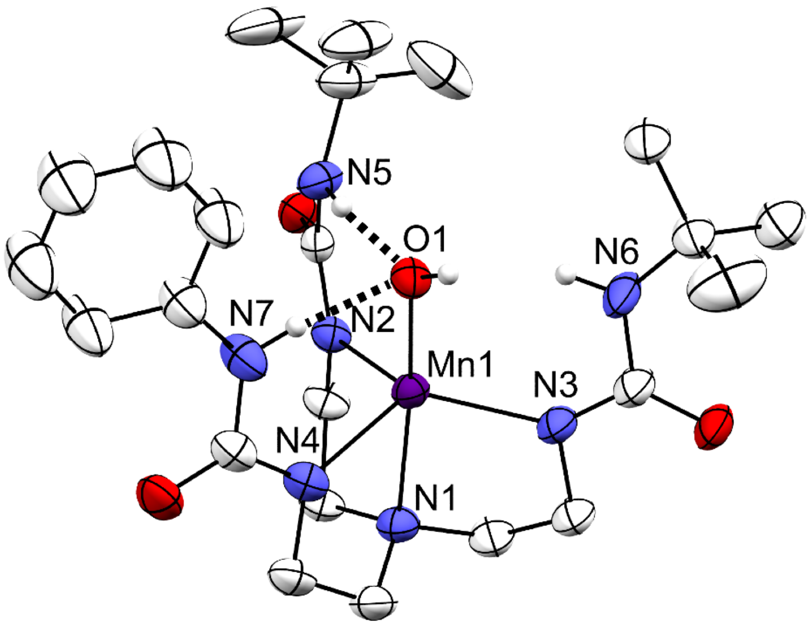

Figure A.1. Thermal ellipsoid plot of $[Mn^{II}H_3\mathbf{3}^{Ph}(OH)]^{2-}$. Thermal ellipsoids are drawn at the 50% probability level. Hydrogen atoms bonded to carbon were removed for clarity.

Table A.1. Selected Bond Distances (Å) and Angles (°) for $[Mn^{II}H_3\mathbf{3}^{Ph}(OH)]^{2-}$

Mn1–O1	2.060(2)
Mn1–N1	2.314(2)
Mn1–N2	2.157(2)
Mn1–N3	2.141(2)
Mn1–N4	2.206(2)
d(N5···O1)	2.922(3)
d(N7···O1)	2.744(3)
O1–Mn1–N1	173.99(7)
O1–Mn1–N2	102.72(7)
O1–Mn1–N3	106.27(7)
O1–Mn1–N4	97.90(7)
N4–Mn1–N1	76.09(8)
N4–Mn1–N2	103.76(8)
N4–Mn1–N3	126.13(8)
N2–Mn1–N1	78.75(7)
N2–Mn1–N3	116.22(8)
N1–Mn1–N3	77.94(8)

Synthesis of $K_2[Mn^{II}H_3\mathbf{3}^{F}(OH)]$. The synthesis of was conducting using the same methodology as reported above for $K_2[Mn^{II}H_3\mathbf{3}^{Ph}(OH)]$, except $H_6\mathbf{3}^{F}$ was used, however the product was obtained as a white powder and single-crystals suitable for XRD were not obtained.

Synthesis of $\mathrm{K_2[Fe^{II}H_3\mathbf{3}^{Ph}(OH)]}$. The synthesis was conducted using the same methodology as the synthesis of $\mathrm{K_2[Mn^{II}H_3\mathbf{3}^{Ph}(OH)]}$, except $\mathrm{Fe^{II}(OAc)_2}$ was used. The molecular structure of $\mathrm{K_2[Fe^{II}H_3\mathbf{3}^{Ph}(OH)]}$ was obtained by XRD, revealing a $\mathrm{Fe^{II}}$ center with a trigonal bipyramidal coordination geometry. (Figure A.2 and Table A.2)

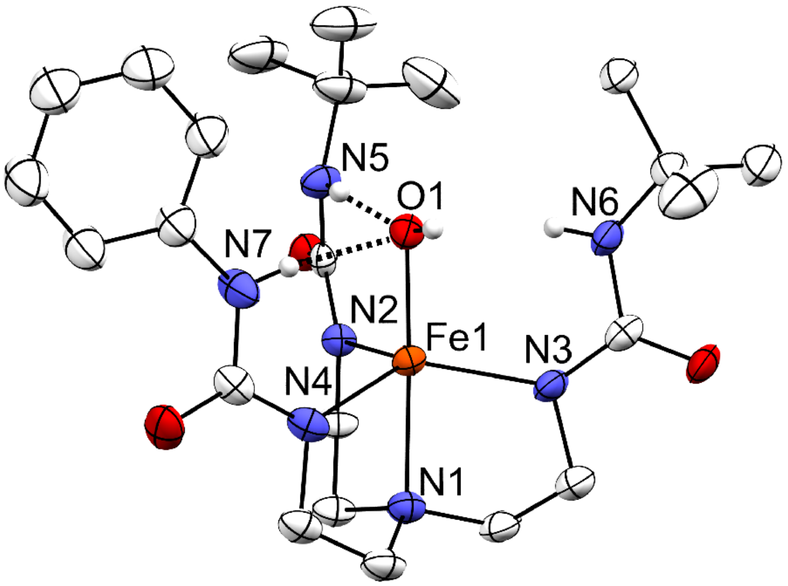

Figure A.2. Thermal ellipsoid plot of $\mathrm{[Fe^{II}H_3\mathbf{3}^{Ph}(OH)]^{2-}}$. Thermal ellipsoids are drawn at the 50% probability level. Hydrogen atoms bonded to carbon were removed for clarity.

Table A.2. Selected Bond Distances (Å) and Angles (°) for $\mathrm{[Fe^{II}H_3\mathbf{3}^{Ph}(OH)]^{2-}}$

Fe1–O1	2.059(2)
Fe1–N1	2.254(3)
Fe1–N2	2.097(3)
Fe1–N3	2.081(3)
Fe1–N4	2.136(3)
d(N5···O1)	2.914(4)
d(N7···O1)	2.731(4)
O1–Fe1–N1	174.14(10)
O1–Fe1–N2	104.29(10)
O1–Fe1–N3	101.99(10)
O1–Fe1–N4	96.82(10)
N4–Fe1–N1	77.90(11)
N4–Fe1–N2	104.59(11)
N4–Fe1–N3	129.65(11)
N2–Fe1–N1	79.71(10)
N2–Fe1–N3	114.98(11)
N1–Fe1–N3	79.83(11)

Synthesis of $\mathrm{K_2[Fe^{II}H_3\mathbf{3}^{F}(OH)]}$. The synthesis was conducted using the same methodology as the synthesis of $\mathrm{K_2[Mn^{II}H_3\mathbf{3}^{Ph}(OH)]}$, except $\mathrm{Fe^{II}(OAc)_2}$ and $\mathrm{H_6\mathbf{3}^{F}}$ were used. The molecular structure of $\mathrm{K_2[Fe^{II}H_3\mathbf{3}^{F}(OH)]}$ was obtained by XRD, revealing a $\mathrm{Fe^{II}}$ center with a trigonal bipyramidal coordination geometry (Figure A.3 and Table A.3).

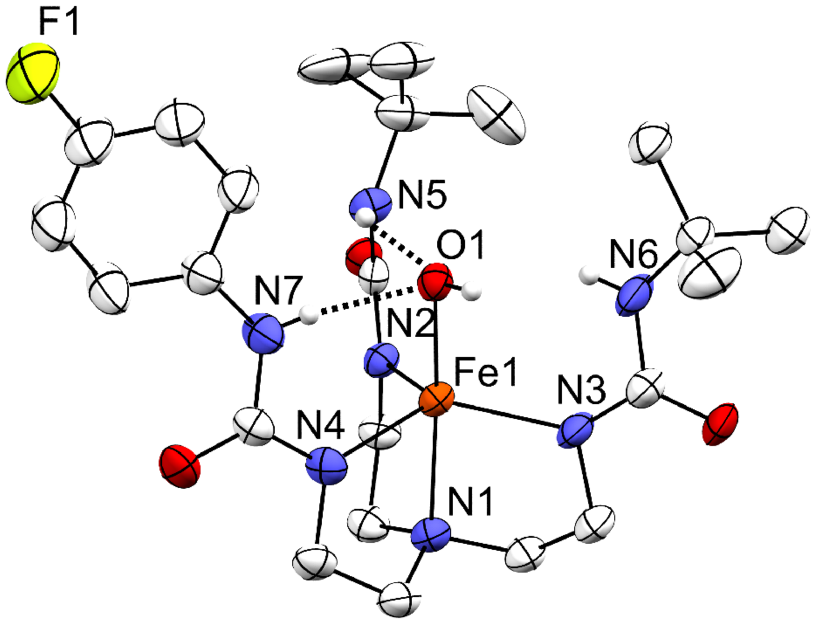

Figure A.3. Thermal ellipsoid plot of $[\mathrm{Fe^{II}H_3}\mathbf{3}^{\mathrm{F}}(\mathrm{OH})]^{2-}$. Thermal ellipsoids are drawn at the 50% probability level. Hydrogen atoms bonded to carbon were removed for clarity.

Table A.3. Selected Bond Distances (Å) and Angles (°) for $[\mathrm{Fe^{II}H_3}\mathbf{3}^{\mathrm{F}}(\mathrm{OH})]^{2-}$

Fe1–O1	2.057(3)
Fe1–N1	2.249(4)
Fe1–N2	2.097(3)
Fe1–N3	2.093(4)
Fe1–N4	2.139(4)
d(N5···O1)	2.924(5)
d(N7···O1)	2.703(5)
O1–Fe1–N1	173.92(13)
O1–Fe1–N2	104.50(13)
O1–Fe1–N3	101.74(14)
O1–Fe1–N4	96.58(13)
N4–Fe1–N1	77.84(14)
N4–Fe1–N2	104.64(14)
N4–Fe1–N3	129.88(15)
N2–Fe1–N1	79.45(13)
N2–Fe1–N3	114.93(15)
N1–Fe1–N3	80.40(14)

Synthesis of $K_2[\mathrm{Co^{II}H_3}\mathbf{3}^{Ph}(\mathrm{OH})]$. The synthesis was conducted using the same methodology as the synthesis of $\mathrm{K_2[Mn^{II}H_3}\mathbf{3}^{\mathrm{Ph}}(\mathrm{OH})]$, except $\mathrm{Co^{II}(OAc)_2}$ was used. The molecular structure of $\mathrm{K_2[Co^{II}H_3}\mathbf{3}^{\mathrm{F}}(\mathrm{OH})]$ was obtained by XRD, revealing a $\mathrm{Co^{II}}$ center with a trigonal bipyramidal coordination geometry (Figure A.4 and Table A.4).

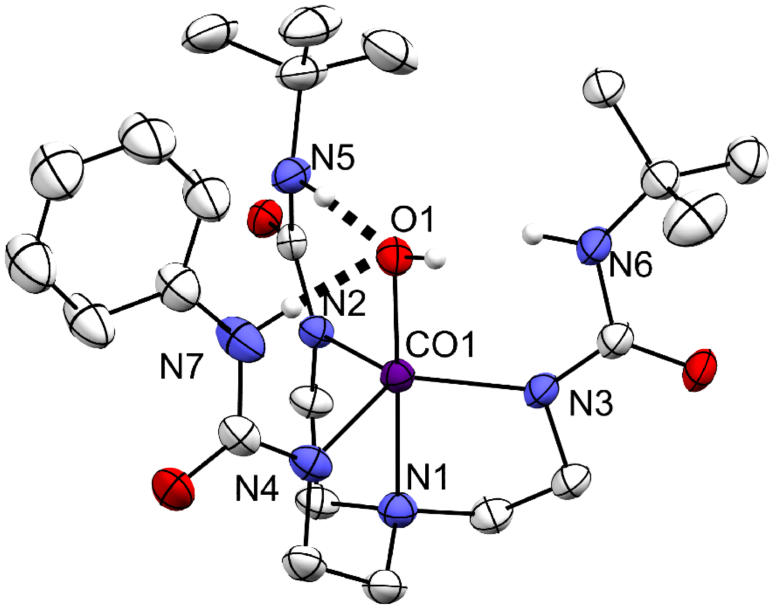

Figure A.4. Thermal ellipsoid plot of $[Co^{II}H_3\mathbf{3}^{Ph}(OH)]^{2-}$. Thermal ellipsoids are drawn at the 50% probability level. Hydrogen atoms bonded to carbon were removed for clarity.

Table A.4. Selected Bond Distances (Å) and Angles (°) for $[Co^{II}H_3\mathbf{3}^{Ph}(OH)]^{2-}$

Co1–O1	2.064(2)
Co1–N1	2.207(2)
Co1–N2	2.046(2)
Co1–N3	2.044(2)
Co1–N4	2.097(2)
d(N5⋯O1)	2.819(3)
d(N7⋯O1)	2.675(3)
O1–Co1–N1	175.55(8)
O1–Co1–N2	101.66(8)
O1–Co1–N3	100.97(8)
O1–Co1–N4	96.99(8)
N4–Co1–N1	78.86(8)
N4–Co1–N2	107.31(8)
N4–Co1–N3	126.60(9)
N2–Co1–N1	81.25(8)
N2–Co1–N3	117.34(9)
N1–Co1–N3	80.45(8)

Synthesis of $K_2[Co^{II}H_3\mathbf{3}^{F}(OH)]$. The synthesis was conducted using the same methodology as the synthesis of $K_2[Mn^{II}H_3\mathbf{3}^{Ph}(OH)]$, except $Co^{II}(OAc)_2$ and $H_6\mathbf{3}^{F}$ was used. The molecular structure of $K_2[Co^{II}H_3\mathbf{3}^{F}(OH)]$ was obtained by XRD, revealing a Co^{II} center with a trigonal bipyramidal coordination geometry (Figure A.5 and Table A.5).

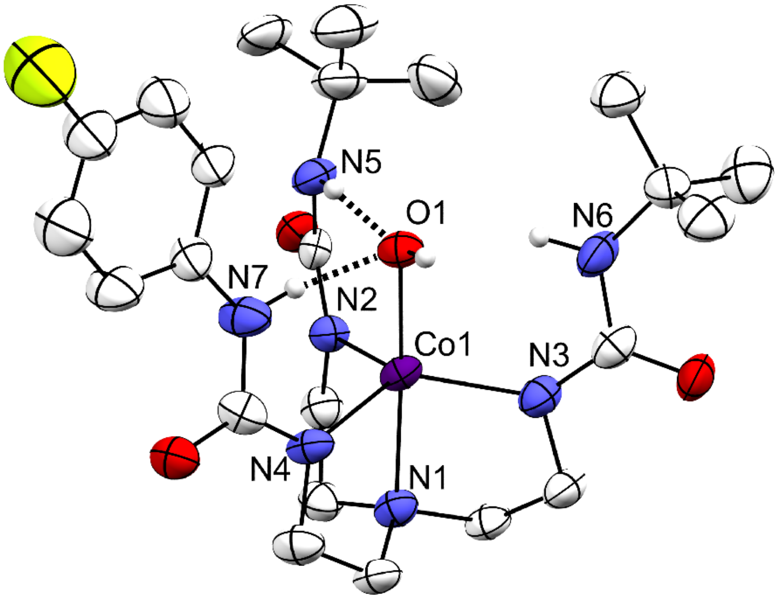

Figure A.5. Thermal ellipsoid plot of $[Co^{II}H_3\mathbf{3}^{F}(OH)]^{2-}$. Thermal ellipsoids are drawn at the 50% probability level. Hydrogen atoms bonded to carbon were removed for clarity.

Table A.5. Selected Bond Distances (Å) and Angles (°) for $[Co^{II}H_3\mathbf{3}^{F}(OH)]^{2-}$

Co1–O1	2.065(3)
Co1–N1	2.202(4)
Co1–N2	2.049(4)
Co1–N3	2.044(5)
Co1–N4	2.092(4)
d(N5···O1)	2.815(6)
d(N7···O1)	2.699(6)
O1–Co1–N1	176.34(15)
O1–Co1–N2	100.15(15)
O1–Co1–N3	101.58(16)
O1–Co1–N4	97.59(15)
N4–Co1–N1	78.76(15)
N4–Co1–N2	107.81(18)
N4–Co1–N3	126.54(18)
N2–Co1–N1	81.35(16)
N2–Co1–N3	116.97(17)
N1–Co1–N3	80.57(16)

Properties of M^{II}–OH Complexes

Electrochemical Properties of Mn^{II}–OH Complexes. The electrochemical properties of $[Mn^{II}H_3\mathbf{3}^{Ph}(OH)]^{2-}$ and $[Mn^{II}H_3\mathbf{3}^{F}(OH)]^{2-}$ were studied using cyclic voltammetry (CV) in DMSO. The $Mn^{III/II}$–OH redox potentials for $[Mn^{II}H_3\mathbf{3}^{Ph}(OH)]^{2-}$ and $[Mn^{II}H_3\mathbf{3}^{F}(OH)]^{2-}$ were observed at – 1.39 and – 1.41 V vs $[FeCp_2]^{+/0}$, respectively (Figure A.6 and Table A.6). These redox potentials are shifted by ~ 0.1 V positive of $[Mn^{II}H_3buea(OH)]^{2-}$.[1] This shift in redox potentials is smaller than the ~ 0.2 V positive shift of $[Mn^{III}H_3\mathbf{3}^{Ph}(O)]^{2-}$ compared to $[Mn^{III}H_3buea(O)]^{2-}$ shown in the chapter 3. This larger shift observed for the series of Mn^{III}–O complexes likely arises from a stronger H-bond forming from the Mn^{III}–O unit compared to a Mn^{II}–OH unit. This is supported by the structural data, which shows a shorter N7···O1 distance in $[Mn^{III}H_3\mathbf{3}^{Ph}(O)]^{2-}$ than in $[Mn^{II}H_3\mathbf{3}^{Ph}(OH)]^{2-}$.

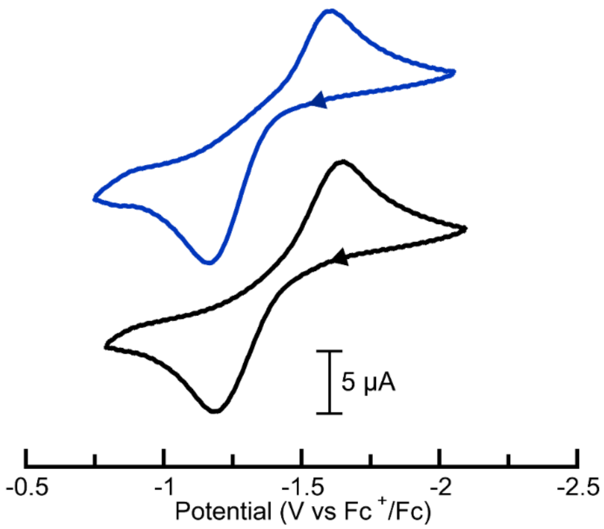

Figure A.6. CV of $[Mn^{II}H_3\mathbf{3}^{Ph}(OH)]^{2-}$ (black) and $[Mn^{II}H_3\mathbf{3}^{F}(OH)]^{2-}$ (blue) recorded in DMSO at 10 mV s^{-1}.

Electrochemical Properties of Fe^{II}–OH Complexes. The electrochemical properties of $[Fe^{II}H_3\mathbf{3}^{Ph}(OH)]^{2-}$ and $[Fe^{II}H_3\mathbf{3}^{F}(OH)]^{2-}$ were studied using cyclic voltammetry (CV) in DMSO. The $Fe^{III/II}$–OH redox potentials for $[Fe^{II}H_3\mathbf{3}^{Ph}(OH)]^{2-}$ and $[Fe^{II}H_3\mathbf{3}^{F}(OH)]^{2-}$ were observed at − 1.68 and − 1.72 V vs $[FeCp_2]^{+/0}$, respectively (Figure A.7 and Table A.6). These redox potentials are also shifted by ~ 0.1 V positive of $[Fe^{II}H_3buea(OH)]^{2-}$, similar to what was shown above for Mn^{II}.[1]

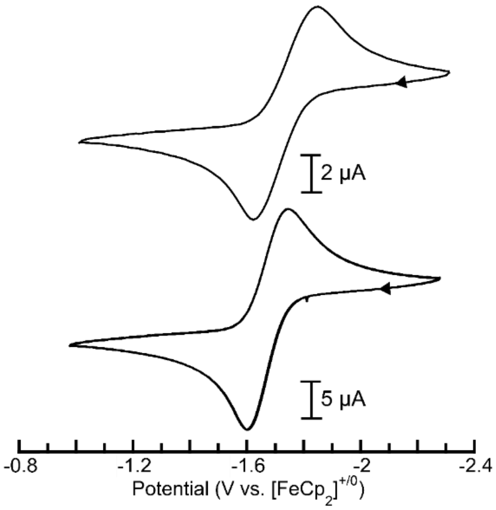

Figure A.7. CV of $[Fe^{II}H_3\mathbf{3}^{Ph}(OH)]^{2-}$ (bottom) and $[Fe^{II}H_3\mathbf{3}^{F}(OH)]^{2-}$ (top) recorded in DMSO at 10 mV s^{-1}.

Table A.6. Electrochemical Properties of Mn^{II}–OH Complexes in DMSO

	$E_{1/2}$ (V vs Fc^+/Fc)
$[Mn^{II}H_3buea(OH)]^{2-}$	– 1.51
$[Mn^{II}H_3\mathbf{3}^{Ph}(OH)]^{2-}$	– 1.39
$[Mn^{II}H_3\mathbf{3}^{F}(OH)]^{2-}$	– 1.41
$[Fe^{II}H_3buea(OH)]^{2-}$	– 1.79
$[Fe^{II}H_3\mathbf{3}^{Ph}(OH)]^{2-}$	– 1.68
$[Fe^{II}H_3\mathbf{3}^{F}(OH)]^{2-}$	– 1.72

Experimental Section

General Procedures. Unless otherwise stated, all manipulations were performed under an argon atmosphere in a Vac-atmospheres dry box. All chemicals were purchased from commercial sources and used without further purification unless otherwise stated. *N,N*-Dimethylacetamide (DMA) was purchased from Sigma-Aldrich in 99.8% purity and stirred over BaO for two days, refluxed for 1 h, followed by vacuum distillation. The ligand precursors 1-(2–(bis(2–(3–(*tert*-butyl)ureido)ethyl)amino)ethyl)-3–phenylurea ($H_6\mathbf{3}^{Ph}$) *and* 1-(2–(bis(2–(3–(*tert*-butyl)ureido)ethyl)amino)ethyl)-3–(4-fluorophenyl)urea ($H_6\mathbf{3}^{F}$) syntheses were described in chapter 3. Potassium hydride (KH) as a 30% dispersion in mineral oil was filtered with a glass frit and washed with pentane and Et_2O, dried by vacuum, and stored under an argon atmosphere.

Physical Methods. Cyclic voltammetric experiments were conducted using a CHI600C electrochemical analyzer. A 2.0 mm glassy carbon electrode was used as the working electrode at scan velocities of 10 mV s^{-1}. A ferrocenium/ferrocene couple ($[FeCp_2]^+/FeCp_2$) was used to monitor the Ag wire reference electrode, and all potentials are referenced to $[FeCp_2]^{+/0}$.

X-Ray Crystallographic Methods. A Bruker SMART APEX II diffractometer was used for molecular structure determination. The APEX2[2] program package was used to determine the unit-cell parameters and for data collection. The raw data was processed using SAINT[3] and SADABS[4] to yield the reflection data file. Subsequent calculations were carried out using the SHELXTL[5] program. The structure was solved by dual space methods and refined on F^2 by full-matrix least-squares techniques. The analytical scattering factors[6] for neutral atoms were used throughout the analysis.

$[Mn^{II}H_3\boldsymbol{3}^{Ph}(OH)]^{2-}$: Hydrogen atoms on O1, N5, N6, and N7 were located from a difference-Fourier map and refined (x,y,z and U_{iso}) and the remaining hydrogen atoms were included using a riding model. At convergence, wR2 = 0.1438 and Goof = 1.050 for 512 variables refined against 9280 data (0.74 Å), R1 = 0.0491 for those 7599 data with $I > 2.0\sigma(I)$ (Table A.7).

$[Fe^{II}H_3\boldsymbol{3}^{Ph}(OH)]^{2-}$: Hydrogen atoms on O1, N5, N6, and N7 were located from a difference-Fourier map and refined (x,y,z and U_{iso}) and the remaining hydrogen atoms were included using a riding model. At convergence, wR2 = 0.1799 and Goof = 1.035 for 512 variables refined against 10055 data (0.74 Å), R1 = 0.0621 for those 7372 data with $I > 2.0\sigma(I)$ (Table A.7).

$[Fe^{II}H_3\boldsymbol{3}^{F}(OH)]^{2-}$: Hydrogen atoms on O1, N5, N6, and N7 were located from a difference-Fourier map and refined (x,y,z and U_{iso}) and the remaining hydrogen atoms were included using a riding model. At convergence, wR2 = 0.2035 and Goof = 1.026 for 477 variables refined against 10362 data (0.73 Å), R1 = 0.0690 for those 6521 data with $I > 2.0\sigma(I)$ (Table A.8). There were several high residuals present in the final difference-Fourier map. It was not possible to determine the nature of the residuals although it was probable that diethyl ether solvent was present. The SQUEEZE[7] routine in the PLATON[8] program package was used to account for the electrons in the solvent accessible voids.

$[Co^{II}H_3\mathbf{3}^{Ph}(OH)]^{2-}$: Hydrogen atoms on O1, N5, N6, and N7 were located from a difference-Fourier map and refined (x,y,z and U_{iso}) and the remaining hydrogen atoms were included using a riding model. There were two molecules of dimethylacetamide present and one diethyl ether. At convergence, wR2 = 0.1509 and Goof = 1.035 for 512 variables refined against 10211 data (0.74 Å), R1 = 0.0534 for those 8658 data with $I > 2.0\sigma(I)$ (Table A.8).

$[Co^{II}H_3\mathbf{3}^{F}(OH)]^{2-}$: Hydrogen atoms on O1, N5, N6, and N7 were located from a difference-Fourier map and refined (x,y,z and U_{iso}) and the remaining Hydrogen atoms were included using a riding model. At convergence, wR2 = 0.2295 and Goof = 1.027 for 450 variables refined against 7983 data (0.79 Å), R1 = 0.0741 for those 4692 data with $I > 2.0\sigma(I)$ (Table A.9). There were several high residuals present in the final difference-Fourier map. It was not possible to determine the nature of the residuals although it was probable that diethyl ether solvent was present. The SQUEEZE[7] routine in the PLATON[8] program package was used to account for the electrons in the solvent accessible voids.

Table A.7. Crystallographic Data for $(K_2[Mn^{II}H_3\mathbf{3}^{Ph}(OH)])_2{\bullet}4DMA{\bullet}Et_2O$ and $(K_2[Fe^{II}H_3\mathbf{3}^{Ph}(OH)])_2{\bullet}4DMA{\bullet}Et_2O$

	$(K_2[Mn^{II}H_3\mathbf{3}^{Ph}(OH)])_2{\bullet}4DMA{\bullet}Et_2O$	$(K_2[Fe^{II}H_3\mathbf{3}^{Ph}(OH)])_2{\bullet}4DMA{\bullet}Et_2O$
Empirical Formula	$C_{66}H_{124}K_4Mn_2N_{18}O_{13}$	$C_{66}H_{124}Fe_2K_4N_{18}O_{13}$
Fw	1644.10	1645.92
T (K)	133(2)	88(2)
space group	$P\bar{1}$	$P\bar{1}$
a (Å)	11.8229(8)	11.7514(18)
b (Å)	14.0775(9)	14.091(2)
c (Å)	14.2797(10)	14.370(2)
α (deg)	70.4628(8)	69.8396(18)
β (deg)	86.5278(9)	86.4696(19)
γ (deg)	71.1569(8)	71.6838(18)
Z	1	1
V (Å^3)	2116.8(2)	2117.8(6)
δ_{calcd} (Mg/m^3)	1.290	1.291
R1	0.0491	0.0621
wR2	0.1438	0.1799
GOF	1.050	1.035

Table A.8. Crystallographic Data for $K_2[Fe^{II}H_3\mathbf{3}^F(OH)]$•2DMA and $(K_2[Co^{II}H_3\mathbf{3}^{Ph}(OH)])_2$•4DMA•$Et_2O$

	$K_2[Fe^{II}H_3\mathbf{3}^F(OH)]$•2DMA	$(K_2[Co^{II}H_3\mathbf{3}^{Ph}(OH)])_2$•4DMA•$Et_2O$
Empirical Formula	$C_{31}H_{56}FFeK_2N_9O_6$	$C_{66}H_{124}Co_2K_4N_{18}O_{13}$
Fw	803.89	1652.08
T (K)	88(2)	88(2)
space group	$P\bar{1}$	$P\bar{1}$
a (Å)	11.766(3)	11.7258(9)
b (Å)	14.048(4)	14.0845(11)
c (Å)	14.474(4)	14.3622(12)
α (deg)	69.896(3)	69.7980(10)
β (deg)	86.818(4)	86.2510(10)
γ (deg)	71.581(3)	71.0230(10)
Z	2	1
V (Å^3)	2127.8(10)	2102.1(3)
δ_{calcd} (Mg/m^3)	1.255	1.305
R1	0.0690	0.0534
wR2	0.2035	0.1509
GOF	1.026	1.035

Table A.9. Crystallographic Data for $K_2[Co^{II}H_3\mathbf{3}^F(OH)]$•2DMA

	$K_2[Co^{II}H_3\mathbf{3}^F(OH)]$•2DMA
Empirical Formula	$C_{66}H_{124}Co_2K_4N_{18}O_{13}$
Fw	1652.08
T (K)	88(2)
space group	$P\bar{1}$
a (Å)	11.7258(9)
b (Å)	14.0845(11)
c (Å)	14.3622(12)
α (deg)	69.7980(10)
β (deg)	86.2510(10)
γ (deg)	71.0230(10)
Z	1
V (Å^3)	2102.1(3)
δ_{calcd} (Mg/m^3)	1.305
R1	0.0534
wR2	0.1509
GOF	1.035

Preparative Methods.

$K_2[Mn^{II}H_3$3$^{Ph}(OH)]$: Solid KH (0.0515 g, 1.28 mmol) was treated with a 4 mL DMA solution of H_6**3**^{Ph} (0.146 g, 0.315 mmol) and stirred for 45 min until bubbling ceased. $Mn^{II}(OAc)_2$ (0.0550 g, 0.318 mmol) was then added as one portion and the resultant solution was stirred for 1 h to give a colorless heterogeneous mixture. The mixture was treated with H_2O (6 μL, 0.3 mmol) and stirred for 15 minutes. The colorless mixture was filtered through a medium porus-glass filter, and was layered with 15 mL of Et_2O, resulting colorless crystals after 1 day. The crystals were collected on a medium porous-glass filter and washed with 20 mL of Et_2O to give 0.091 g (47%) of the desired white solid.

$K_2[Mn^{II}H_3$3$^{F}(OH)]$: The salt was prepared using a similar procedure described above for $K_2[Mn^{II}H_3$**3**$^{Ph}(OH)]$ with KH (0.0271 g, 0.675 mmol), H_6**3**^{F} (0.0776 g, 0.161 mmol), $Mn^{II}(OAc)_2$ (0.0286 g, 0.165 mmol), and H_2O (3 μL, 0.2 mmol). The crystals were collected on a medium porous-glass filter and washed with 20 mL Et_2O to give 0.051 g (51%) of the desired white solid.

$K_2[Fe^{II}H_3$3$^{Ph}(OH)]$: The salt was prepared using a similar procedure described above for $K_2[Mn^{II}H_3$**3**$^{Ph}(OH)]$ with KH (0.0425 g, 1.06 mmol), H_6**3**^{Ph} (0.1190 g, 0.2567 mmol), $Fe^{II}(OAc)_2$ (0.0457 g, 0.263 mmol), and H_2O (5 μL, 0.3 mmol). The crystals were collected on a medium porous-glass filter and washed with 20 mL Et_2O to give 0.082 g (52%) of the desired white solid.

$K_2[Fe^{II}H_3$3$^{F}(OH)]$: The salt was prepared using a similar procedure described above for $K_2[Mn^{II}H_3$**3**$^{Ph}(OH)]$ with KH (0.0431 g, 1.07 mmol), H_6**3**^{F} (0.1234 g, 0.2562 mmol),

$Fe^{II}(OAc)_2$ (0.0456 g, 0.262 mmol), and H_2O (5 µL, 0.3 mmol). The crystals were collected on a medium porous-glass filter and washed with 20 mL Et_2O to give 0.077 g (48%) of the desired white solid.

$K_2[Co^{II}H_3\mathbf{3}^{Ph}(OH)]$: The salt was prepared using a similar procedure described above for $K_2[Mn^{II}H_3\mathbf{3}^{Ph}(OH)]$ with KH (0.0303 g, 0.755 mmol), $H_6\mathbf{3}^{Ph}$ (0.0874 g, 0.189 mmol), $Co^{II}(OAc)_2$ (0.0330 g, 0.186 mmol), and H_2O (5 µL, 0.3 mmol). The crystals were collected on a medium porous-glass filter and washed with 20 mL Et_2O to give 0.090 g (78%) of the desired pink solid.

$K_2[Co^{II}H_3\mathbf{3}^{F}(OH)]$: The salt was prepared using a similar procedure described above for $K_2[Mn^{II}H_3\mathbf{3}^{Ph}(OH)]$ with KH (0.0520 g, 1.30 mmol), $H_6\mathbf{3}^{F}$ (0.1561 g, 0.3241 mmol), $Co^{II}(OAc)_2$ (0.0572 g, 0.323 mmol), and H_2O (6 µL, 0.3 mmol). The crystals were collected on a medium porous-glass filter and washed with 20 mL Et_2O to give 0.085 g (50%) of the desired pink solid.

References

(1) Gupta, R.; MacBeth, C. E.; Young, V. G.; Borovik, A. S. Isolation of Monomeric Mn(III/II)−OH and Mn(III)−O Complexes from Water: Evaluation of O−H Bond Dissociation Energies. *J. Am. Chem. Soc.* **2002**, *124* (7), 1136–1137.

(2) Bruker AXS, I. APEX2 Version 2014.11-0. Madison, WI 2014.

(3) Bruker AXS, I. SAINT Version 8.34a. Madison, WI 2013.

(4) Sheldrick, G. M. SADABS. Bruker AXS, Inc: Madison 2014.

(5) Sheldrick, G. M. SHELXTL. Bruker AXS, Inc: Madison 2014.

(6) Wilson, A. J. C.; Geist, V. International Tables for Crystallography. Volume C: Mathematical, Physical and Chemical Tables. Kluwer Academic Publishers, Dordrecht/Boston/London 1992 (Published for the International Union of Crystallography), 883 Seiten, ISBN 0-792-3-16-38X. *Cryst. Res. Technol.* **1993**, *28* (1), 110–110.

(7) Spek, A. L. PLATON SQUEEZE: A Tool for the Calculation of the Disordered Solvent Contribution to the Calculated Structure Factors. *Acta Crystallogr. Sect. C Struct. Chem.* **2015**, *71* (1), 9–18.

(8) Spek, A. L. Structure Validation in Chemical Crystallography. *Acta Crystallogr. Sect. D Biol. Crystallogr.* **2009**, *65* (2), 148–155.

APPENDIX B

Mn Complexes with Sulfonamido Tripods

Synthesis of Metal Complexes

Synthesis of $Mn^{II}–OH_2$ Complexes. A solution of the ligand precursors N,N',N''-(nitrilotris(ethane-2,1-diyl))tris(4-methylbenzenesulfonamide) (H_3TST) and N,N',N''-(nitrilotris(ethane-2,1-diyl))tris(2,4,6-trimethylbenzenesulfonamide) (H_3MST) were treated with three equivalents (equiv) of KH in anhydrous dimethylacetamide (DMA). Once H_2 evolution had ceased, $Mn^{II}(OAc)_2$ and NMe_4OAc was added and the solution was filtered to remove KOAc. To the DMA solution of the salt, diethyl ether (Et_2O) was added to precipitate $(NMe_4)[Mn^{II}TST]$ or $(NMe_4)[Mn^{II}MST]$, which was treated with five equiv of H_2O in methylene chloride (CH_2Cl_2) and purified by layering the solution of the salt with pentane to give $(NMe_4)[Mn^{II}TST(OH_2)]$ or $(NMe_4)[Mn^{II}MST(OH_2)]$.

Synthesis of $Mn^{III}–OH$ Complexes. An acetonitrile (MeCN) solution of $(NMe_4)[Mn^{II}TST(OH_2)]$ or $(NMe_4)[Mn^{II}MST(OH_2)]$ was treated with one equiv of the base triazabicylclodecene (TBD) and $FeCp_2BF_4$ to give an immediate green-blue color. $FeCp_2$ was extracted from the MeCN solution using pentane to give a green solution of the salt. Single crystals of the salt were obtained by diffusion of Et_2O and pentane into the MeCN solution. The molecular structure of $(TBD\text{-}H)[Mn^{III}TST(OH)]$ was obtained by X-ray diffraction (XRD), revealing a Mn^{III} center with a trigonal bipyramidal coordination geometry.

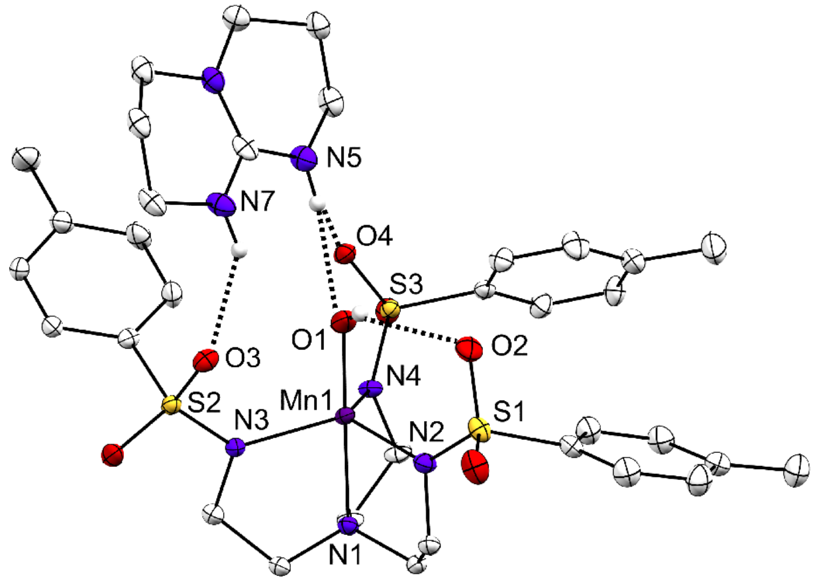

Figure B.1. Thermal ellipsoid plot of (TBD-H)[Mn$^{\text{III}}$TST(OH)]. Thermal ellipsoids are drawn at the 50% probability level. Hydrogen atoms bonded to carbon were removed for clarity.

Table B.1. Selected Bond Distances (Å) and Angles (°) for (TBD-H)[Mn$^{\text{III}}$TST(OH)]

Mn1–O1	1.849(2)
Mn1–N1	2.146(2)
Mn1–N2	2.063(2)
Mn1–N3	2.068(2)
Mn1–N4	2.078(2)
d(O1···O2)	2.785(2)
d(N5···O1)	3.040(3)
d(N5···O4)	2.924(2)
d(N7···O3)	2.819(2)
O1–Mn1–N1	178.91(7)
O1–Mn1–N2	98.15(7)
O1–Mn1–N3	100.05(7)
O1–Mn1–N4	100.20(8)
N4–Mn1–N1	80.36(6)
N4–Mn1–N2	120.12(7)
N4–Mn1–N3	114.72(7)
N2–Mn1–N1	80.77(6)
N2–Mn1–N3	117.23(7)
N1–Mn1–N3	80.52(6)

Synthesis of Mn$^{\text{III}}$–(μ–OH)–Sc^{3+}–(μ–OH)–Mn$^{\text{III}}$. A CH_2Cl_2 solution of (TBD-H)[Mn$^{\text{III}}$TST(OH)] or (TBD-H)[Mn$^{\text{III}}$MST(OH)] was treated with $Sc(OTf)_3$ and 12-crown-4 to give an green-blue solution. Single crystals for structure determination by XRD were obtained by layering the green-blue solution with pentanes (Figure B.2 and Table B.2).

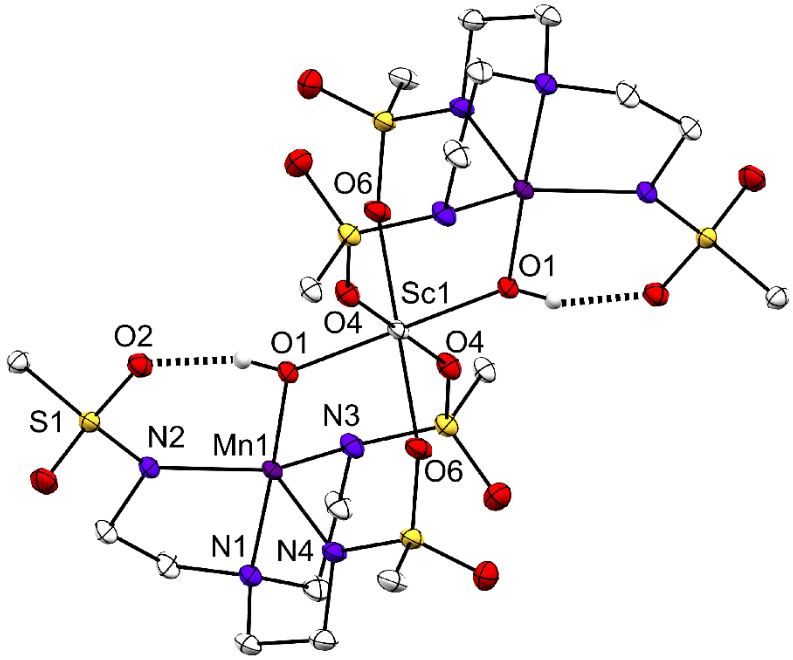

Figure B.2. Thermal ellipsoid plot of ([Mn^{III}MST(OH)]$_2$Sc^{3+})$^+$ Thermal ellipsoids are drawn at the 50% probability level. 1,3,5-trimethylbenzene and hydrogen atoms bonded to carbon were removed for clarity.

Table B.2. Selected Bond Distances (Å) and Angles (°) for ([Mn^{III}MST(OH)]$_2$Sc^{3+})$^+$

Mn1–O1	1.869(2)
Mn1–N1	2.027(2)
Mn1–N2	2.001(2)
Mn1–N3	2.051(2)
Mn1–N4	2.102(2)
Sc1–O1	2.042(2)
Sc1–O4	2.101(2)
Sc1–O6	2.094(2)
d(O1···O2)	2.591(2)
O1–Mn1–N1	177.56(5)
O1–Mn1–N2	95.32(5)
O1–Mn1–N3	97.91(5)
O1–Mn1–N4	99.31(5)
N4–Mn1–N1	81.78(5)
N4–Mn1–N2	117.46(5)
N4–Mn1–N3	106.26(6)
N2–Mn1–N1	82.25(5)
N2–Mn1–N3	131.30(6)
N1–Mn1–N3	83.84(5)
O1–Sc1–O6	87.61(4)
O1–Sc1–O4	86.56(4)
O4–Sc1–O6	89.93(5)
Sc1–O1–Mn1	125.64(6)

Experimental Section

General Procedures. Unless otherwise stated, all manipulations were performed under an argon atmosphere in a Vac-atmospheres dry box. All chemicals were purchased from commercial sources and used without further purification unless otherwise stated. N,N',N''-(nitrilotris(ethane-2,1-diyl))tris(4-methylbenzenesulfonamide) (H_3TST) and N,N',N''-(nitrilotris(ethane-2,1-diyl))tris(2,4,6-trimethylbenzenesulfonamide) (H_3MST) were prepared using literature procedures.[1,2] Potassium hydride (KH) as a 30% dispersion in mineral oil was filtered with a glass frit, washed with pentane and Et_2O, dried by vacuum and stored under an argon atmosphere.

X-Ray Crystallographic Methods. A Bruker SMART APEX II diffractometer was used for molecular structure determination. The APEX2[3] program package was used to determine the unit-cell parameters and for data collection. The raw data was processed using SAINT[4] and SADABS[5] to yield the reflection data file. Subsequent calculations were carried out using the SHELXTL[6] program. The structure was solved by dual space methods and refined on F^2 by full-matrix least-squares techniques. The analytical scattering factors[7] for neutral atoms were used throughout the analysis.

(TBD-H)[Mn^{III}TST(OH)]: Hydrogen atoms were included using a riding model. At convergence, wR2 = 0.0917 and Goof = 1.021 for 7255 variables refined against 8777 data (0.74 Å), R1 = 0.0385 for those 7255 data with $I > 2.0\sigma(I)$ (Table B.3).

([Mn^{III}MST(OH)]$_2$Sc^{3+})OTf: H1 was located from a difference-Fourier map and refined (x,y,z and U_{iso}) and the remaining hydrogen atoms were included using a riding model. A disordered triflate anion and dichloromethane molecule was present. At convergence, wR2 = 0.0889 and Goof = 1.034 for 632 variables refined against 11090 data (0.75 Å), R1 = 0.0333 for those 9921 data with $I > 2.0\sigma(I)$ (Table B.3).

Table B.3. Crystallographic Data for (TBD-H)[Mn^{III}TST(OH)]

	(TBD-H)[Mn^{III}TST(OH)]	([Mn^{III}MST(OH)]$_2$Sc^{3+})OTf•DCM•OTf
Empirical Formula	$C_{34}H_{48}MnN_7O_7S_3$	$C_{72}H_{102}Cl_{10}F_3Mn_2N_8O_{17}S_7Sc$
Fw	817.91	2142.37
T (K)	88(2)	88(2)
space group	$P\bar{1}$	$P\bar{1}$
a (Å)	8.9661(6)	13.1173(9)
b (Å)	14.6025(10)	14.4587(10)
c (Å)	14.6574(10)	14.6665(10)
α (deg)	76.3877(8)	105.9710(10)
β (deg)	84.8462(8)	110.0770(10)
γ (deg)	89.8670(9)	104.7210(10)
Z	2	1
V (Å^3)	1857.3(2)	2317(3)
δ_{calcd} (Mg/m^3)	1.463	1.535
R1	0.0385	0.0333
wR2	0.0917	0.0889
GOF	1.020	1.034

Preparative Methods.

(NMe$_4$)[Mn^{II}TST]: Solid KH (0.0843 g, 2.10 mmol) was treated with a 10 mL DMA solution of H$_3$TST (0.4191 g, 0.6884 mmol) and stirred for 45 min until bubbling ceased. Mn^{II}(OAc)$_2$ (0.1190 g, 0.6878 mmol) and NMe$_4$OAc (0.0919 g, 0.6900 mmol) was then added as one portion and stirred for 1 hour to give a colorless heterogeneous mixture. The mixture was filtered through a medium porus-glass filter and reduced in volume to 3 mL by vacuum. A white solid was precipitated by addition of 20 mL of Et$_2$O, collected on a medium porus-glass filter, washed with 20 mL of Et$_2$O, and dried by vacuum.

(NMe$_4$)[Mn^{II}MST]: The salt was prepared using a similar procedure described above for (NMe$_4$)[Mn^{II}MST] with KH (0.0860 g, 2.14 mmol), H$_3$MST (0.4912 g, 0.7098 mmol),

$Mn^{II}(OAc)_2$ (0.1231 g, 0.7116 mmol), and NMe_4OAc (0.0950 g, 0.714 mmol). A white solid was obtained (0.381 g, 66%) and dried by vacuum.

$(NMe_4)[Mn^{II}TST(OH_2)]$: A solution of $(NMe_4)[Mn^{II}TST]$ (0.1586 g, 0.2158 mmol) in 3 mL of CH_2Cl_2 was treated with 10 μL of water (0.56 mmol) and stirred for 15 minutes. The colorless solution was filtered through diatomaceous earth and a white solid (0.109 g, 67%) was precipitated with pentanes.

$(NMe_4)[Mn^{II}MST(OH_2)]$: The salt was prepared using a similar procedure described above for $(NMe_4)[Mn^{II}MST(OH_2)]$ with $(NMe_4)[Mn^{II}MST]$ (0.2228 g, 0.2720 mmol) and H_2O (5 μL, 0.3 mmol). A white solid was obtained (0.180 g, 79%) and dried by vacuum.

(TBD-H)$[Mn^{III}TST(OH)]$: A solution of $(NMe_4)[Mn^{II}TST(OH_2)]$ (0.1791 g, 0.2378 mmol) and TBD (0.0334 g, 0.240 mmol) in 10 mL of MeCN was treated with $FeCp_2BF_4$ (0.0648 g, 0.238 mmol) in 3 mL of MeCN and allowed to stir for 10 minutes to give a dark blue-green color. $FeCp_2$ was extracted with 3x10 mL of pentane to give a dark blue solution. Dark green crystals (0.072 g, 37%) suitable for XRD was obtained by diffusion of a 10:1 mixture of Et_2O:pentane into a solution of the salt.

(TBD-H)$[Mn^{III}MST(OH)]$: The salt was prepared using a similar procedure described above for (TBD-H)$[Mn^{III}TST(OH)]$ with $(NMe_4)[Mn^{II}MST]$ (0.1247 g, 0.1490 mmol), TBD (0.0207 g, 0.149 mmol), and $FeCp_2BF_4$ (0.0407 g, 0.149 mmol). A green solid was obtained (0.050 g, 79%) and dried by vacuum.

([Mn^{III}TST(OH)]$_2$Sc^{3+})OTf: A solution of and 12-crown-4 (0.0067 g, 0.038 mmol) and Sc(OTf)$_3$ (0.0175 g, 0.0356 mmol) in 2 mL CH$_2$Cl$_2$ was treated with (TBD-H)[Mn^{III}MST(OH)] (0.0347 g, 0.0385 mmol) and stirred for 15 minutes to give a green solution. Dark green crystals suitable for XRD was obtained by diffusion of a 10:1 mixture of Et$_2$O:pentane into a solution of the salt.

References

(1) Chen, D.; Motekaitis, R. J.; Murase, I.; Martell, A. E. The Synthesis of Binucleating Polyaza Macrocyclic and Macrobicyclic Ligands and the Dioxygen Affinities of Their Cobalt Complexes. *Tetrahedron* **1995**, *51* (1), 77–88.
(2) Park, Y. J.; Ziller, J. W.; Borovik, A. S. The Effects of Redox-Inactive Metal Ions on the Activation of Dioxygen: Isolation and Characterization of a Heterobimetallic Complex Containing a Mn(III)–(μ-OH)–Ca(II) Core. *J. Am. Chem. Soc.* **2011**, *133* (24), 9258–9261.
(3) Bruker AXS, I. APEX2 Version 2014.11-0. Madison, WI 2014.
(4) Bruker AXS, I. SAINT Version 8.34a. Madison, WI 2013.
(5) Sheldrick, G. M. SADABS. Bruker AXS, Inc: Madison 2014.
(6) Sheldrick, G. M. SHELXTL. Bruker AXS, Inc: Madison 2014.
(7) Wilson, A. J. C.; Geist, V. International Tables for Crystallography. Volume C: Mathematical, Physical and Chemical Tables. Kluwer Academic Publishers, Dordrecht/Boston/London 1992 (Published for the International Union of Crystallography), 883 Seiten, ISBN 0-792-3-16-38X. *Cryst. Res. Technol.* **1993**, *28* (1), 110–110.